University of Arkansas, Fayetteville

ScholarWorks@UARK

Theses and Dissertations

8-2019

Growth of Indium Nitride Quantum Dots by Molecular Beam Epitaxy

Steven P. Minor
University of Arkansas, Fayetteville

Follow this and additional works at: https://scholarworks.uark.edu/etd

Part of the Electromagnetics and Photonics Commons, Optics Commons, and the Semiconductor and Optical Materials Commons

Recommended Citation

Minor, Steven P., "Growth of Indium Nitride Quantum Dots by Molecular Beam Epitaxy" (2019). *Theses and Dissertations*. 3398.
https://scholarworks.uark.edu/etd/3398

This Dissertation is brought to you for free and open access by ScholarWorks@UARK. It has been accepted for inclusion in Theses and Dissertations by an authorized administrator of ScholarWorks@UARK. For more information, please contact ccmiddle@uark.edu.

Growth of Indium Nitride Quantum Dots by Molecular Beam Epitaxy

A dissertation submitted in partial fulfillment
of the requirements for the degree of
Doctor of Philosophy in Microelectronics-Photonics

by

Steven P. Minor
Arkansas State University
Bachelor of Science in Engineering, 2008
University of Arkansas
Master of Science in Microelectronics-Photonics, 2012

December 2019
University of Arkansas

This dissertation is approved for recommendation to the Graduate Council.

Gregory J. Salamo, Ph.D.
Dissertation Director

Hameed Naseem, Ph.D. Committee Member	Shui-Qing Yu, Ph.D. Committee Member
Morgan Ware, Ph.D. Committee Member	Rick Wise, Ph.D. Ex-Officio Member

The following signatories attest that all software used in this dissertation was legally licensed for use by Steven P. Minor for research purposes and publication.

________________________________ ________________________________

Mr. Steven P. Minor, Student Dr. Gregory J. Salamo, Dissertation Director

This dissertation was submitted to http://www.turnitin.com for plagiarism review by the TurnItIn company's software. The signatories have examined the report on this dissertation that was returned by TurnItIn and attest that, in their opinion, the items highlighted by the software are incidental to common usage and are not plagiarized material.

________________________________ ________________________________

Dr. Rick Wise, Program Director Dr. Gregory J. Salamo, Dissertation Director

Abstract

Over the last decade, the evolution of the global consciousness in response to decreasing environmental conditions from global warming and pollution has led to an outcry for finding new alternative/clean methods for harvesting energy and determining ways to minimize energy consumption. III-nitride materials are of interest for optoelectronic and electronic device applications such as high efficiency solar cells, solid state lighting (LEDs), and blue laser (Blu-ray Technology) applications. The wide range of direct band gaps covered by its alloys (0.7eV-6.2eV) best illustrates the versatility of III-nitride materials. This wide range has enabled applications extending from the ultraviolet to the near infrared. This study investigates the processes by which InN quantum dots (QDs) form through molecular beam epitaxy (MBE) growth in Nitrogen-Rich and Metal-Rich growth environments.

Structural characterization was performed using Atomic Force Microscopy. Statistical analysis was performed on both growth environments, Metal-Rich and Nitrogen-Rich, to observe changes in nucleation density, QD height and diameter, volume of InN, and the contact angle between the QDs and the growth surface. To further understand the growth environments, the system was analyzed as functions of growth temperature, deposition time, and deposition rate. Under Nitrogen-Rich growth environment, it was found that the growth of InN QDs follows typical Stranski-Krastinov (SK), heterogeneous nucleation theory. However, due to the existence of an excess indium adlayer, the Metal-Rich growth condition changes the development of the InN QDs. The results of this investigation are presented herein. A cursory investigation in the optical response of both growth environments was performed. The optical response was characterized through photoluminescence (PL) spectroscopy with a transition at 730 nm for Metal-Rich InN QDs using a two-step GaN capping procedure.

Acknowledgements

Working as a fulltime faculty member with a wife and two daughters while trying to complete a dissertation, has been extremely difficult. A process that should have taken a year has now stretched into five years. However, there are many people in my life that never lost faith in me, encouraged me, and tolerated my behavior during the rough times. I would like to take this opportunity to acknowledge those people.

Firstly, I would like to thank my wife, Andrea Minor, and my daughters, Mckenzie and Teagan Minor. You have been instrumental in giving me the support and love that I so desperately needed. I have moved you across the state twice during this process, and you have followed me without question.

Dr. Greg Salamo, my research advisor and mentor, thank you for everything that you have done. Your relentless pursuit of knowledge, scientific curiosity, and work ethic have served as shining examples to myself and my fellow graduate students.

I would like to thank Dr. Morgan Ware. We have shared many conversations on the topic of thin film growth. I would also like to thank the rest of my committee, Dr. Hameed Naseem and Dr. Fisher Yu.

To the MicroEP program staff, and especially Renee Hearon, thank you for your support. Renee, I do not know how you can be such a good surrogate mother to so many graduate students.

I would like to thank my fellow graduate students who have helped me along the way, including, but not limited to: Colin Furrow, Rob Sleezer, Chen Li, Thomas White, Sabina

Koukourinkova, Tim Morgan, and Mohammad Zamani.

I would also like to thank my hosts that gave me a place to stay during my summer trips back to the University of Arkansas in order to complete my dissertation. Raymond and Solomon Jones have treated me like family since I met them. I could not have done this without their support.

Finally, I would like to thank my mother, Jackie Holloway. My mother has “fought against the current” her entire life. She was the first in our family to earn a college degree and the first in our family to earn a graduate degree. Setting the example of how an education can further one’s career, in my opinion, has changed the course of my life, the lives of my children, and future generations to come. Mom, thank you for blazing the trail for our family.

Dedication

I dedicate this dissertation to my family and friends. Thank you.

Table of Contents

Chapter 1: Introduction to the Study 1

1.1 Introduction 1

1.2 Benefits and Limitations of Nitride Materials for Photonic Applications 2

1.2.1 III-Nitride Material Properties 3

1.3 Current Understanding of Nitride Growth 7

1.3.1 Two Dimensional Structures, InN Epitaxial Layers by MBE 8
1.3.2 Zero Dimensional Structures, InN Quantum Dots by MBE 9

1.4 Scope of Study 9

Chapter 2: Nitride Materials by Molecular Beam Epitaxy 11

2.1 Confinement Theory 11

2.2 Nucleation Theory 13

2.2.1 Heterogeneous Nucleation 14

2.3 Molecular Beam Epitaxy 19

2.3.1 MBE System Components 19
2.3.2 In-situ RHEED Analysis 21
2.3.3 MBE Growth Calibrations 23

Chapter 3: Characterization Methods and Statistical Analysis 26

3.1 Atomic Force Microscopy 26

3.2 Photoluminescence 27

3.3 InN QD Analysis Techniques 28

3.4 Confidence Intervals and Student’s t Distribution 31

Chapter 4: Results and Discussion 35

4.1 Nitrogen-Rich Growth 36

4.1.1 Growth Temperature Dependence 36
4.1.2 Deposition Time Dependence 44
4.1.3 Deposition Rate Dependence 50

4.2 Metal-Rich Growth 57

4.2.1 Growth Temperature Dependence 57
4.2.2 Deposition Time Dependence 63
4.2.3 Deposition Rate Dependence 69

4.3 Comparison of Nitrogen-Rich and Metal-Rich Growth Environments 74

4.4 The Presence of Excess Indium 77

4.5 Summary of Metal-Rich Deviations 80

4.6 Light Emitting Structures 80

Chapter 5: Conclusions & Future Work 83

5.1 Conclusions 83

5.2 Future Work 84

References 85

Appendix A: Description of Research for Popular Publication 90

Appendix B: Executive Summary of Newly Created Intellectual Property 92

Appendix C: Potential Patent and Commercialization Aspects of listed Intellectual Property Items 93

C.1 Patentability of Intellectual Property 93

C.2 Commercialization Prospects (Should Each Item be Patented) 93

C.3 Possible Prior Disclosure of IP 93

Appendix D: Broader Impact of Research 94

D.1 Applicability of Research Methods to Other Problems 94

D.2 Impact of Research Results on U.S. and Global Society 94

D.3 Impact of Research Results on the Environment 94

Appendix E: Microsoft Project for PhD MicroEP Degree Plan 96

Appendix F: Identification of All Software Used in Research and Dissertation Generation 97

Appendix G: All Publications Published, Submitted and Planned 98

List of Figures

Figure 1. Illustrations of Zincblene (a) and Wurtzite (b) Crystal Structures. 4

Figure 2. III-Nitride and other III-V Semiconductor Properties. 5

Figure 3. Example of Visible Spectrum with Associated Photon Energy. 7

Figure 4. Graphical Representation of a Finite Potential Well. 12

Figure 5. Example of Graphical Means for Solving Quantized Energy States Within the Conduction Band of the Exciton in InN QDs. 14

Figure 6. Illustration of Capillarity Theory..16

Figure 7. Descriptive Breakdown of the Gibbs Free Energy Equation. 16

Figure 8. Graphical Illustration of Modular MBE Configuration...20

Figure 9. RHEED Example of 3D Surface (a) and 2D Surface (b) Grown by MBE. 22

Figure 10. In-situ RHEED Analysis Using RHEED Oscillations to Monitor Growth Rate..........23

Figure 11. Calibration Result for an MBE Effusion Cell. 24

Figure 12. Result of a Stoichiometric Growth Point Calibration..25

Figure 13. Graphical Representation of the Three-Carrier Recombination Processes. 27

Figure 14. Using the Flattening Procedure in Nanoscope Analysis Software v1.50. 29

Figure 15. Using the Particle Analysis Tool in Nanoscope Analysis Software. 30

Figure 16. Example of Using Particle Remove Function in Nanoscope Analysis Software. 31

Figure 17. Example of Using the Section Tool in Nanoscope Analysis Software in order to Measure Contact Angle of InN QDs...32

Figure 18. Examples of a Normal, Gaussian Distribution and a Student's t Distribution for Comparison. 33

Figure 19. AFM scans of Nitrogen-Rich, Growth Temperature Dependent Samples. 37

Figure 20. QD Density as a Function of 1/kT for Nitrogen-Rich InN QDs. 38

Figure 21. QD Height as a Function of 1/kT for Nitrogen-Rich InN QDs. 40

Figure 22. QD Diameter as a Function of 1/kT for Nitrogen-Rich InN QDs. 40

Figure 23. Graphical Representation of the Change in Nucleation Density and Capture Area as a Function of Growth Substrate Temperature. 41

Figure 24. Volume of Deposited InN as a function of 1/kT for Nitrogen-Rich InN QDs. 42

Figure 25. QD Contact Angle as a Function Substrate Temperature for Nitrogen-Rich InN QDs. 43

Figure 26. AFM Scans of Nitrogen-Rich, Deposition Time Dependent Samples. 44

Figure 27. QD Density as a Function Deposition Time for Nitrogen-Rich InN QDs. 45

Figure 28. QD Height as a Function Deposition Time for Nitrogen-Rich InN QDs. 47

Figure 29. QD Diameter as a Function Deposition Time for Nitrogen-Rich InN QDs. 47

Figure 30. Volume of Deposited InN as a Function of Deposition Time for Nitrogen-Rich InN QDs. 48

Figure 31. QD Contact Angle as a Function of Deposition Time for Nitrogen-Rich InN QDs. ...49

Figure 32. AFM scans of Nitrogen-Rich, Deposition Rate Dependent samples. 50

Figure 33. QD Density as a Function of Deposition Rate for Nitrogen-Rich InN QDs. 51

Figure 34. QD Height as a Function of Deposition Rate for Nitrogen-Rich InN QDs..................54

Figure 35. QD Diameter as a Function of Deposition Rate for Nitrogen-Rich InN QDs..............54

Figure 36. Volume of Deposited InN as a Function of Deposition Rate for Nitrogen-Rich InN QDs. 56

Figure 37. QD Contact Angle as a Function Deposition Rate for Nitrogen-Rich InN QDs..........56

Figure 38. AFM scans of Metal-Rich, Growth Temperature Dependent samples. 57

Figure 39. QD Density as a Function of 1/kT for Metal-Rich InN QDs. 58

Figure 40. QD Height as a Function of 1/kT for Metal-Rich InN QDs. 60

Figure 41. QD Diameter as a Function of 1/kT for Metal-Rich InN QDs. 60

Figure 42. Deposited InN Volume as a Function of 1/kT for Metal-Rich InN QDs. 62

Figure 43. QD contact angle as a function Growth Temperature for Metal-Rich InN QDs..........62

Figure 44. AFM scans of Metal-Rich, Deposition Time Dependent samples. 63

Figure 45. QD Density as a Function of Deposition Time for Metal-Rich InN QDs. 64

Figure 46. QD Height as a Function of Deposition Time for Metal-Rich InN QDs. 65

Figure 47. QD Diameter as a Function of Deposition Time for Metal-Rich InN QDs. 66

Figure 48. Deposited InN Volume as a Function of Deposition Time for Metal-Rich InN QDs..67

Figure 49. QD Contact Angle as a Function Deposition Time for Metal-Rich InN QDs. 68

Figure 50. AFM scans of Metal-Rich, Deposition Rate Dependent samples. 69

Figure 51. QD Density as a Function of Deposition Rate for Metal-Rich InN QDs. 70

Figure 52. QD Height as a Function of Deposition Rate for Metal-Rich InN QDs. 72

Figure 53. QD Diameter as a Function of Deposition Rate for Metal-Rich InN QDs. 72

Figure 54. Deposited InN Volume as a Function of Deposition Rate for Metal-Rich InN QDs...73

Figure 55. QD Contact Angle as a Function Deposition Rate for Metal-Rich InN QDs. 74

Figure 56. InN Shape Comparison for Metal-Rich and Nitrogen-Rich Growth Conditions at 390°C. 76

Figure 57. InN Shape Comparison for Metal-Rich and Nitrogen-Rich Growth Conditions at 400°C. 76

Figure 58. InN Shape Comparison for Metal-Rich and Nitrogen-Rich Growth Conditions at 410°C. 77

Figure 59. AFM Scans of Samples used for Analyzing the Possibility of Excess Indium on the Growth Surface. 78

Figure 60. Nitrogen-Rich Uncapped QD AFM Scan Analysis Showing No Significant Change After 5 Years. 78

Figure 61. QD Diameter and Height distributions for Metal-Rich QD Showing Effects of Oxidation...79

Figure 62. Conceptual Illustration of the Change in Structure Height Due to the Presence of an Indium Adlayer, an Oxidized Indium Layer, or Bare Growth Surface...............................79

Figure 63. Graphical Illustration of the Metal-Rich InN QD structure. 81

Figure 64. Graphical Illustration of the Nitrogen-Rich InN QD structure. 82

Figure 65. Graphical Illustration of the GaN reference structure. 82

Figure 66. The Results of the PL Spectroscopy for Confined InN/GaN QDs Using Metal-Rich and Nitrogen-Rich Growth Conditions: a) Metal-Rich, b) Nitrogen-Rich, and c) LT/HT GaN Reference...82

List of Tables

Table 1. Calculated Bohr Radii for Select III-Nitride and III-Arsenide Materials 12

Table 2. Calculated Energy States for Indium Nitride Quantum Dots with a GaN Barrier for Heights at and below the bulk Bohr Exciton Radius. 14

Table 3. Nitrogen-Rich InN QD Density as a Function of Growth Temperature......................... 37

Table 4. Nitrogen-Rich InN QD Height as a Function of Growth Temperature 39

Table 5. Nitrogen-Rich InN QD Diameter as a Function of Growth Temperature 39

Table 6. Nitrogen-Rich InN QD Density as a Function of Deposition Time. 45

Table 7. Nitrogen-Rich InN QD Height as a Function of Deposition Time. 46

Table 8. Nitrogen-Rich InN QD Diameter as a Function of Deposition Time. 46

Table 9. Nitrogen-Rich InN QD Density as a Function of Deposition Rate. 51

Table 10. Nitrogen-Rich InN QD Height as a Function of Deposition Rate. 53

Table 11. Nitrogen-Rich InN QD Diameter as a Function of Deposition Rate. 53

Table 12. Metal-Rich InN QD Density as a Function of Growth Temperature. 58

Table 13. Metal-Rich InN QD Height as a Function of Growth Temperature. 59

Table 14. Metal-Rich InN QD Diameter as a Function of Growth Temperature. 59

Table 15. Metal-Rich InN QD Density as a Function of Deposition Time. 64

Table 16. Metal-Rich InN QD Height as a Function of Deposition Time. 65

Table 17. Metal-Rich InN QD Diameter as a Function of Deposition Time. 66

Table 18. Metal-Rich InN QD Density as a Function of Deposition Rate. 70

Table 19. Metal-Rich InN QD Height as a Function of Deposition Rate. 71

Table 20. Metal-Rich InN QD Diameter as a Function of Deposition Rate. 71

Chapter 1: Introduction to the Study

1.1 Introduction

Over the last decade, the evolution of the global consciousness in response to decreasing environmental conditions from global warming and pollution has led to an outcry for finding new alternative/clean methods for harvesting energy and determining ways to minimize energy consumption. Scientific research and industrial innovation have made significant strides in developing new materials and devices in order to achieve these outcomes. Alternative energy, non-fossil fuel sources such as solar panels and wind turbines have reduced drastically in cost and increased in efficiency over the past 20 years. While new means of producing energy without the burning of fossil fuels meets global desire, ways of reducing the use of harvested energy must be improved. One way to achieve this goal is to reduce the energy required by household and commercial lighting.

A report from the Department of Energy (DOE) shows that lighting consumed 12% of the total energy consumed in the United States in 2011 [1]. The incandescent bulb and fluorescent lamp have contributed as the main sources of lighting both commercially and residentially through recent history. The incandescent bulb is highly inefficient. An incandescent bulb produces light with a filament wire, which is heated by an electrical current. Less than 5% of this electrical power is converted to visible light; whereas, 95% of the electrical power is transformed into heat. The compact fluorescent lamp is more efficient than the incandescent bulb, using around 33% of the power in comparison to the incandescent bulb to produce the same amount of light [2]. However, there is still a more efficient way to produce light.

The LED, or light emitting diode, is a strong candidate for becoming the new “light bulb”

due to its lower power consumption. The LED, since its invention by Oleg Vladimirovich Losev, has garnered much attention in order to enhance its performance. Recent advances in this technology by LED industry leaders Phillips and Cree, which will be discussed in further detail later, have reduced the power consumption of the LED to around ~12% of the power required by the incandescent bulb [3] with the goal of reaching 10% in near future. In order to put this into perspective, one could get five times the "light" from using LEDs for the same energy consumption as one incandescent bulb. A 2010 article by LED professional estimated LEDs with 100% market penetration and 50% conversion efficiency would save the U.S. 525 terawatt-hour per year or $35 billion per year in power production costs and that the carbon dioxide equivalent emission would be reduced by approximately 87 Megatons [4].

1.2 Benefits and Limitations of Nitride Materials for Photonic Applications

III-nitride materials are of interest for optoelectronic and electronic device applications. The wide range of direct band gaps covered by its alloys (0.7eV-6.2eV) best illustrates the versatility of III-nitride materials. This wide range has enabled applications extending from the ultraviolet to the near infrared. Tremendous gains in understanding the growth dynamics of this material system have recently led to its subsequent use in both solid state lighting (LEDs) and blue laser (BluRay Technology) applications. In addition, nanostructures created from these materials open the door for exciting studies in both physics and engineering, which may lead to new classes of optoelectronic and electronic devices. The following discussion will highlight the material properties of III-Nitrides and the current limitations that are faced when using these materials.

1.2.1 III-Nitride Material Properties

The following sections are an overview of the material properties of InN and GaN. These two binary semiconductors were at the center of focus within this research. Indium gallium nitride (InGaN) was not specifically covered due to it being an alloy of the two binary semiconductors.

1.2.1.1 Crystalline Structure

III-nitride materials are found in three possible crystal structures: wurtzite, zincblende, and rock salt. Wurtzite is the most stable of the three structures. It is also the most common and is an example of the hexagonal crystal system. The zincblende structure of III-nitride materials is considered metastable and can be grown on the {011} crystal planes of silicon, magnesium oxide, and gallium arsenide. Rock salt is only produced under very high pressures [5].

The wurtzite unit cell has two lattice constants, a and c. Its space grouping is $P6_3mc$. This means that the unit cell has 6-fold symmetry around the c-axis, a mirror plane to the normal (m), and a glide plane alone the c-axis. The wurtzite structure consists of two interpenetrating hexagonal close packed (HCP) sublattices which are separated by 5/8 of the cell height [5].

The zincblende unit cell is an example of the diamond crystal system. The zincblend unit cell consists of two interpenetrating Face Centered Cubic (FCC) sublattices with a two atom basis. The FCC sublattices are separated by sqrt(3)/4 of the lattice constant, a. The zincblende structure has a space grouping of $F\bar{4}3m$ [5].

The wurtzite and zincblende unit cells are similar. In both cases, the group III atom (gallium or indium) is bonded to four nitrogen atoms, and nitrogen atoms are bonded to four

group III atoms. The main difference between the two unit cells is found in the stacking sequence of the closest packed diatomic. For wurtzite, this would be the (0001) plane, and the (111) plane in the zincblende unit cell. The stacking sequence for each unit cell are ABABAB for wurtzite in the <0001> direction, and ABCABC for zincblende in the <111> direction. Each crystalline system has a mirror plane. Where the stacking planes A and B are the mirror opposites. The C stacking plane occurs due to the 60° rotation. Examples of the wurtzite and zincblende crystal structures can be seen in Figure 1 [5].

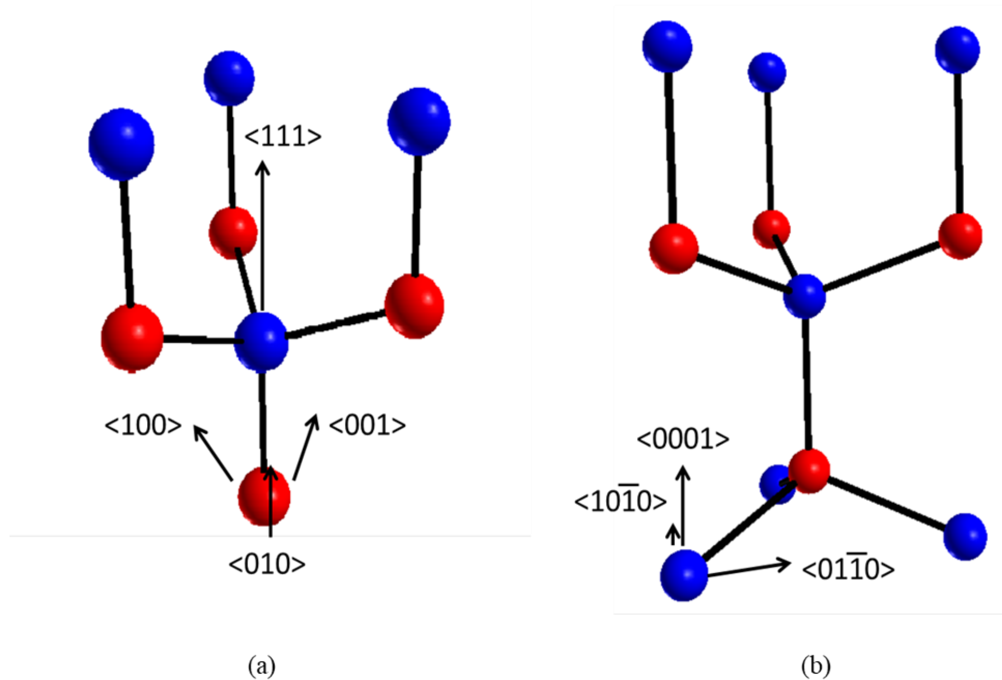

Figure 1. Illustrations of Zincblene (a) and Wurtzite (b) Crystal Structures.

It is widely known that III-nitride materials suffer from large dislocation densities (~10^9 cm^{-2}). Screw and edge dislocations are the primary types of defects found in GaN, InN, and AlN growth. A dislocation is an irregularity in the crystalline lattice and can influence the properties of the material. Many material properties that are important to device operation are affected by

these irregularities in the crystal structure. Most notably, dislocation defects can create non-radiative recombination centers within the crystal and limit a structure's luminescent efficiency.

This characteristic flaw is caused by the lack of a native substrate on which to grow nitride materials. Lattice mismatches range from 3-11% within the family of alloys (AlN, GaN, and InN) with InN having an ~11% lattice mismatch with GaN. Some groups have substituted Si (111) as a growth substrate; however, InN still has a lattice mismatch of ~8% with Si (111). C-plane lattice constants for III-nitride materials can be seen in Figure 2.

The most common growth substrate begins with sapphire (Al_2O_3). Under high temperature conditions and an active nitrogen flux, the oxygen atoms in the very top layer of sapphire can be replaced with nitrogen which creates a very thin (~2-3 MLs) AlN surface. This process is referred to as nitridation. After surface nitridation, a few hundred nanometers of AlN is deposited followed by microns of GaN. AlN and GaN only share a 3% lattice mismatch. Many of the initial dislocations created during nitridation are removed if the GaN is grown sufficiently thick (~3-5 um).

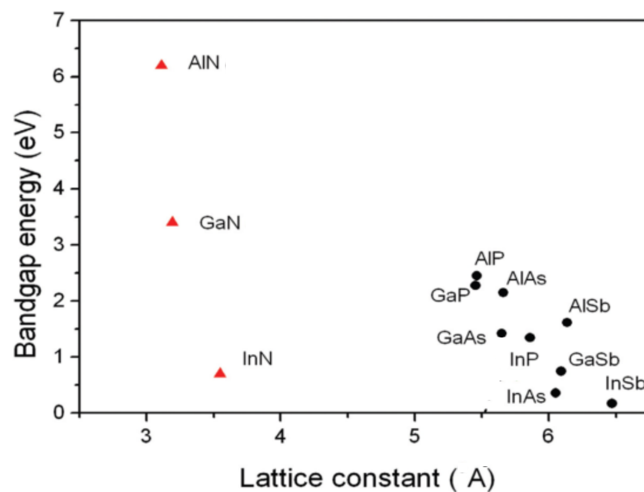

Figure 2. III-Nitride and other III-V Semiconductor Properties [6].

III-V materials such as GaAs, InAs, InP, etc. benefit from having native substrates on which to grow. Silicon and germanium substrates provide an adequate lattice match for high quality crystalline growth of these other III-V materials as seen in Figure 2. Current growth methods have produced these III-V materials, such as those mentioned previously, with dislocation densities around 1000-2000 cm^{-2} [7]. Improvements have been made on these III-V materials due to the overwhelming amount of research that has continued since the 1980s.

1.2.1.2 Optical Properties

Of the III-nitride alloys, indium nitride (InN) can be considered a “new” interest in semiconductor research. Until recently, the bandgap for this material was considered to be around 2 eV. This, however, has been proven to be wrong by many groups [8]. The actual bandgap of InN has been measured to be 0.7 eV. This incorrectly observed bandgap has been attributed to oxygen contamination due to early InN films being grown by sputter deposition. Currently, high quality InN films are being successfully grown using molecular beam epitaxy (MBE) [8]. Indium nitride’s low bandgap energy of 0.7 eV is equivalent to a wavelength of 1.77 microns. This wavelength corresponds to the near-infrared region of the EM spectrum as seen in Figure 3. Gallium nitride (GaN) is another important compound in the III-nitride family. GaN’s measured bandgap is 3.4 eV. This band gap energy is equivalent to a wavelength of around 364 nm and is in the ultraviolet portion of the solar spectrum. With the new reported bandgap energy value of indium nitride, a system of alloys or a III-nitride heterostructure utilizing quantum confinement can be created using gallium, indium, and nitrogen that can cover the entire visible spectrum.

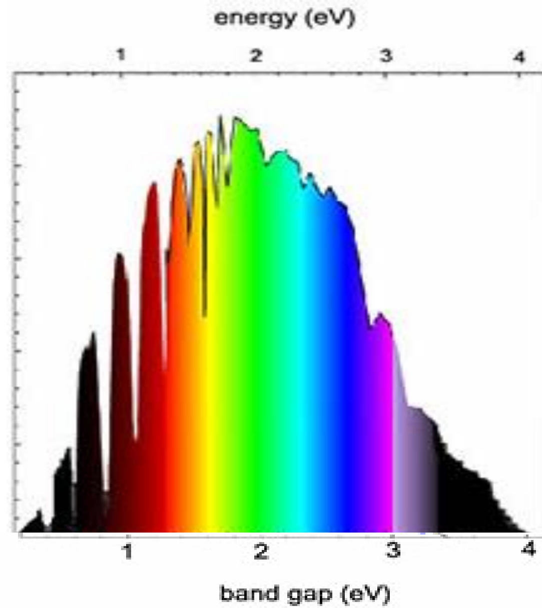

Figure 3. Example of Visible Spectrum with Associated Photon Energy [9].

1.3 Current Understanding of Nitride Growth

Interest in understanding the growth and fabrication of III-nitride materials picked up in 2000 when the bandgap of InN was determined to be 0.7 eV, and not 1.9 eV [5]. The importance of this discovery has already been discussed in the previous section. Using III-nitride material systems in the production of LEDs, high efficiency solar cells, and other optoelectronic devices was now possible. After 2000, the research community has attempted to grow InN by means of metalorganic vapor-phase epitaxy (MOVPE) [10-11], molecular beam epitaxy (MBE) [12-33], sputtering [34], hydride vapor-phase epitaxy (HVPE) [35-37], pulsed laser deposition (PLD) [38-40], and several other methods [41-44]. Throughout these methods, many substrates have been used to overcome the III-nitride's lack of a native substrate: sapphire (Al_2O_3), Si (111), GaAs, InAs, InP, GaN, and AlN.

Some important observations have been made on the growth of InN and other III-nitride

materials. For InN, dissociation begins with temperatures as low as 430 °C, and the desorption temperature of indium in UHV is ~ 630°C. These are important temperatures when considering the growth of InN. In addition, it has been observed for all III-nitride materials that films grown with a III/N flux ratio of greater than unity exhibit smooth surfaces, and films grown with a III/N flux ratio of less than unity exhibit a rough surface [45]. In addition, it was shown theoretically by Neugebauer et al. that an effective surface diffusion channel for nitrogen adatoms is created when a sufficient indium adlayer is present [46]. Neugebauer's discovery is significant. Enhanced diffusion at low temperatures can improve crystal growth in MBE at lower than optimal temperatures.

The motivation behind this research is confined InN. A confined semiconductor can be classified as one of three structures: a 2D planar film or quantum well (QW), a 1D quantum wire (QWR), or a 0D quantum dot (QD). The dimensionality of the structure refers to the freedom of the electron to move, therefore in a QD, the electron is confined in each direction, X, Y, and Z. The following two sections will discuss some of the work that has been performed on the growth of InN by MBE for 2D and 0D structures. Quantum wires will not be discussed due to their lack of use in this research.

1.3.1 Two Dimensional Structures, InN Epitaxial Layers by MBE

Due to the electrical properties of InN thin films, many research groups have investigated the growth of two dimensional, epitaxial layers of InN by MBE. The main challenges reported by many of these groups are the precise control of the III/V ratio and the growth temperature. For the purposes of this research, high quality, low growth temperature GaN was required.

Low temperature GaN capping layers for InN QDs were investigated by Lozano et al.

[47]. In this work, two samples were produced: an uncapped InN QD sample and a GaN capped InN QD sample. The GaN cap was grown with a two-step process. First, a layer was grown at 550 °C for long enough to cover the InN QDs. Second, the growth temperature was raised to 1050 °C and the growth of the capping layer continued. The group found through TEM that the dimensions of the InN QD changed after capping. Capping of GaN made the InN QDs "shorter" and "wider."

1.3.2 Zero Dimensional Structures, InN Quantum Dots by MBE

In 2002, Nörenberg et al. attempted to control the size and density of self-assembled InN nanostructures on GaN by MBE [19]. In their research, two different nitrogen delivery methods were used, thermally cracked ammonia and a modified plasma source. Using the nitrogen plasma source, the group reported Stranski-Krastanov growth at "higher" V/III flux ratios. The flux ratio was never reported, but the group did observe QD densities of 4.8×10^{11}-1.3×10^{12} cm^{-2} for growth temperatures of 350-400 °C and layer thicknesses of 4-8 MLs [19].

In 2006, InN QDs were investigated by Dimakis et al. [28]. For that study, three groups of samples were created. These groups were to investigate the role of temperature, time, and In/N flux ratio (0.15-0.30) on the density and size of the QDs. It was found that as temperature increased, the QD density decreased and the size of the QDs increased. The group noted that the growth rate of the InN QDs was affected by dissociation at 470°C.

1.4 Scope of Study

The research presented herein was performed in order to understand the underlying growth mechanics involved in the creation of InN QDs through molecular beam epitaxy. The motivation

of this study was the use of InN QDs in optoelectronic devices such as LEDs, solar cells, etc. A comprehensive look at past and present research of 2D and 3D III-nitride structures was conducted. As shown through this literature review, many articles have been published on the growth of III-nitride quantum structures; however, a comprehensive investigation into the various methods of producing InN QDs, and understanding the root causes of these different methods was needed. Special emphasis was given in this work to developing a working model to predict the density and size of InN QDs. Control of InN QD density and size allows for the tailoring of a structure's emitted radiation wavelength. Multiple characterization techniques were utilized which included: Atomic Force Microscopy (AFM), Reflective High Energy Diffraction (RHEED), and Photoluminescence (PL).

Chapter 2: Nitride Materials by Molecular Beam Epitaxy

2.1 Confinement Theory

The following section will discuss the theory of quantum confinement as it pertains to tailoring the emission wavelength of semiconductor nanostructures and, in particular, InN QDs. Special attention was given to calculating logical estimations of energy state values for various InN QD structures of different sizes. These estimations are given herein.

Anyone familiar with even an introductory knowledge of quantum mechanics and the confined behavior of electrons is aware of the "particle in a box" problem for an infinite potential well. Electron confinement is achieved when the width of the infinite well becomes small enough to confine the electron wave such that the energy levels become quantized. This confinement width is referred to as the Bohr exciton radius. The Bohr exciton radius, typically defined as the distance between the proton and electron of an atom, can be calculated using Equation 1. The permittivity, ε, and reduced effective mass, m^*, are material specific. However, the relative permittivity, ε_0, reduced Planck's constant, $\hbar$, and the charge of an electron, q, are known constants. Calculated values of the Bohr exciton radius for the binary alloys of the III-nitrides and III-arsenides can be found in Table 1.

$$a_0 = \frac{4\pi\varepsilon\varepsilon_0\hbar^2}{m^* q^2} \qquad \text{(Equation 1)}$$

It can be difficult to solve a finite potential well, but graphical methods have been developed to make the solutions of the quantized energy states possible. First, a finite well must be defined with boundaries such as seen in Figure 4 and wave functions for the three boundaries such that:

Table 1. Calculated Bohr Radii for Select III-Nitride and III-Arsenide Materials.

Semiconductor	Symbol	Bandgap (eV)	Lattice Constant (Å)		Effective Mass (x m^*_o)		Reduced Effective Mass (m^*_r) (kg)	Static Dielectric Constant (F/m)	Bohr Excition Radius (nm)
Indium Nitride	InN	0.7	a_o	3.5446	m^*_e	0.11	9.38749E-32	15.3	7.86
			c_o	5.7034	m^*_h	1.63			
Gallium Nitride	GaN	3.44	a_o	3.189	m^*_e	0.20	1.59425E-31	8.9	2.69
			c_o	5.186	m^*_h	1.40			
Aluminum Nitride	AlN	6.2	a_o	3.11	m^*_e	0.40	3.27311E-31	8.5	1.25
			c_o	4.98	m^*_h	3.53			
Gallum Arsenide	GaAs	1.52	a_o	5.65325	m^*_e	0.07	5.42998E-32	13.18	11.70
			c_o		m^*_h	0.54			
Indium Arsenide	InAs	0.35	a_o	6.0583	m^*_e	0.03	2.30417E-32	15.15	31.69
			c_o		m^*_h	0.40			

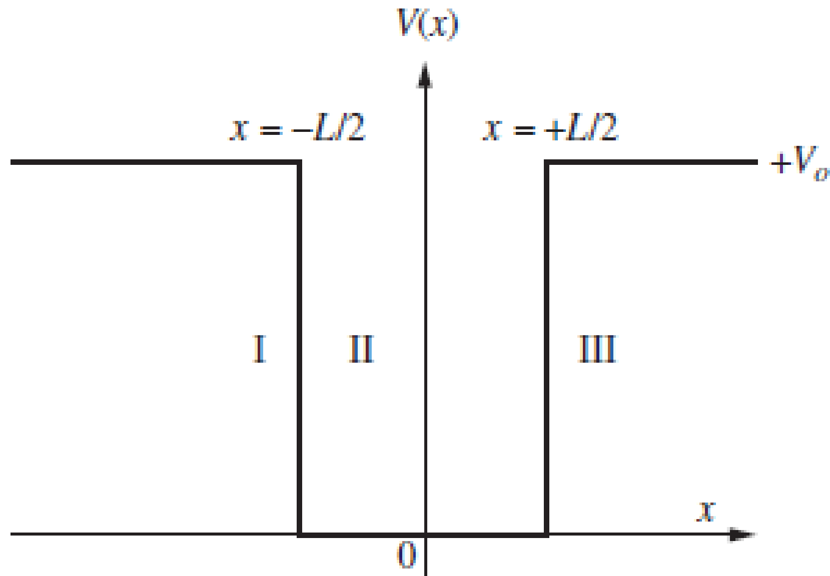

Figure 4. Graphical Representation of a Finite Potential Well.

$$\phi_{I} = Ae^{\rho x} \qquad \text{(Equation 2)}$$

$$\phi_{II} = B\sin(kx) + C\cos(kx) \qquad \text{(Equation 3)}$$

$$\phi_{III} = De^{-\rho x} \qquad \text{(Equation 4),}$$

where $k = \sqrt{2mE/\hbar^2}$, $\rho = \sqrt{2m(V_0 - E)/\hbar^2}$, m is the effective mass, E is the energy, $\hbar$ is the reduced Planck's constant, and V_0 is the well potential. Using boundary conditions for continuity and matrix algebra, the determinate of a four equation, four unknown (*A*, *B*, *C*, and *D*) system yields,

$$\left[k\sin\left(\frac{kL}{2}\right) - \rho\cos\left(\frac{kL}{2}\right)\right]\left[k\sin\left(\frac{kL}{2}\right) - \rho\cos\left(\frac{kL}{2}\right)\right] = 0 \qquad \text{(Equation 5)},$$

where L is the well width. Finally, through simplification, two equalities are found:

$$k\tan\left(\frac{kL}{2}\right) = \sqrt{k_0^2 - k^2} \qquad \text{(Equation 6)}$$

$$-k\cot\left(\frac{kL}{2}\right) = \sqrt{k_0^2 - k^2} \qquad \text{(Equation 7)}$$

These two equations lead to a set of graphical solutions at the intersections of the tangent and cotangent functions and $\sqrt{k_0^2 - k^2}$. An example of this method of solving for the quantized energy states can be found in Figure 5 with energy values calculated for InN QDs with heights up to the bulk Bohr exciton radius in Table 2. One dimensional confinement would typically only be acceptable for quantum well structures. However, the typical diameter for InN QDs as seen in this group's previous work have been much larger (>30 nm) than the Bohr exciton radius of ~8 nm [45]. Therefore, the QD can be considered as an effective well with quantum confinement only occurring in the growth direction or height of the QD.

2.2 Nucleation Theory

A phase change must occur for molecules or atoms to cluster, or nucleate. There are two types of nucleation found in nature: homogeneous and heterogeneous nucleation. Heterogeneous

nucleation is most readily found because it does not require a spontaneous nucleation to occur, but rather the nucleation occurs at a nucleating agent such as a foreign particle or surface. These nucleation agents act to lower the barrier to the initial formation of the new phase [16].

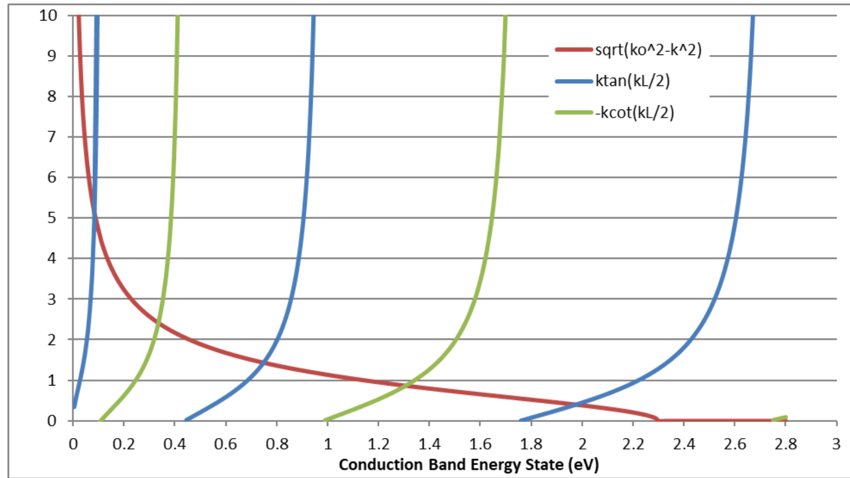

Figure 5. Example of Graphical Means for Solving Quantized Energy States Within the Conduction Band of the Exciton in InN QDs.

Table 2. Calculated Energy States for Indium Nitride Quantum Dots with a GaN Barrier for Heights at and below the bulk Bohr Exciton Radius.

Height (nm)	E_1 (eV)	E_1 (nm)	E_2 (eV)	E_2 (nm)	E_3 (eV)	E_3 (nm)	E_4 (eV)	E_4 (nm)	E_5 (eV)	E_5 (nm)	E_6 (eV)	E_6 (nm)
1	2.04	608										
2	1.33	933	2.87	431								
3	1.06	1174	2.06	602								
4	0.93	1336	1.59	779	2.60	477						
5	0.86	1445	1.32	936	2.07	599	2.98	416				
6	0.82	1520	1.16	1069	1.72	720	2.46	503				
7	0.79	1572	1.05	1178	1.49	834	2.08	597	2.78	446		
8	0.77	1610	0.98	1267	1.33	931	1.80	690	2.39	520	3.03	410

2.2.1 Heterogeneous Nucleation

In terms of heterogeneous nucleation, there are three growth modes. These three growth modes are characterized by the strongly atoms bond to the substrate or each other. In the Frank-van der Merwe growth mode, atoms bond stronger to the growth surface than each other. This

leads to a “wetting of the surface” and two-dimensional, layer-by-layer growth occurs. In the Volmer-Weber growth mode, atoms bond more strongly to each other than the growth surface. This leads to three-dimensional, island growth. These islands continue to grow and become stable when they reach a critical radius. The Sranski-Krastanov growth mode is considered both a layer and island growth mode. During initial growth, atoms bind to the growth substrate. This creates a two-dimensional, layered surface. Due to lattice mismatch, the deposited layer is strained. Once a critical thickness is reached, a three dimensional surface is created to alleviate the accumulated strain. The chemical potential of the growth surface is also a contributing factor to the change in growth mode dimensionality. The Stranski-Krastonov growth mode is used in fabricating self-assembled quantum dots [48].

Capillarity theory is a very useful way to make connections among variables such as substrate temperature, deposition rate, and critical nucleation size. Capillarity theory is useful for understanding semiconductor growth. First, the assumption is that active atoms in the vapor impinge on the growth substrate and cluster forming nuclei with radius, r. The change of the free energy accompanying this condensation process with a nucleate of mean dimension *r* can be written as [48]

$$\Delta G = \alpha_3 r^3 \Delta G_v + \alpha_1 r^2 \gamma_{vf} + \alpha_2 r^2 \gamma_{fs} - \alpha_2 r^2 \gamma_{sv} \quad \text{(Equation 8)}$$

where ΔG_v is the chemical free energy change per unit volume which drives the condensation reaction, γ_{vf} is the interfacial tension between vapor and film, γ_{fs} is the interfacial tension between the film and the substrate, γ_{sv} is the interfacial tension between the substrate and vapor, $\alpha_1 r^2$ is the curved surface area of the island, $\alpha_3 r^3$ is the volume of the island, and $\alpha_2 r^2$ is the circular area of the island on the substrate as seen in Figure 6. The geometric constants are given by α_1, α_2, and α_3

[48]. A more descriptive breakdown of the Gibbs Free Energy equation is shown in Figure 7.

At equilibrium, the Young's equation between the interfacial tensions can be written as

$$\gamma_{sv} = \gamma_{fs} + \gamma_{vf} \cos\Theta \qquad \text{(Equation 9)}$$

where the angle Θ is dependent on the surface properties of the impinging atoms/molecules and the growth substrate as seen in Figure 6 [48].

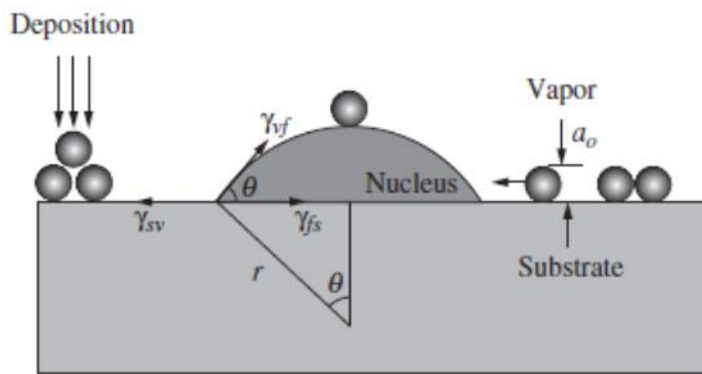

Figure 6. Illustration of Capillarity Theory [48].

$$\Delta G = \alpha_3 r^3 \Delta G_v + \alpha_1 r^2 \gamma_{vf} + \alpha_2 r^2 \gamma_{fs} - \alpha_2 r^2 \gamma_{sv}$$

Free energy change due to nucleating a structure

Change in chemical free energy due to nucleation

Change in free energy due to new surface area

Change in free energy under the nuclei

Figure 7. Descriptive Breakdown of the Gibbs Free Energy Equation.

The growth modes discussed above can be distinguished using the Young's equation. Frank van de Merwe growth mode occurs when impinging atoms "wet" the surface and the

resulting contact angle, Θ , equals zero. This condition is seen in Equation 10 [48].

$$\gamma_{sv} = \gamma_{fs} + \gamma_{vf} \qquad \text{(Equation 10)}$$

Volmer-Weber (VW) growth mode occurs when impinging atoms form island and the resulting contact angle is greater than zero. This condition is seen in Equation 11 [48].

$$\gamma_{sv} < \gamma_{fs} + \gamma_{vf} \qquad \text{(Equation 11)}$$

Stranski-Krastanov (SK) growth mode occurs when the strain energy per unit area of film growth is larger than the interfacial tension between the vapor and film and the following inequality is fulfilled [48].

$$\gamma_{sv} > \gamma_{fs} + \gamma_{vf} \qquad \text{(Equation 12)}$$

As one can easily see, capillarity theory gives a good "description" of the tension relief mechanism, which leads to an SK growth mode condition. However, many variable growth parameters can be manipulated to change the size, density and even shape during molecular beam epitaxy of SK quantum dots. Substrate temperature and deposition rate are the main contributors to affecting the deposition process. In heterogeneous nucleation, the change in the barrier to nucleation, ΔG^*, can be expressed as the following equality:

$$\Delta G^* = \frac{16\pi(\gamma_{vf})^3}{27\alpha_3^2(\Delta G_V + \Delta G_S)^2}\left(\frac{2 - 3\cos\theta + \cos^3\theta}{4}\right) \qquad \text{(Equation 13)}$$

where ΔG_V is the chemical free-energy change per unit volume and ΔG_S is the strain free-energy change per unit volume. The first factor of the product is derived from homogeneous nucleation

and the second factor is called the “wetting factor” and comes from the contact angle and geometric constants of the heterogeneous nucleation theory mentioned above [49]. But, how is ΔG* affected by changes in substrate temperature and deposition rate? The chemical free-energy change per unit volume, ΔG_V, can be expressed as,

$$\Delta G_V = -\frac{k_B T}{\Omega} \ln\left(\frac{\dot{R}}{\dot{R}_c}\right) \qquad \text{(Equation 14)}$$

where $\dot{R}$ and $\dot{R}_C$ are the impingement flux and desorption flux of metal atoms, respectively. Solving for Equation 8 and using the condition in which δΔG/δr = 0, the critical radius, r*, for stable nuclei can be determined [49].

$$r^* = \frac{-2(\alpha_1 \gamma_{fv} + \alpha_2 \gamma_{fs} - \alpha_2 \gamma_{sv})}{3\alpha_3 \Delta G_V} \qquad \text{(Equation 15)}$$

Finally, through direct differentiation of Equation 15 and assuming typical values for the tensions and the entropy change for vaporization, four inequalities can be found:

$$(\delta r^* / \delta T)_{\dot{R}} > 0 \qquad \text{(Equation 16)}$$

$$(\delta \Delta G^* / \delta T)_{\dot{R}} > 0 \qquad \text{(Equation 17)}$$

$$(\delta r^* / \delta \dot{R})_T < 0 \qquad \text{(Equation 18)}$$

$$(\delta \Delta G^* / \delta \dot{R})_T < 0 \qquad \text{(Equation 19)}$$

These four inequalities predict a number of common effects observed during film deposition. Equations 16 and 17 show that the nucleus radius (dot size) and barrier to nucleation

increase with increased substrate temperature at a constant deposition rate. Furthermore, Equations 18 and 19 show that the nucleus radius and barrier to nucleation decrease with an increase in deposition rate at a constant substrate temperature. The barrier to nucleation is inversely proportional to the nucleation density. Therefore, the nucleation density should increase with a decrease in nucleation barrier, and vice versa.

2.3 Molecular Beam Epitaxy

Molecular Beam Epitaxy (MBE) has been proven to be a very effective method of producing high quality epitaxial films. Precise control over growth parameters such as growth rate, growth temperature, and atomic impingement flux, make MBE an ideal system to perform a semiconductor growth study. In addition to precise control over growth parameters, MBE growth is performed in ultra-high vacuum (UHV). Typically maintained at standby pressures of 10^{-10}-10^{-11} torr, the MBE environment is devoid of high levels of impurities. Impurities can lead to many detrimental effects in semiconductor crystal growth such as reducing carrier mobilities, unintentional doping, non-radiative recombination, etc. The UHV environment also increases the mean free path of impinging atoms by reducing the likelihood of scattering off of a free particle before reaching the growth surface.

The following sections will discuss the MBE system components, in-situ RHEED analysis, and growth calibrations.

2.3.1 MBE System Components

A basic MBE system is shown in Figure 8. MBE systems utilize a modular design in order to reduce outside contamination, provide independent control, and allow future system

expansion. The Intro/cassette load-lock, Buffer/transfer, and growth chambers are separated by UHV gate valves. Typical additions to an MBE system are made for in-situ material characterization or metallization.

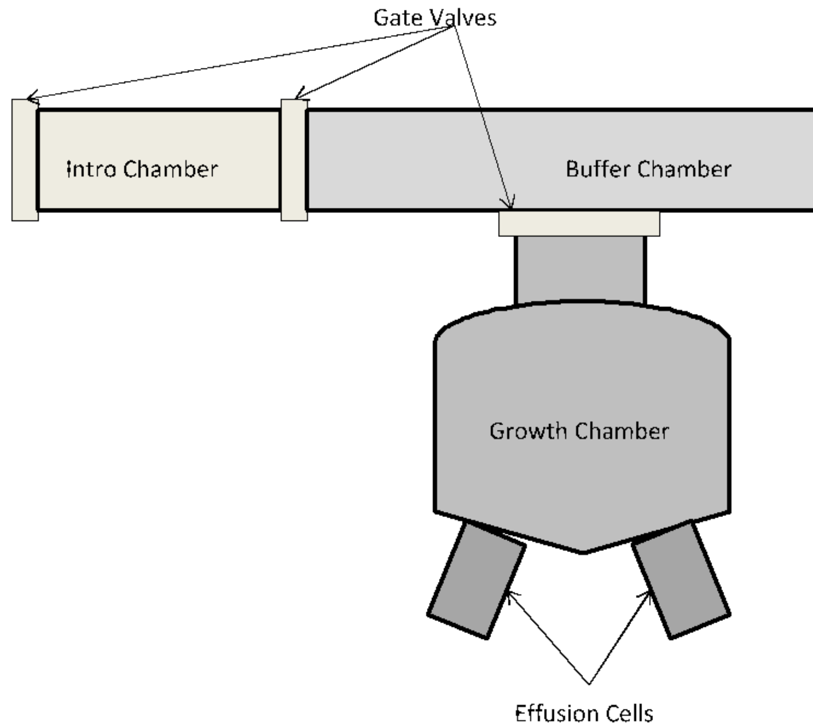

Figure 8. Graphical Illustration of Modular MBE Configuration.

Source material delivery is performed by effusion cells. These effusion cells are often referred to as Knudsen cells. Each Knudsen cell is loaded with high purity elemental material. For the III-N MBE which was used in this research, the available source materials were aluminum, gallium, and indium.

Like an effusion cell, a radio frequency (RF) plasma source, can be utilized to deliver active atomic species such as oxygen and nitrogen. The RF plasma source is necessary due to the diatomic nature of both oxygen and nitrogen at equilibrium. The RF plasma source uses high

power and frequency to ionize the source gas. The ionized gas is called a plasma. Through the process of ionization, diatomic molecules are separated into monoatomic, active source material.

Using effusion cells and an RF plasma source, III-nitride materials can be produced with very precise film thicknesses. This precision is due to the already discussed manipulation of growth parameters. In addition, precise layer thicknesses are produced by the slow, very accurate growth rate. Typical growth rates are less than 1 μm/hr.

2.3.2 In-situ RHEED Analysis

As mentioned in the previous section, additional equipment is used in MBE for in-situ material characterization. One of these characterization techniques is reflective high energy diffraction (RHEED) analysis. In-situ RHEED analysis helps the user in monitoring crystallinity and morphology before, during, and after the semiconductor growth process.

RHEED analysis utilizes the principle of Bragg diffraction. Using a shallow grazing angle ($\Theta < 1°$), a beam of high energy electrons probes the growth surface. The diffraction pattern created is shown on a phosphor screen. The plane spacing for III-nitride materials is given by the following formula for hexagonal unit cells [50].

$$d_{hkl}^{hex} = \sqrt{\frac{3}{4}\frac{a^2}{h^2 + hk + k^2} + \frac{c^2}{l^2}} \qquad \text{(Equation 20)}$$

where h, k, and l are the Miller indices and a and c are the lattice constants of the hexagonal material (indium nitride, gallium nitride, or aluminum nitride). These reciprocal plane spacing measurements are very useful in determining the composition of deposited material and determining whether a surface structure is “relaxed” or “strained” to the growth substrate.

In addition to crystallinity measurements, RHEED analysis is very beneficial in analyzing surface morphology, stoichiometric cell temperatures, and growth rate. Use of RHEED in determining stoichiometric cell temperatures will be discussed in the following section. Surface morphology is indicated in RHEED through real space analysis. Using a static RHEED image, a streaky pattern indicates a 2-D, planar surface, whereas a spotty pattern indicates a 3-D, rough surface. Examples of these static RHEED observations are shown in Figure 9.

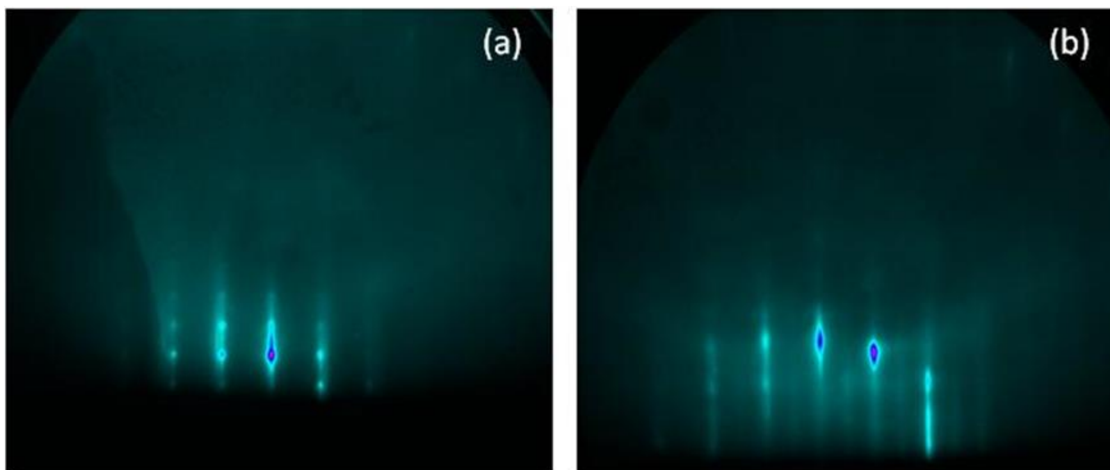

Figure 9. RHEED Example of 3D Surface (a) and 2D Surface (b) Grown by MBE.

Growth rate can be determined through the change in RHEED intensity during disorder/order oscillations. During the growth of 2-D, planar films, the intensity of the RHEED exhibits a sinusoidal change, often referred to as RHEED oscillations. One period of the sinusoidal wave represents a completed monolayer of film thickness. Given the frequency of oscillation and the c-plane lattice spacing, a real-time growth rate can be determined. An example of RHEED oscillations and surface reconstruction is shown in Figure 10.

2.3.3 MBE Growth Calibrations

In order to determine the growth parameters used in this experiment, two calibration routines were used. The first calibration routine involved determining the effusion cell flux for indium and gallium. Effusion cell flux was measured as a Beam Equivalent Pressure (BEP). In order to determine this pressure, a program was written within the MBE control software, MOLLY (Veeco, Plainview, NY). This program started by measuring the average background pressure. Once the average background pressure was measured, the effusion cell shutter opened, and the pressure was measured again. The difference in pressures was defined as the BEP for the effusion cell at the given effusion cell temperature. Multiple effusion cell temperatures were measured, and a graph was created for the effusion cell BEP as a function of effusion cell temperature as seen in Figure 11.

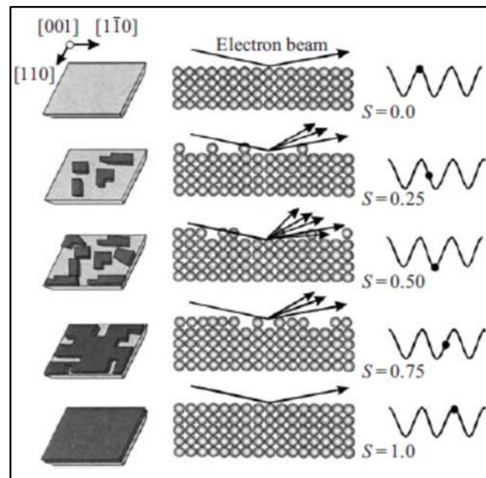

Figure 10. In-situ RHEED Analysis Using RHEED Oscillations to Monitor Growth Rate [50].

The data was modeled using a logarithmic function of the form

$$y = a\ln(x) + b \qquad \text{(Equation 21)}$$

The coefficients, a and b, of the fitted equation were used to determine the expected effusion cell BEP at any given effusion cell temperature within the measured range.

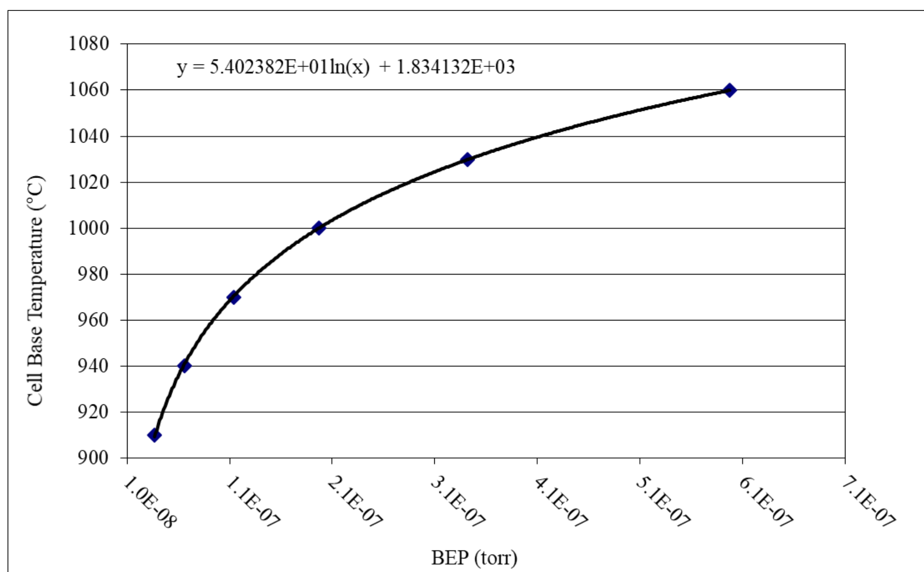

Figure 11. Calibration Result for an MBE Effusion Cell.

The second calibration routine utilized was determining the stoichiometric growth point for GaN. Gallium nitride was chosen over InN due to the growth temperature of GaN being high enough to allow for adequate desorption of excess gallium during the calibration routine. During the stoichiometric calibration, RHEED analysis was utilized. It was shown in the previous section that RHEED intensity decreases or increases with surface disorder or order. RHEED intensity is also affected by the accumulation of excess metal on the growth surface. This decrease in intensity is due to the scattering caused by the amorphous nature of the liquid metal. The initial gallium effusion cell temperature was chosen to be “Metal-Rich.” During a 30 second deposition time, both gallium and nitrogen shutters were opened, and the RHEED intensity

decreased as excess gallium accumulated on the surface. Once the shutters closed, the RHEED was monitored for the recovery of the initial intensity. This recovery time was termed the "desorption time." Gallium effusion cell temperatures were reduced after each 30 second deposition until a desorption time of close to zero was reached. The effusion cell temperatures and desorption times were plotted and fitted with a linear equation as seen in Figure 12. This stoichiometric calibration routine was used for each growth temperature used within this research.

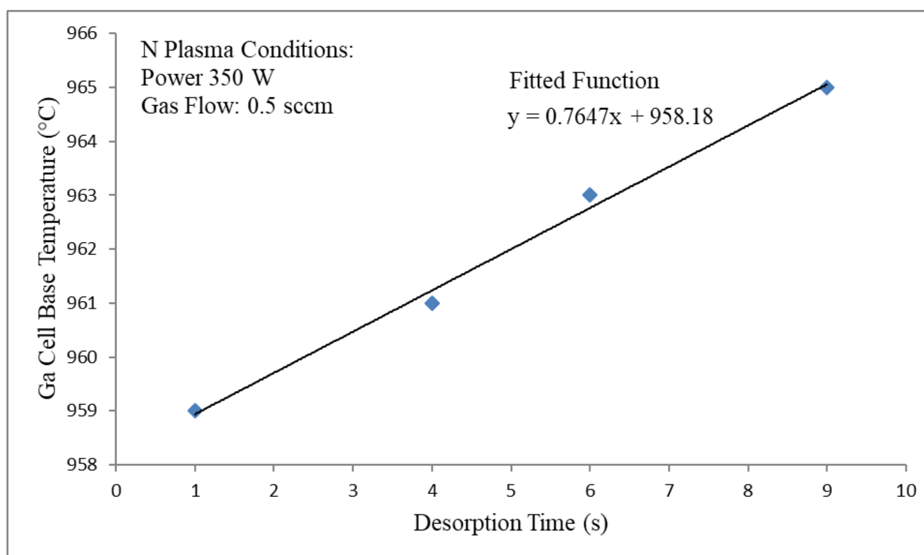

Figure 12. Result of a Stoichiometric Growth Point Calibration.

The gallium effusion cell stoichiometric temperatures were used to determine the associated BEP found in the first calibration routine. Using the gallium BEP and the ionization cross sectional areas of gallium and indium, equivalent stoichiometric cell temperatures were found for the indium effusion cell.

Chapter 3: Characterization Methods and Statistical Analysis

3.1 Atomic Force Microscopy

Atomic Force Microscopy (AFM) is a useful tool for analyzing non-conductive surfaces at the nanoscale. Much like a record player, AFM utilizes a cantilever with a very sharp tip. Cantilevers are typically made of silicon or silicon nitride. AFM probes are usually characterized by their construction material, resonant frequency, and stiffness. The AFM is able to provide accurate and precise measurements due to the piezoelectric elements of the system and the PID control system.

The AFM has three measurement modes: Contact, Non-Contact, and Tapping. Contact mode measures the surface morphology through cantilever deflection while the probe is in contact with the surface. Contact mode can damage a “soft” surface. Non-Contact mode measures the surface morphology through van der Waals, dipole-dipole, and electrostatic interactions without contacting the surface. Non-Contact mode suffers with accuracy when a liquid layer is present on the surface. Tapping mode utilizes elements of both contact and non-contact modes without suffering the limitations of these other modes. Tapping mode was used during this research.

Tapping mode consists of an oscillating cantilever which oscillates at or near the resonant frequency of the probe. This resonant frequency is referred to as the drive frequency. While oscillating, a piezoelectric actuator keeps the tip in contact with the surface at the bottom of its oscillation. A PID feedback loop maintains the constant oscillation signal from a split photodiode detector. The final image is generated from the intermittent contacts of the probe tip with the measured surface.

AFM scanning error can be produced by the size and shape of the AFM tip and any mechanical or electrical noise that may be present during testing. AFM probes in this research were made of silicon, had a drive frequency of ~300 kHz, a radius of curvature of 10 nm, and a spring constant of 40 N/m.

3.2 Photoluminescence

The story of semiconductor light emission starts with the generation of electrons in the conduction band and holes in the valence band, which can occur through many mechanisms, including thermal excitation, current injection, and optical excitation. These “excited” carriers can be eliminated through a recombination process. There are many different recombination processes: Shockley-Read (SR) recombination, bimolecular recombination, and Auger recombination (AR). A recombination process can be further classified as a radiative or non-radiative recombination process depending on whether the recombination of the electron and hole produce electromagnetic radiation. A graphical representation of all three recombination processes is found in Figure 13 [51].

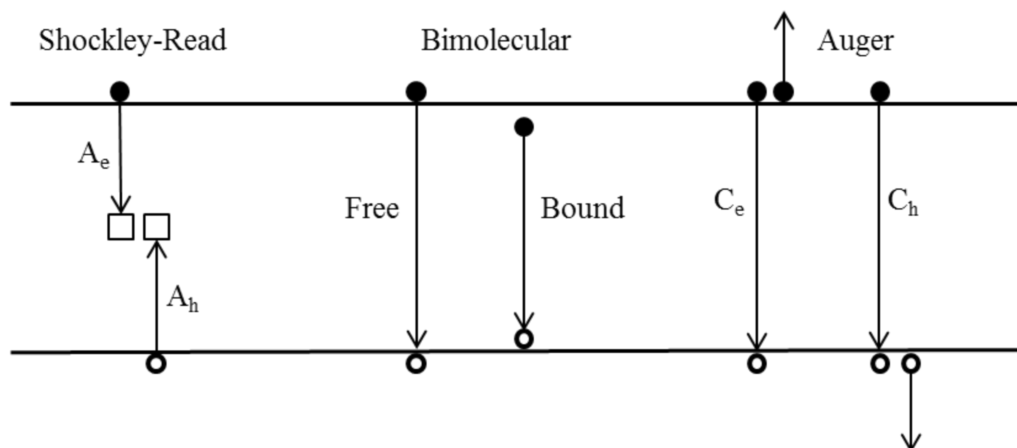

Figure 13. Graphical Representation of the Three-Carrier Recombination Processes.

Photoluminescence, or PL, is the process of emitting light after the absorption of photons. This absorption of photons leads to photoexcitation in which electrons are excited to a higher energy state. Photons are re-radiated when a relaxation of excited electrons to a lower energy state occurs. The measurement of this process, PL spectroscopy, is useful in characterizing optically active semiconductors. Some of the fundamental properties which can be obtained from this measurement are crystalline order, strain, composition, doping, surface carrier depletion depth, layer thickness, and extended defects [52].

Simply, PL spectroscopy can be accomplished with an emitter (high energy light source) and a detector (measures the re-radiated photons). A chosen emitter must produce incident photons with sufficient energy. In order to excite gallium nitride, the emitted photons should have an energy of greater than 3.4 eV, or a wavelength of less than 365 nm. Light of this energy can be produced with a quadrupled YAG laser at 266 nm. Depending on the analysis required, complexity can be added to the system. Beam splitters, neutral density filters, cryostats, and pumps are typically added to a PL spectroscopy system.

3.3 InN QD Analysis Techniques

The measurement of crystalline structures on the growth surface, can be performed through various techniques: atomic force microscopy, scanning electron microscopy, scanning-tunneling microscopy, tunneling electron microscopy, etc. For the purposes of this research, atomic force microscopy (AFM) was utilized. AFM was used due to the non-conductive nature of the growth substrates in which the samples were grown on. Sapphire was part of the underlying growth surface, and is non-conductive.

Once AFM scans were taken, these surface scans had to be interpreted. Bruker's

Nanoscope Analysis software V1.5 (Bruker, Billerica, MA) was used for this purpose. Multiple scans were made of each sample in order to reduce uncertainty. Each scan was interpreted to determine average QD density, height, diameter, area, and contact angle made with the growth surface. The steps used in image processing and structural measurements are given below.

First, the raw image was flattened. An example is shown in Figure 14. A second order flattening was used due to the parabolic scan nature of the AFM piezo.

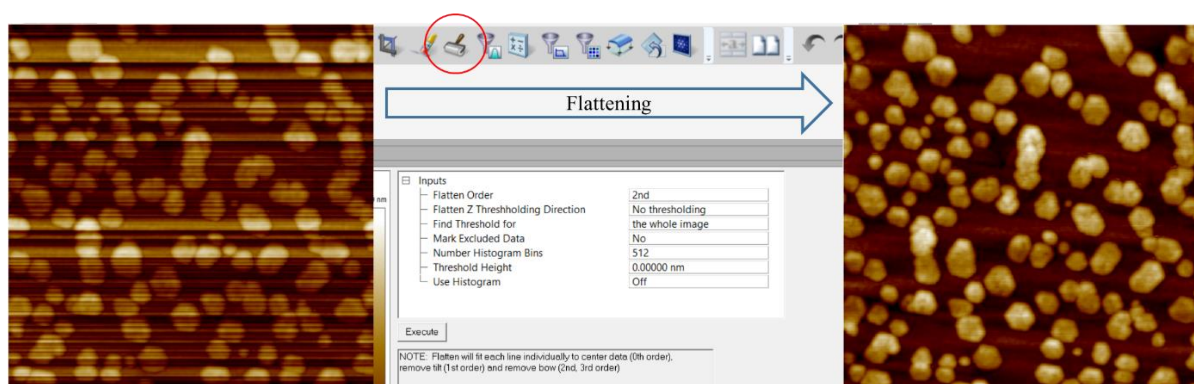

Figure 14. Using the Flattening Procedure in Nanoscope Analysis Software v1.50.

Once the image was flattened, the image was copied into MS Paint, and each individual QD was counted for the QD density. After determining the QD density, the “particle analysis” tool was used to determine the average height, diameter, and area. Figure 15 displays an example of this process in the Nanoscope software.

The threshold height was an important variable in the analysis of the quantum structures. Threshold height refers to the base reference. For QD heights, all QDs were measured using this reference as the zero point. For QD diameter and area, only material above this threshold was considered. The threshold height was increased or decreased in order to accurately measure structure dimensions. This was accomplished by observing the growth surface. If the threshold

height was lowered too much, the analysis software would “pick up” the growth surface. This would be indicated in the scan image. Once the optimal threshold height was determined, threshold heights greater than zero were added to the average height to account for lost accuracy due to surface undulation.

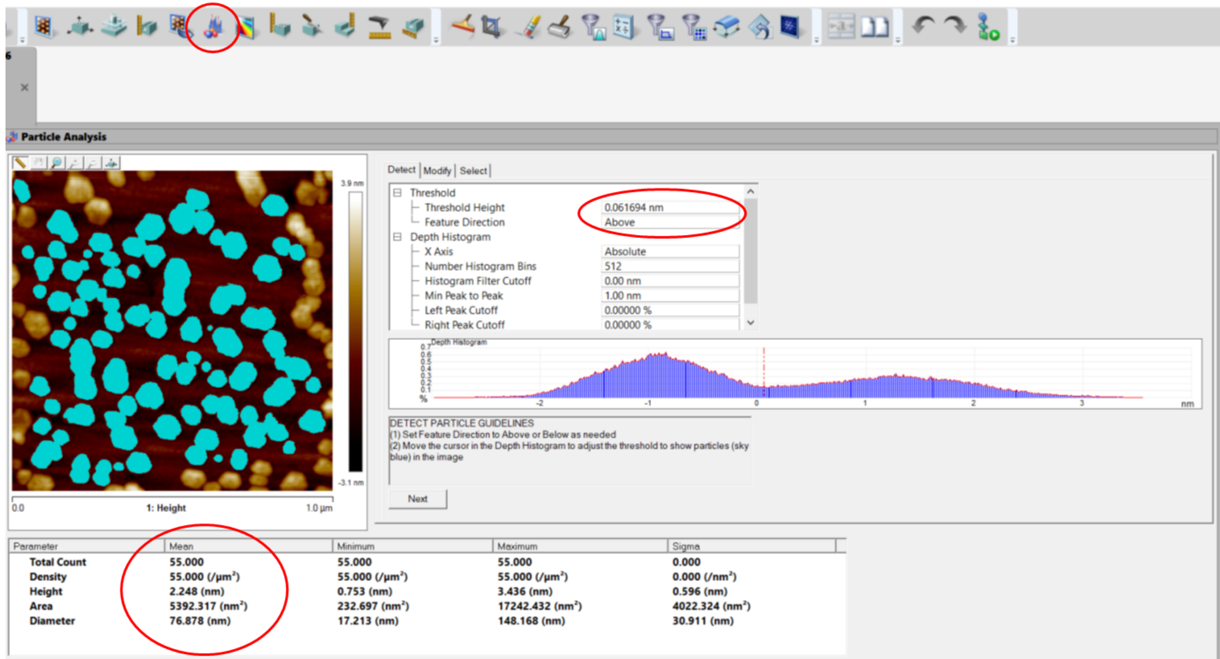

Figure 15. Using the Particle Analysis Tool in Nanoscope Analysis Software. (Circles indicate tool bar location, threshold height, and mean values of analyzed particles.)

For determining the diameter and area of the QD structures, special attention was given to coalesced or closely packed structures. In order to eliminate these structures, the “particle remove” function was used by selecting particles on the AFM scan which were conjoined/coalesced. The “particle remove” function was found under the “select” tab. An example of the step is given in Figure 16.

Finally, the contact angle was measured for each QD using the “section” tool. The average contact angle was calculated using Excel. An example of a contact angle measurement is

shown in Figure 17.

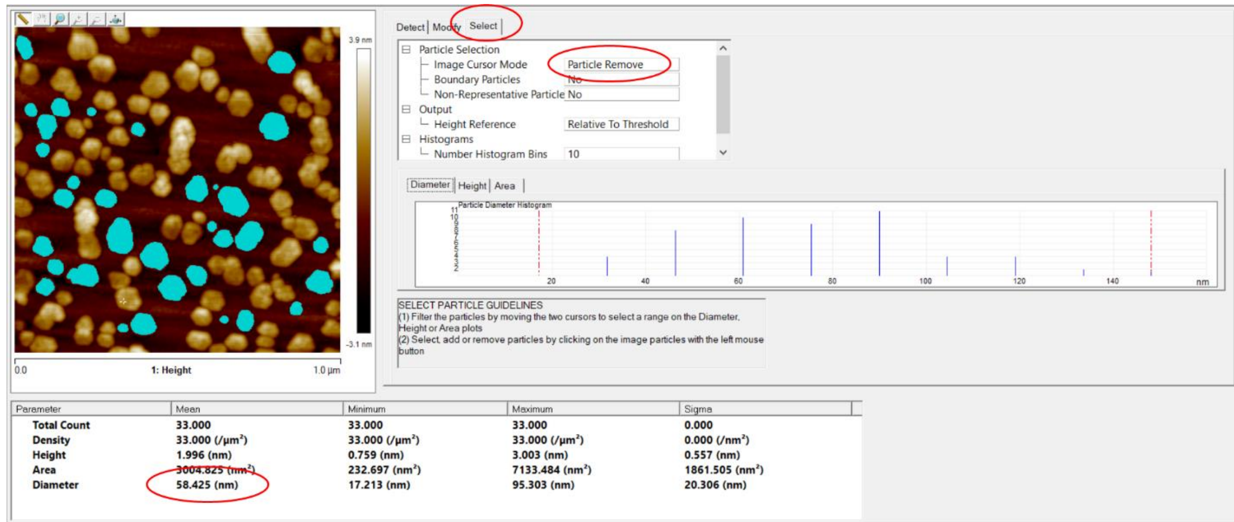

Figure 16. Example of Using Particle Remove Function in Nanoscope Analysis Software. (Circles indicate the select tab, particle remove option, and the mean diameter of particles analyzed.)

3.4 Confidence Intervals and Student's t Distribution

The bulk of analysis used in this research involved the use of statistical analysis. Both descriptive and inferential statistics were utilized to compare results. The descriptive statistics used in this research were the mean and standard deviation of measurements made to each sample. In every measurement, error is introduced. There are two types of error: Systematic and Random error. Systematic error, or bias, is introduced due to instrument error or user error. Typically, systematic error is always positive or always negative, and can be "calibrated" out of the final result. Random error is caused by naturally occurring variations in the measurement. Measurements with random error have a Gaussian distribution. If repeated measurements are made, the uncertainty in the measurement is reduced by sqrt(v/n), where v is the variation and n is the number of repeated measurements. The minimization of the variation, and "clustering" of

measurements around a center point, the mean, are due to the Central Limit Theorem.

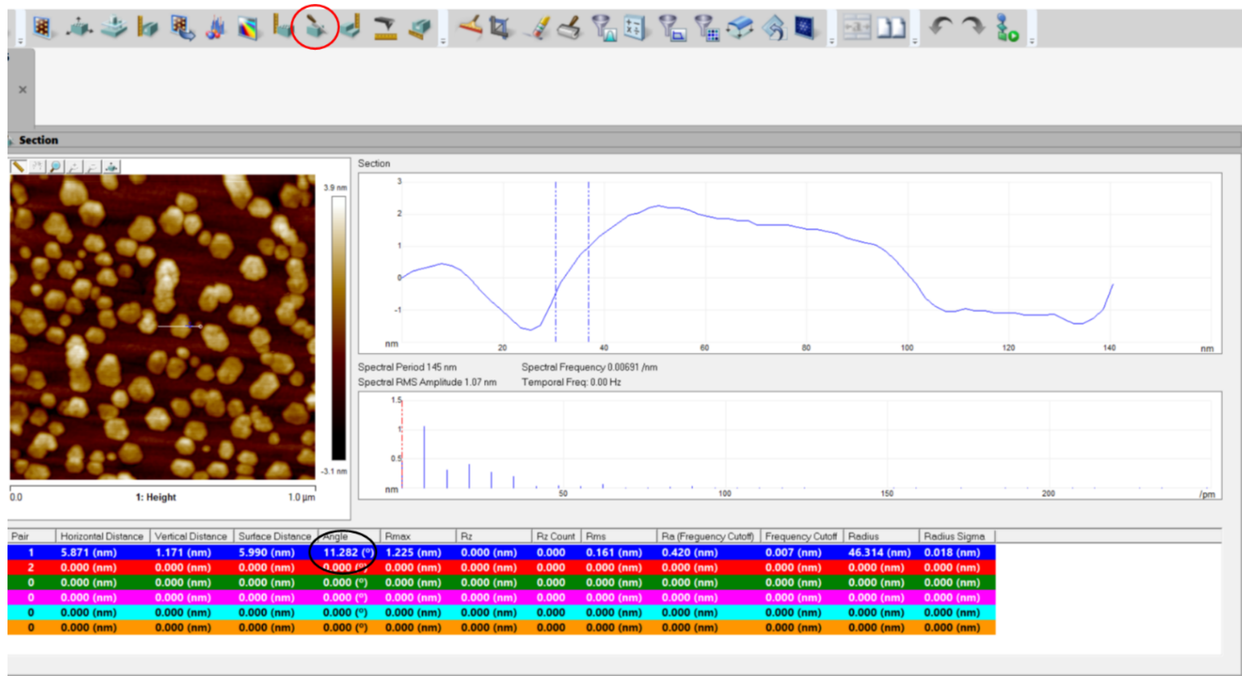

Figure 17. Example of Using the Section Tool in Nanoscope Analysis Software in Order to Measure Contact Angle of InN QDs.

In order to create a “good” Gaussian distribution, many measurements must be made ($n > 30$). However, for work such as the research presented herein, analysis of 30 AFM scans for ~20 samples would result in 600 AFM scans. That is too many scans for most people to analyze without losing their mind. To circumvent the analysis of this many scans, a Student’s t distribution can be used for sample sets of less than 30 measurements. The Student’s t distribution is a special form of the Gaussian distribution. The Student’s t distribution takes into account that the “clustering” of measurements around the mean is still in progress. More area is present in the tails of the Student’s t distribution than in the Gaussian (normal) distribution. An example of the two distributions is shown in Figure 18.

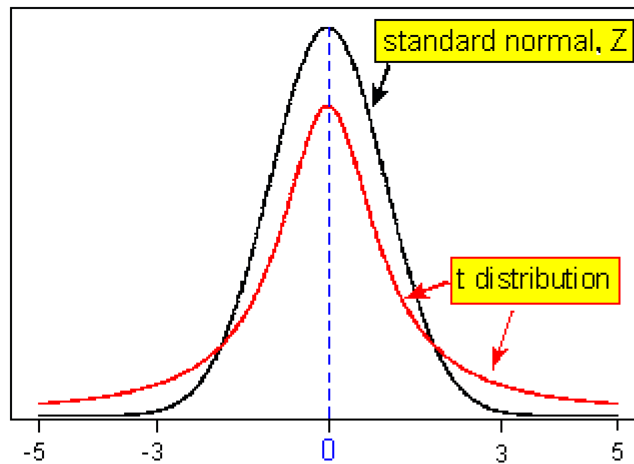

Figure 18. Examples of a Normal, Gaussian Distribution and a Student's t Distribution for Comparison [53].

Using a Student's t distribution and descriptive statistics, one can infer what a population mean would be through the use of Confidence Intervals. A confidence interval is a range of possible values that a population mean could be based on a "confidence level," number of measurements, sample mean, and sample standard deviation. The confidence interval can be calculated using the following equation:

$$CI = \overline{X} \pm (t_{stat})\left(\frac{s}{\sqrt{n}}\right) \qquad \text{(Equation 22)}$$

where CI is the confidence interval, $\overline{X}$ is the sample mean, t_{stat} is the scalar factor from the Student's t distribution table, s is the sample standard deviation, and n is the number of measurements. The Student's t scalar can be found using a Student's t table. With each consecutive measurement, a new distribution is created. Again, this is due to the clustering of measurements around the mean. Every t_{stat} has been calculated and can be easily found. In order

to find the t_{stat}, one must know the level of confidence required and the degrees of freedom (n-1). For this research, a confidence level of 95% was used. A 95% confidence level leaves an error of 5%. Given that a confidence interval is needed for a population mean, the range should be centered around the mean, and a two-tailed curve should be used. This would mean that the error of 5% should be equally divided into the two tails (0.025). Finally, knowing the t_{stat}, sample mean, the sample standard deviation, and the number of measurements, a confidence interval can be calculated. Again, a confidence interval is a range of possible value that one is confident that the population mean will fall within. In this research, the confidence interval (±) was used as the error bars for the mean of each sample.

Chapter 4: Results and Discussion

A study of the underlying growth mechanics involved in the nucleation density and critical radius of indium nitride (InN) quantum dots (QDs) was performed. InN samples were created through the use of molecular beam epitaxy (MBE) using a Veeco Generation II MBE chamber (Veeco, Plainview, NY) fitted with solid-source Knudsen cells and a radio frequency (RF) plasma source. All InN QDs were deposited on Metal Organic Chemical Vapor Phase Deposition (MOCVD) gallium nitride (GaN) templates.

Two growth environments were created for the deposition of InN QDs: Metal-Rich and Nitrogen-Rich. Metal-Rich growth was observed when InN QDs were deposited under indium rich growth conditions (In:N flux ratio of ~ 1.07). Nitrogen-Rich growth was observed when InN QDs were deposited using indium limited growth conditions (In:N flux ratio of < 1.0). To further understand the role of flux ratio on the development of InN QDs, the function of growth parameters (substrate growth temperature, deposition time and deposition rate) were studied for each growth environment. Reported growth rates were calculated using stoichiometric growth conditions. The nominal, stoichiometric growth rate was 0.25 MLs/s (monolayers per second). This growth rate was based on RF plasma conditions of 350 W and 0.5 sccm. Under Nitrogen-Rich growth environments, the growth rate was based on the product of the In:N flux ratio and nominal growth rate. For example, using a 0.30 In:N flux ratio would produce a growth rate of 0.075 MLs/s.

Changes in QD properties, nucleation density, height, diameter, volume, and contact angle/shape, were characterized using a Bruker Nanoscope V Atomic Force Microscope (AFM) (Bruker, Billerica, MA). In addition, Bruker's Nanoscope Analysis software V1.5 was utilized to

interpret surface scans obtained through AFM. Each InN QD sample was scanned multiple times in various locations. Mean values are reported for QD density, height and diameter for each sample in this section. In addition, the volume of deposited material was calculated and the contact angle of the quantum dots to the growth surface were investigated using the Bruker's Nanoscope Analysis software. Error bars are based on a 95% confidence interval using a student's t probability distribution.

This chapter presents and discusses the findings of the study.

4.1 Nitrogen-Rich Growth

4.1.1 Growth Temperature Dependence

Six temperature dependent samples were grown at temperatures, 375, 390, 400, 410, 425, and 440 °C. The growth time for each sample was 53 seconds, and the growth rate was 0.075 MLs/s. Each sample was grown to have the equivalent of 4 MLs of indium nitride deposited. Samples were grown with Nitrogen-Rich conditions, and an In:N flux ratio of 0.30. Under indium-limited growth conditions the growth rate was 30% of the nominal growth rate.

The results from the AFM characterization can be seen in Figure 19.

Quantum Dot Density

Table 3 displays the quantitative results of the substrate growth temperature treatment for the Nitrogen-rich growth mode for InN QDs as it pertains to QD density.

Figure 20, shown below, is a plot of QD density as a function of the inverse of growth substrate temperature. Error bars are not visible in Figure 20 and are represented within the data point.

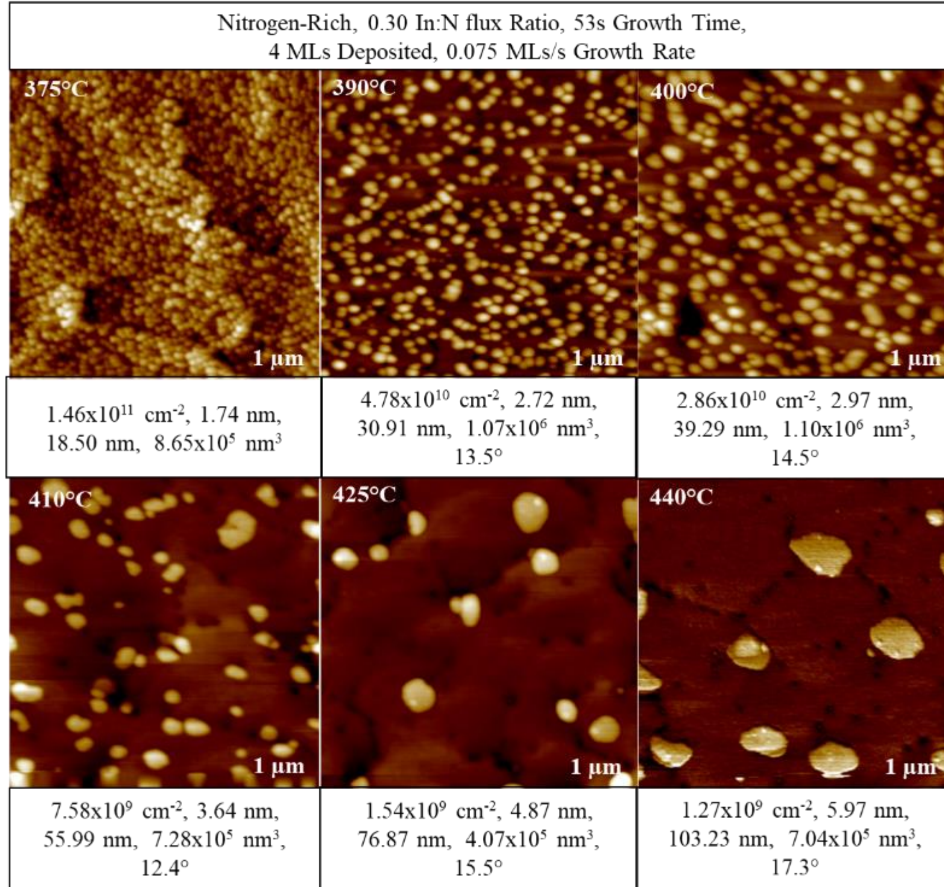

Figure 19. AFM scans of Nitrogen-Rich, Temperature Dependent Samples. (Each scan's deposition time, deposition thickness, and scan size are indicated within the scan. Descriptive statistics are given in each box for the following in this order: QD mean density, height, and diameter, total volume deposited, and mean contact angle of QD with the growth surface.)

Table 3. Nitrogen-Rich InN QD Density as a Function of Growth Temperature.

Sample ID	Substrate Temperature (°C)	1/kT (J^{-1})	Mean Density (cm^{-2})	Standard Deviation (cm^{-2})	Error (cm^{-2})
NH90	375	1.117E+20	1.46E+11	3.78E+10	± 2.97E+10
NH88	390	1.092E+20	4.78E+10	3.74E+09	± 1.60E+09
NH85	400	1.076E+20	2.86E+10	3.92E+09	± 1.68E+09
NH87	410	1.060E+20	7.58E+09	1.27E+09	± 5.46E+08
NH82	425	1.037E+20	1.54E+09	1.17E+08	± 5.01E+07
NH89	440	1.016E+20	1.27E+09	1.21E+08	± 4.76E+07

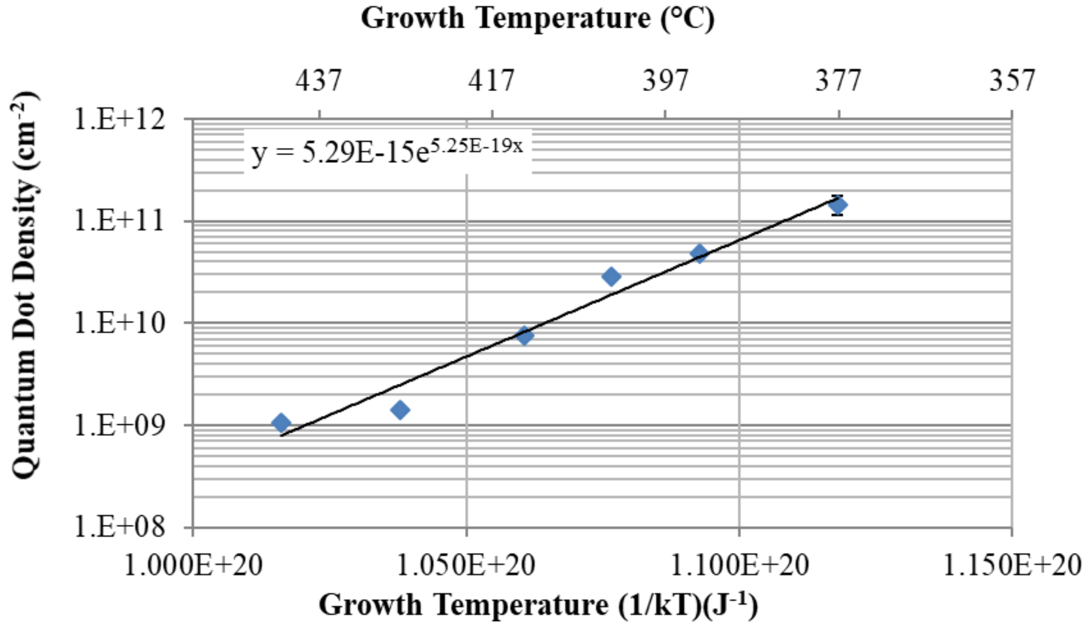

Figure 20. QD Density as a Function of 1/kT for Nitrogen-Rich InN QDs.

An exponential trend was observed for the temperature dependent, Nitrogen-Rich data set. This exponential trend was fitted with the exponential equation found in Figure 20. From this equation, the activation energy for the system was found to be 5.10×10^{-19} J, or 3.19 eV. The Nitrogen-Rich densities trend well with typical SK, heterogeneous nucleation, and follow the form of Equation 23.

$$N^* = n_0 \exp\left(\frac{-\Delta G^*}{k_B T}\right) \qquad \text{(Equation 23)}$$

Quantum Dot Height and Diameter

Table 4 and Table 5 display the quantitative results of the substrate growth temperature treatment for the Nitrogen-Rich growth for InN QDs as it pertains to height and diameter, respectively.

Table 4. Nitrogen-Rich InN QD Height as a Function of Growth Temperature

Sample ID	Substrate Temperature (°C)	1/kT (J^{-1})	Mean Height (nm)	Standard Deviation (nm)	Error (nm)
NH90	375	1.117E+20	1.74	0.28	± 0.22
NH88	390	1.092E+20	2.72	0.07	± 0.03
NH85	400	1.076E+20	2.97	0.09	± 0.04
NH87	410	1.060E+20	3.64	0.33	± 0.14
NH82	425	1.037E+20	4.87	0.33	± 0.14
NH89	440	1.016E+20	5.97	0.62	± 0.24

Table 5. Nitrogen-Rich InN QD Diameter as a Function of Growth Temperature

Sample ID	Substrate Temperature (°C)	1/kT (J^{-1})	Mean Diameter (nm)	Standard Deviation (nm)	Error (nm)
NH90	375	1.117E+20	18.50	0.82	± 0.64
NH88	390	1.092E+20	30.91	1.69	± 0.72
NH85	400	1.076E+20	39.29	1.51	± 0.65
NH87	410	1.060E+20	55.99	7.45	± 3.19
NH82	425	1.037E+20	76.87	2.83	± 1.21
NH89	440	1.016E+20	103.23	11.13	± 4.37

Figure 21 and Figure 22 graphically display the trends observed in the data found in Table 4 and Table 5.

The Nitrogen-Rich series shows a very strong exponential trend in regard to the change in quantum dot height and diameter. Both data sets, height and diameter, were experimentally fitted. For the quantum dot height data, the activation energy was found to be $1.18\text{x}10^{-19}$ J. The activation energy for the quantum dot diameter series was found to be $1.69\text{x}10^{-19}$ J. The exponential fit for height and diameter agree with an Ostwald ripening and an increase in capture area of mobile adatoms with an increase in temperature. Equation 24 represents the relationship of diffusion length, *X*, and substrate temperature, *T*. Equation 25 shows capture area, *A*, as a

function of diffusion length, *X*.

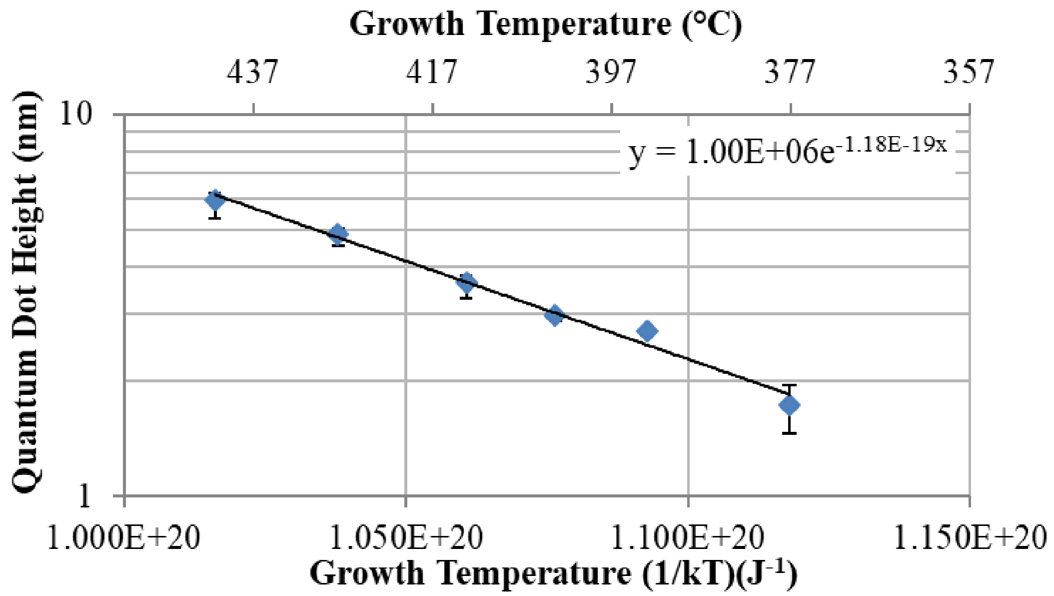

Figure 21. QD Height as a Function of 1/kT for Nitrogen-Rich InN QDs.

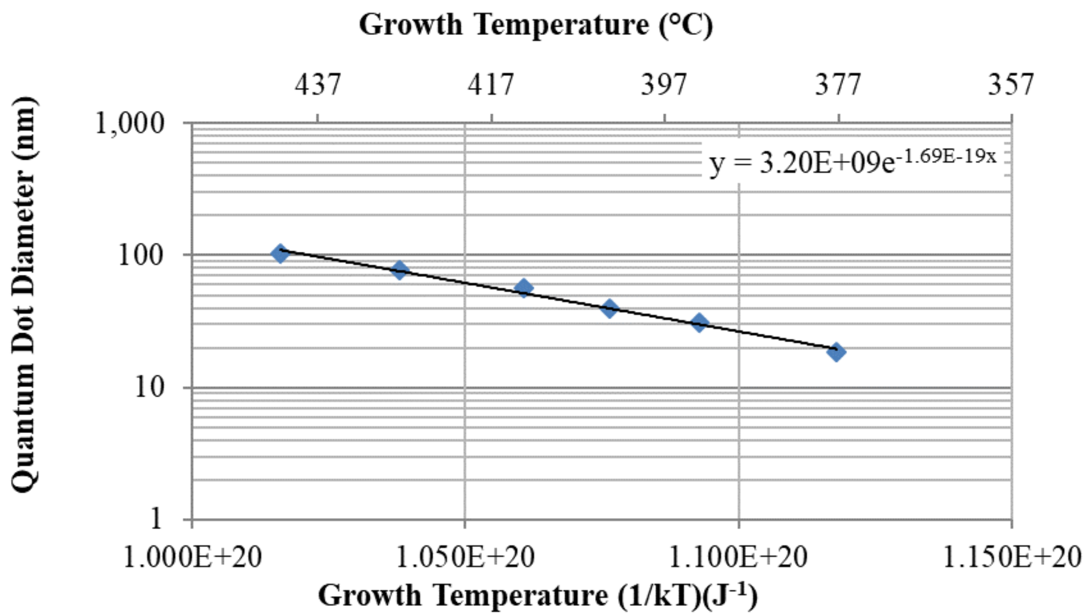

Figure 22. QD Diameter as a Function of 1/kT for Nitrogen-Rich InN QDs.

$$X = a_0 \exp\left(\frac{E_{des} - E_s}{2kT}\right) \qquad \text{(Equation 24)}$$

$$A = \pi(X)^2 \qquad \text{(Equation 25)}$$

From Figures 21 and 22, the observed trends for both QD height and QD diameter show an increase in dimensional size with increasing substrate growth temperature. Given that the nucleation density of the InN QDs decreased with increasing temperature, the increased size of both QD dimensions with temperature can only be explained by an increase in the nuclei capture area or capture radius, *X*. If the capture radius does not increase, then the size of the QDs would not change and adatoms would leave the growth surface before finding a stable nucleation site. A simple pictorial representation of this concept is shown in Figure 23 in which $T_2 > T_1$. Nucleation sites are represented by '*' and nucleation capture areas are represented by circles.

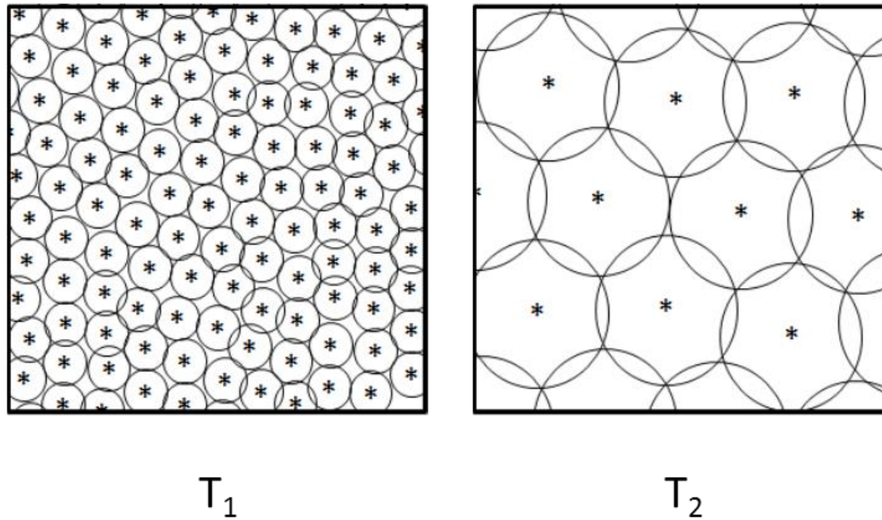

Figure 23. Graphical Representation of the Change in Nucleation Density and Capture Area as a Function of Growth Substrate Temperature.

Volume of Deposited Material

Calculations were made to account for all deposited material characterized through AFM. Volume calculations were made using the product of the average values for quantum dot density, surface area, and height. The volumes are reported as the volume of indium nitride material found in a 1 μm^2 area ($nm^3/\mu m^2$). Figure 24 graphically depicts the change in deposited material with a change in growth temperature for Nitrogen-Rich samples. Volumes were calculated for each sample except the sample produced with a substrate temperature of 375 °C. The tightly packed nature of the quantum dots produced too much uncertainty in the volume calculation based on AFM analysis.

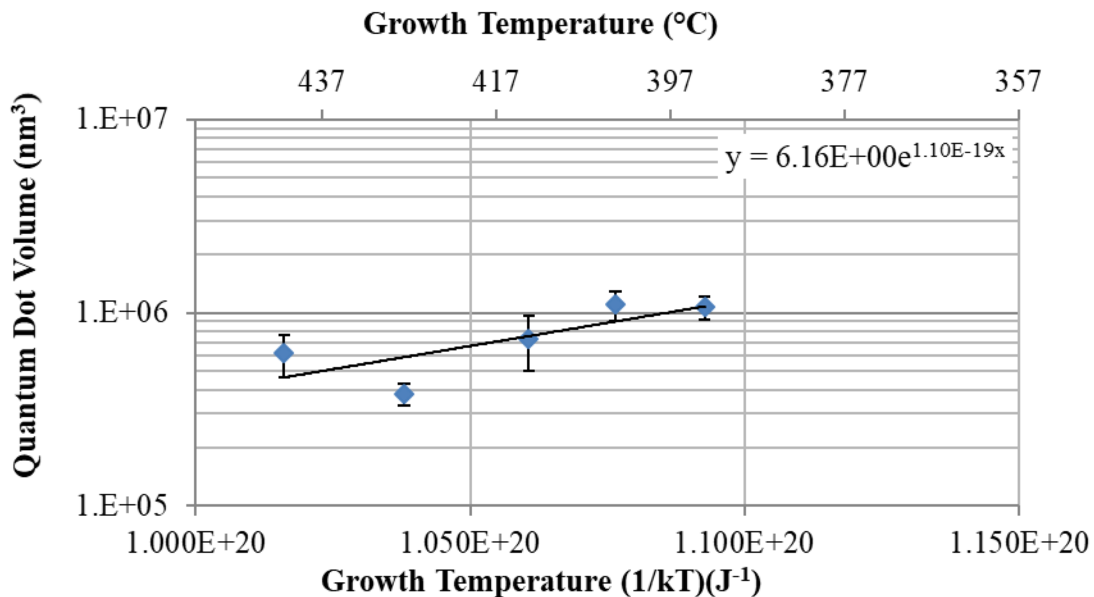

Figure 24. Volume of Deposited InN as a Function of 1/kT for Nitrogen-Rich InN QDs.

The calculated volumes did show a decreasing trend with increasing substrate temperature. However, no fitted equation was employed for this data set. As temperature was increased, the volume was observed to decrease starting at 400 °C. The loss of InN QD volume

was due to dissociation. However, this was slightly below the expected dissociation temperature that was expected of 430 °C.

Quantum Dot Contact Angle

Quantum dot contact angle was measured using the Bruker Nanoscope Analysis software. Contact Angles were measured and averaged for each sample in the series. Figure 25 displays the change in contact angle as a function of growth substrate temperature for the Nitrogen-Rich series.

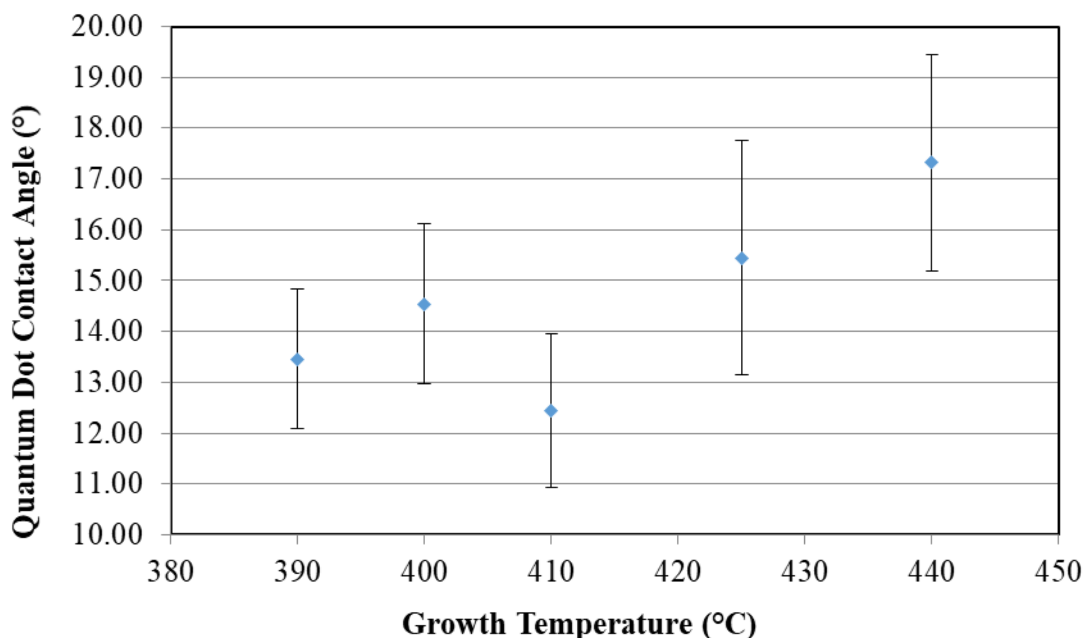

Figure 25. QD Contact Angle as a Function Substrate Temperature for Nitrogen-Rich InN QDs.

Due to the associated error within each measurement, no change on contact angle was found for the series. However, it is important to note that the average magnitude of the contact angle was approximately 14-15°.

4.1.2 Deposition Time Dependence

Three samples were created in order to observe the role in which deposition time has on the nucleation and growth of InN QDs. The three samples were fabricated at deposition times of 53, 66.25, and 79.5 seconds. These deposition times led to film depositions of 4, 5, and 6 MLs, respectively. Other growth conditions, growth temperature (400°C) and deposition In:N flux ratio (0.32), were held constant during this experiment. The results from the AFM characterization are shown in Figure 26.

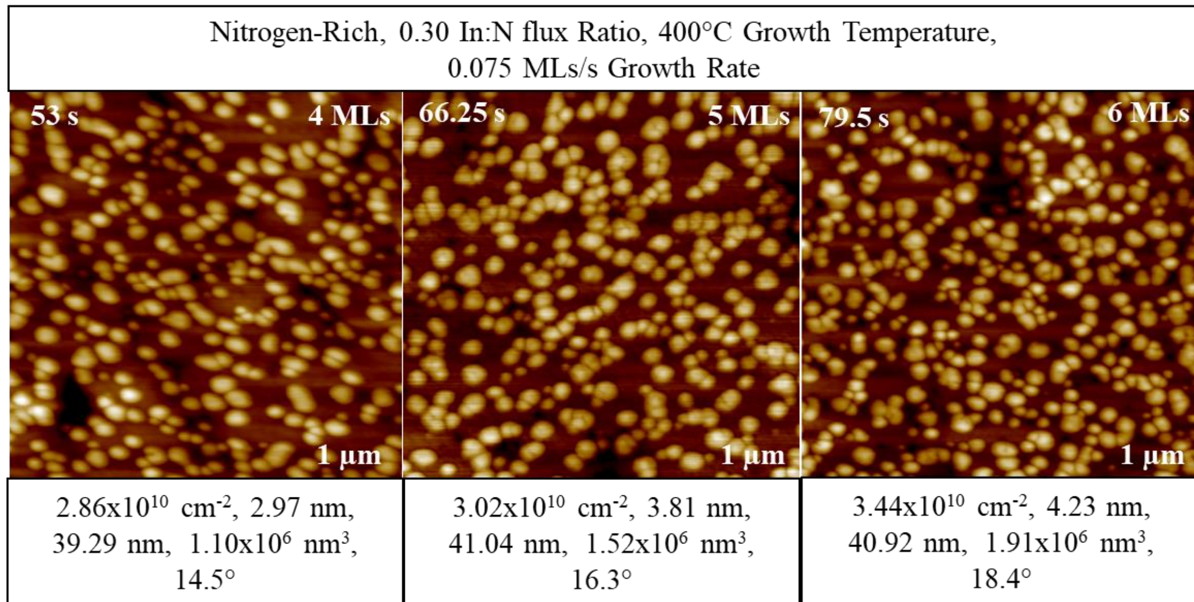

Figure 26. AFM Scans of Nitrogen-Rich, Time Dependent Samples. (Each scan's deposition time, deposition thickness, and scan size are indicated within the scan. Descriptive statistics are given in each box for the following in this order: QD mean density, height, and diameter, total volume deposited, and mean contact angle of QD with the growth surface.)

Quantum Dot Density

Table 6 displays the quantitative results of the deposition time growth parameter for the

Nitrogen-Rich growth environment for InN QDs as it pertains to quantum dot density.

Table 6. Nitrogen-Rich InN QD Density as a Function of Deposition Time.

Sample ID	Growth Time (s)	Mean Density (cm^{-2})	Standard Deviation (cm^{-2})	Error (cm^{-2})
NH85	53	2.86E+10	3.92E+09	± 1.68E+09
NH91	66.25	3.02E+10	1.24E+09	± 5.29E+08
NH92	79.5	3.44E+10	3.17E+09	± 1.36E+09

Results from Table 6 have been displayed in Figure 27.

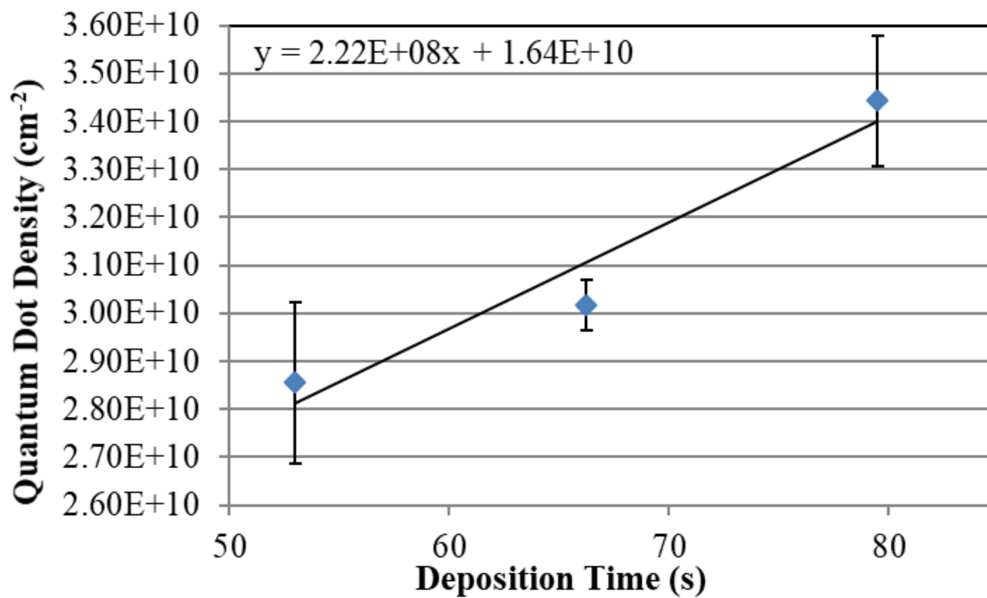

Figure 27. QD Density as a Function Deposition Time for Nitrogen-Rich InN QDs.

An increase in quantum dot density was observed in the Nitrogen-Rich system for increasing deposition times. Experimental fits of the data were performed. The linear fit equation is given in Figure 27.

The surface, during growth, is always evolving. The key to increasing nucleation density as

a function of increasing deposition time is that smaller structures "grow" to a stable size. Given a longer deposition time and that the impingement flux to the smaller dots is greater than the flux leaving due to ripening to larger dots, the "small" dots will become stable and the quantum dot density will increase. This increase in QD density is what was observed.

Quantum Dot Height and Diameter

Table 7 and Table 8 display the quantitative results of the deposition time treatment for the Nitrogen-Rich growth mode for InN QDs as it pertains to height and diameter, respectively.

Table 7. Nitrogen-Rich InN QD Height as a Function of Deposition Time.

Sample ID	Growth Time (s)	Mean Height (nm)	Standard Deviation (nm)	Error (nm)
NH85	53	2.97	0.09	± 0.04
NH91	66.25	3.81	0.16	± 0.07
NH92	79.5	4.23	0.25	± 0.11

Table 8. Nitrogen-Rich InN QD Diameter as a Function of Deposition Time.

Sample ID	Growth Time (s)	Mean Diameter (nm)	Standard Deviation (nm)	Error (nm)
NH85	53	39.29	1.51	± 0.65
NH91	66.25	41.04	2.43	± 1.04
NH92	79.5	40.92	1.91	± 0.82

Figure 28 and Figure 29 graphically display the quantitative results found in Tables 7 and 8.

A linear trend was modeled to fit the change in height of the Nitrogen-Rich time dependent data series. The model suggested that the quantum dot height changed at a rate of 50 pm/s.

A linear trend was modeled to fit the change in diameter of the Nitrogen-Rich time dependent data series. The model suggested that the quantum dot diameter of this series changed at a rate of 60 pm/s.

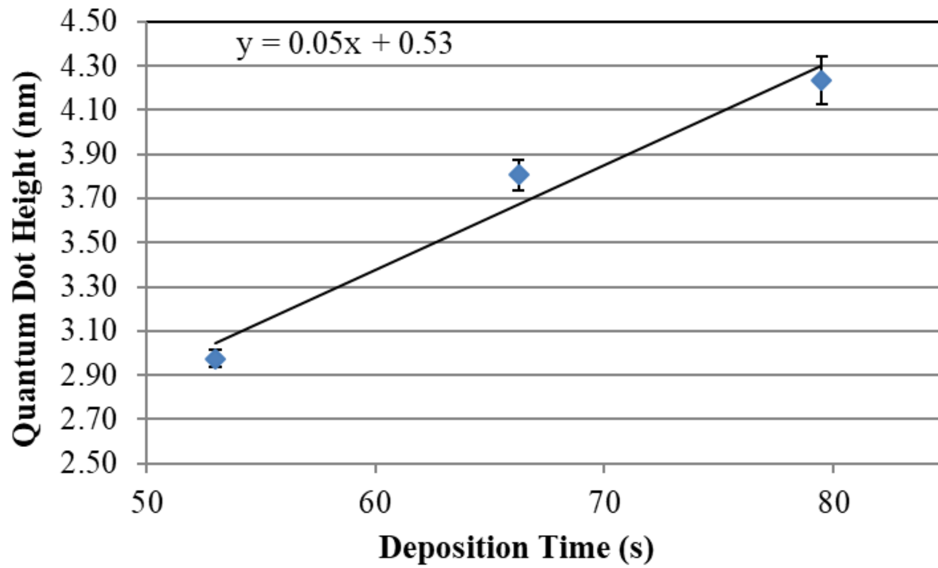

Figure 28. QD Height as a Function Deposition Time for Nitrogen-Rich InN QDs.

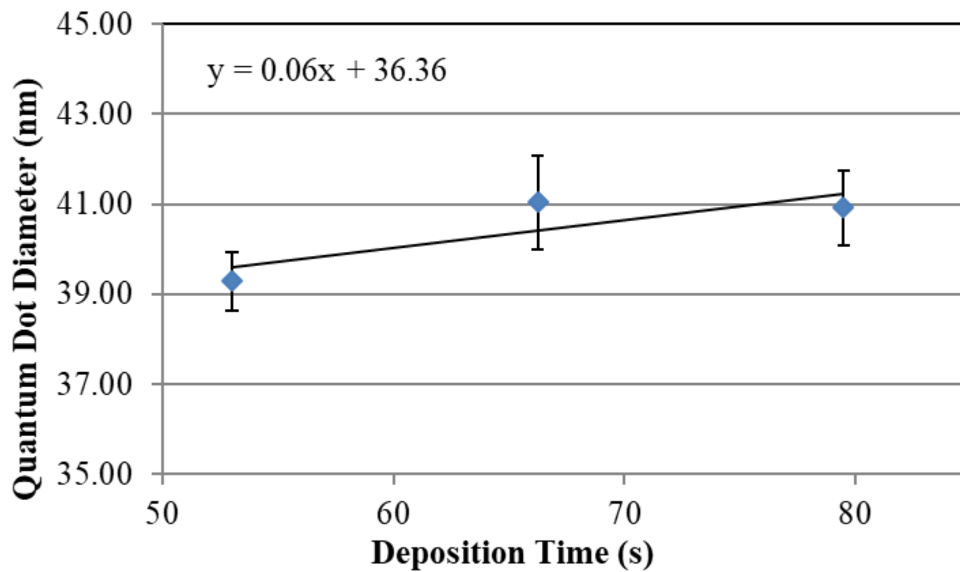

Figure 29. QD Diameter as a Function Deposition Time for Nitrogen-Rich InN QDs.

Both dimensional increases are consistent with the development of SK QDs by showing a linear increase in QD size as a function of deposition time.

Volume of Deposited Material

Calculations were made to account for all deposited material observed through AFM. Volume calculations were made using the product of the average values for quantum dot density, surface area, and height. The volumes are reported as the volume of indium nitride material found in a 1 μm^2 area ($nm^3/\mu m^2$). Figure 30 graphically depicts the change in deposited material with a change in deposition time for Nitrogen-Rich samples.

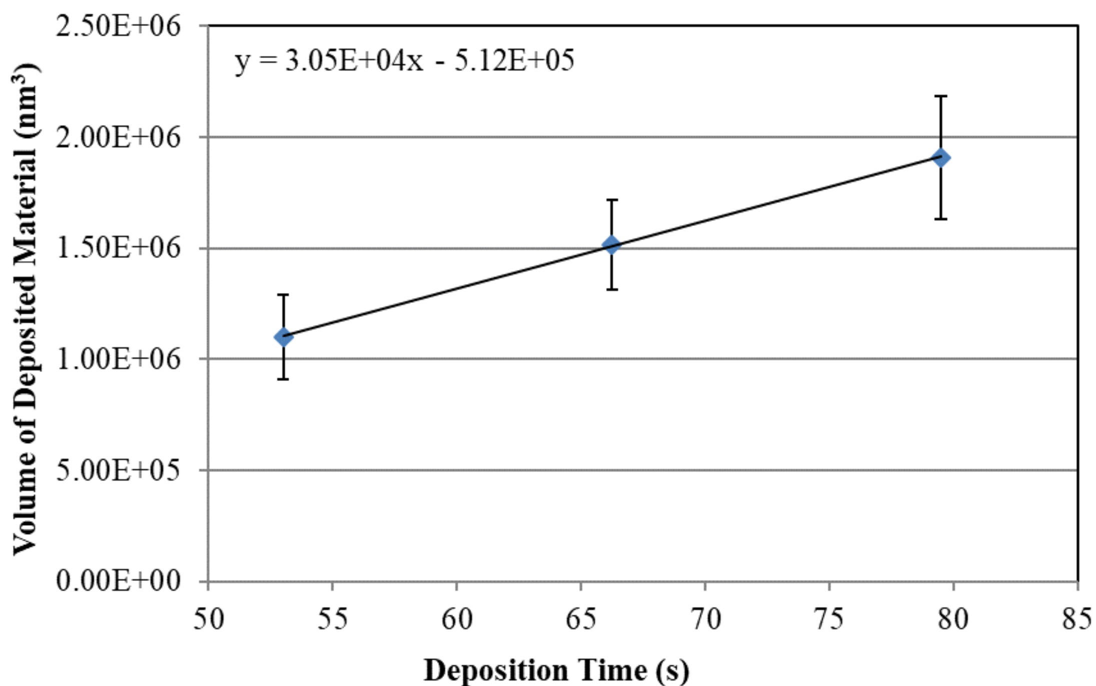

Figure 30. Volume of Deposited InN as a Function of Deposition Time for Nitrogen-Rich InN QDs.

A linear trend was observed for the volume of deposited material with increasing deposition time. From the fitted equation, the volume increased at a rate of 3.05×10^4 nm^3/s.

Given that the c-plane lattice spacing of InN is 2.85 Å, the modeled rate of change in volume corresponds to a growth rate of 0.10 MLs/s. This growth rate was much lower than the nitrogen-based growth rate of 0.25 MLs/s. However, due to the indium limited condition in the Nitrogen-Rich growth method, this was expected. A growth rate of 0.10 MLs/s corresponds to an In:N flux ratio of approximately 0.4 which was higher than the expected flux ratio of 0.32.

Quantum Dot Contact Angle

Quantum dot contact angle was measured using the Bruker Nanoscope Analysis software. Contact Angles were measured and averaged for each sample in the series. Figure 31 displays the change in contact angle as a function of deposition time for the Nitrogen-Rich series.

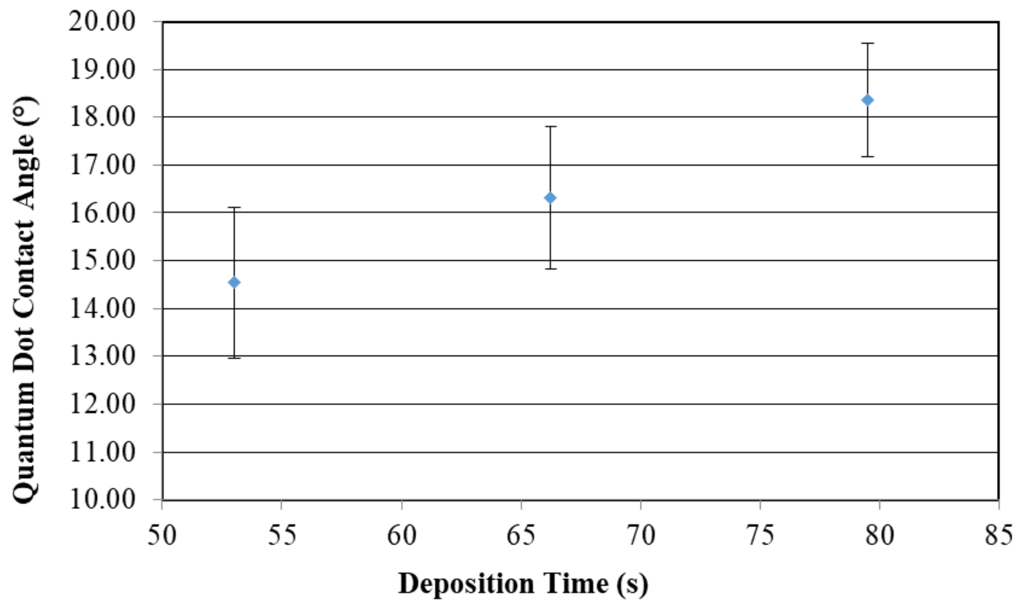

Figure 31. QD Contact Angle as a Function of Deposition Time for Nitrogen-Rich InN QDs.

A linear, increasing trend was observed in the quantum dot contact angle with increased deposition time.

4.1.3 Deposition Rate Dependence

Three samples were created in order to observe the role which deposition rate had on the nucleation and growth of InN QDs. Here, the deposition rate was controlled by varying the flux ratio of In to N, while keeping the N flux constant. Or, equivalently, by simply varying the In flux with constant N flux. This was valid here, since indium was the rate limiting species for N-rich conditions. The three samples were grown with In:N flux ratios which corresponded to InN growth rates of 0.063, 0.075, and 0.095 MLs/s. Other growth conditions (growth temperature, 400°C, and deposition thickness, 4 MLs) were held constant during this experiment. The results from the AFM characterization can be seen in Figure 32.

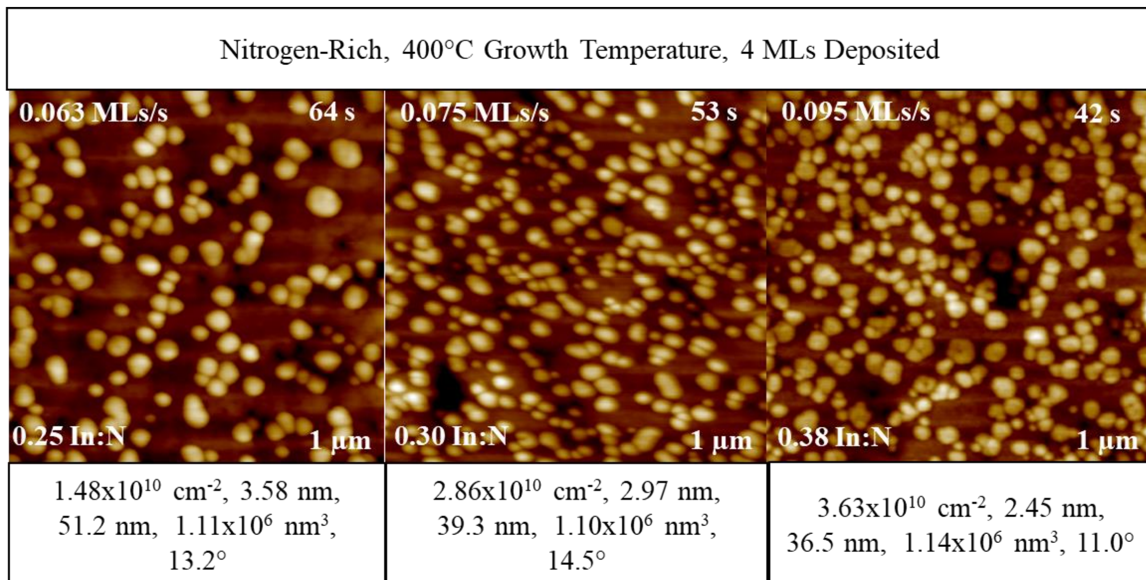

Figure 32. AFM scans of Nitrogen-Rich, Rate Dependent samples. (Each scan's deposition time, deposition thickness, and scan size are indicated within the scan. Descriptive statistics are given in each box for the following in this order: QD mean density, height, and diameter, total volume deposited, and mean contact angle of QD with the growth surface.)

Quantum Dot Density

Table 9 displays the quantitative results of the substrate growth temperature treatment for

the Nitrogen-Rich growth environment for InN QDs as it pertains to QD density.

Figure 33 is a plot of quantum dot density as a function of the deposition rate. Where error bars are not visible in Figure 33, they are represented within the data point.

Table 9. Nitrogen-Rich InN QD Density as a Function of Deposition Rate.

Sample ID	Growth Rate (MLs/s)	Mean Density (cm^{-2})	Standard Deviation (cm^{-2})	Error (cm^{-2})
NH94	0.0625	1.48E+10	8.38E+08	± 3.59E+08
NH85	0.0755	2.86E+10	3.92E+09	± 1.68E+09
NH93	0.0952	3.63E+10	1.73E+09	± 7.42E+08

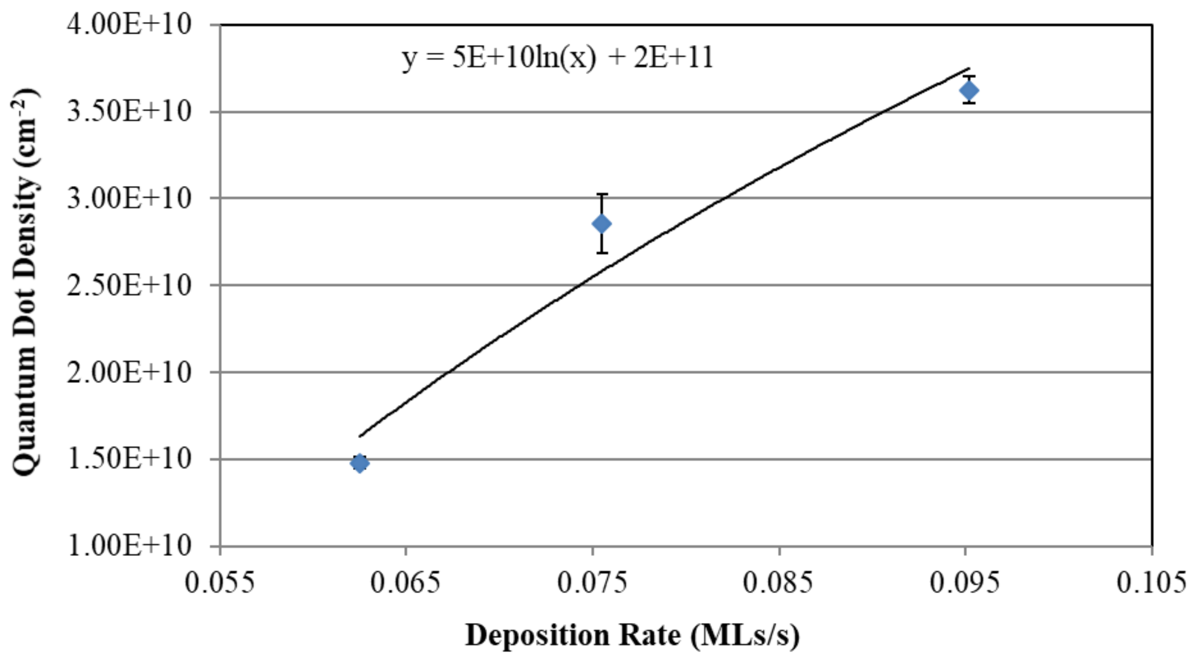

Figure 33. QD Density as a Function of Deposition Rate for Nitrogen-Rich InN QDs.

A logarithmic trend was observed for the change in quantum dot density for the Nitrogen-Rich, rate dependent series. The data series was modeled with the equation found within Figure 33. A logarithmic trend in quantum dot density was not observed in the temperature dependent or

time dependent data sets.

The underlying mechanism that caused this observed trend was the logarithmic nature of incoming source flux which changed the "pressure" of the growth surface and the surrounding system.

Looking again at Equation 23 and Equation 8,

$$N^* = n_0 \exp\left(-\frac{\Delta G}{k_b T}\right) \quad \text{(Equation 23)}$$

$$\Delta G = \alpha_3 r^3 \Delta G_v + \alpha_1 r^2 \gamma_{vf} + \alpha_2 r^2 \gamma_{fs} - \alpha_2 r^2 \gamma_{sv} \quad \text{(Equation 8)}$$

one can see the important role which ΔG plays in the nucleation density during heterogeneous nucleation. However, until now, the role of ΔG_v has not been discussed. ΔG_v is the change in free energy per unit volume and can be expressed as:

$$\Delta G_V = -\frac{k_B T}{\Omega} \ln\left(\frac{\dot{R}}{\dot{R}_c}\right) \quad \text{(Equation 14)}$$

where Ω is the atomic volume, $\dot{R}$ and $\dot{R}_C$ are the impingement flux and desorption flux of metal atoms, respectively. The desorption flux of metal atoms is dependent on substrate temperature. At 400 °C, the desorption flux is negligible or nonexistent. Therefore, as $\dot{R}$ increases at a constant substrate growth temperature, ΔG_v becomes more negative. This is an important concept with regards to QD nucleation density. If ΔG_v becomes more negative, then ΔG^* also becomes more negative. Remember, that ΔG^* refers to the maximum free energy required to form a QD with a

critical nucleation radius, $r*$. As ΔG^* becomes more negative, the barrier to nucleation is reduced, and the nucleation density increases.

Quantum Dot Height and Diameter

Table 10 and Table 11 display the quantitative results of the deposition rate treatment for the Nitrogen-Rich growth mode for InN QDs as it pertains to height and diameter, respectively.

Table 10. Nitrogen-Rich InN QD Height as a Function of Deposition Rate.

Sample ID	Growth Rate (MLs/s)	Mean Height (nm)	Standard Deviation (nm)	Error (nm)
NH94	0.0625	3.58	0.13	± 0.06
NH85	0.0755	2.97	0.09	± 0.04
NH93	0.0952	2.45	0.17	± 0.07

Table 11. Nitrogen-Rich InN QD Diameter as a Function of Deposition Rate.

Sample ID	Growth Rate (MLs/s)	Mean Diameter (nm)	Standard Deviation (nm)	Error (nm)
NH94	0.0625	51.2	4.0	± 1.73
NH85	0.0755	39.3	1.5	± 0.65
NH93	0.0952	36.5	2.5	± 1.08

Figure 34 and Figure 35 graphically display the quantitative results found in Tables 10 and 11.

A logarithmic trend was observed for the change in quantum dot height for the Nitrogen-Rich, rate dependent series. The equation used to model the change in quantum dot height with deposition rate can be found within Figure 34.

A logarithmic trend was modeled for the change in quantum dot diameter for the Nitrogen-Rich, rate dependent series. The equation used to model the change in quantum dot diameter

with deposition rate can be found within Figure 35.

More stable nuclei on the growth surface means that there was less material available for each nucleus. Therefore, the size of the QD decreased with an increase in growth rate. This can also be shown mathematically using the calculation of the critical nucleation radius, r*

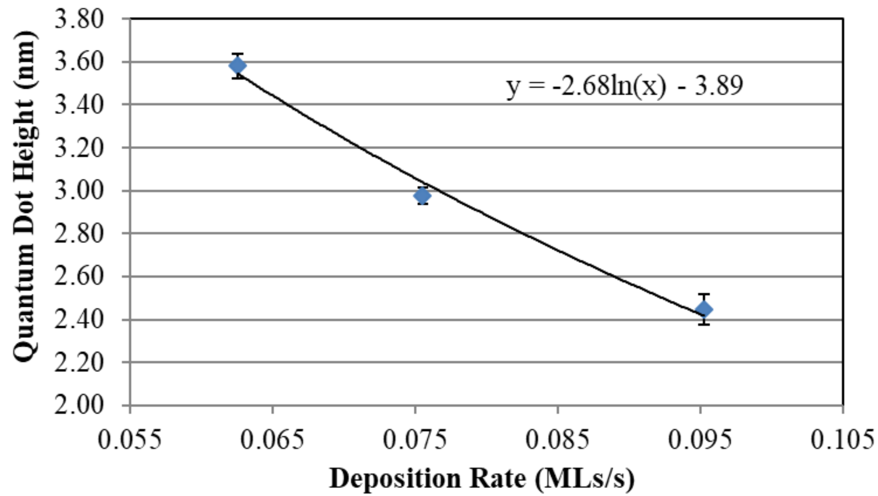

Figure 34. QD Height as a Function of Deposition Rate for Nitrogen-Rich InN QDs.

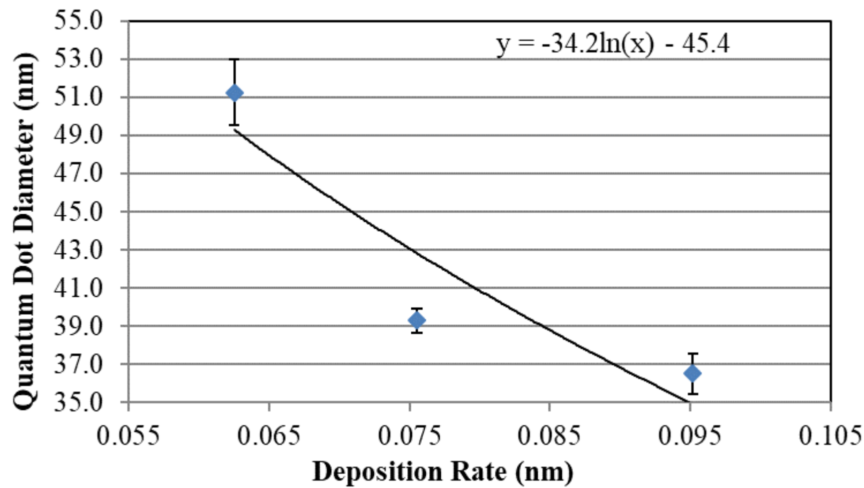

Figure 35. QD Diameter as a Function of Deposition Rate for Nitrogen-Rich InN QDs.

$$r^* = \frac{-2(a_1\gamma_{fv} + a_2\gamma_{fs} - a_2\gamma_{sv})}{3a_3\Delta G_V} \qquad \text{(Equation 15)}$$

When ΔG_v becomes more negative due to the increase in impinging flux, the critical radius decreases by $1/\Delta G_v$ or $1/\ln(\dot{R})$ where $\dot{R}$ is the impingement flux.

Volume of Deposited Material

Calculations were made to account for all deposited material observed through AFM. Volume calculations were made using the product of the average values for quantum dot density, surface area, and height. The volumes are reported as the volume of indium nitride material found in a 1 μm^2 area ($nm^3/\mu m^2$). Figure 36 graphically depicts the change in deposited material with a change in deposition rate for Nitrogen-Rich samples.

Volume was unchanged for this series. This was due to the fact that these samples were deposited with 4 MLs of InN. Four MLs of InN corresponds to 1.14×10^6 nm^3 of deposited InN volume in a 1 μm^2 area.

Quantum Dot Contact Angle

Quantum dot contact angle was measured using the Bruker Nanoscope Analysis software. Contact angles were measured and averaged for each sample in the series. Figure 37 displays the change in contact angle as a function of deposition rate for the Nitrogen-Rich series.

A slight decrease or no change in contact angle was observed for the Nitrogen-Rich, rate dependent series.

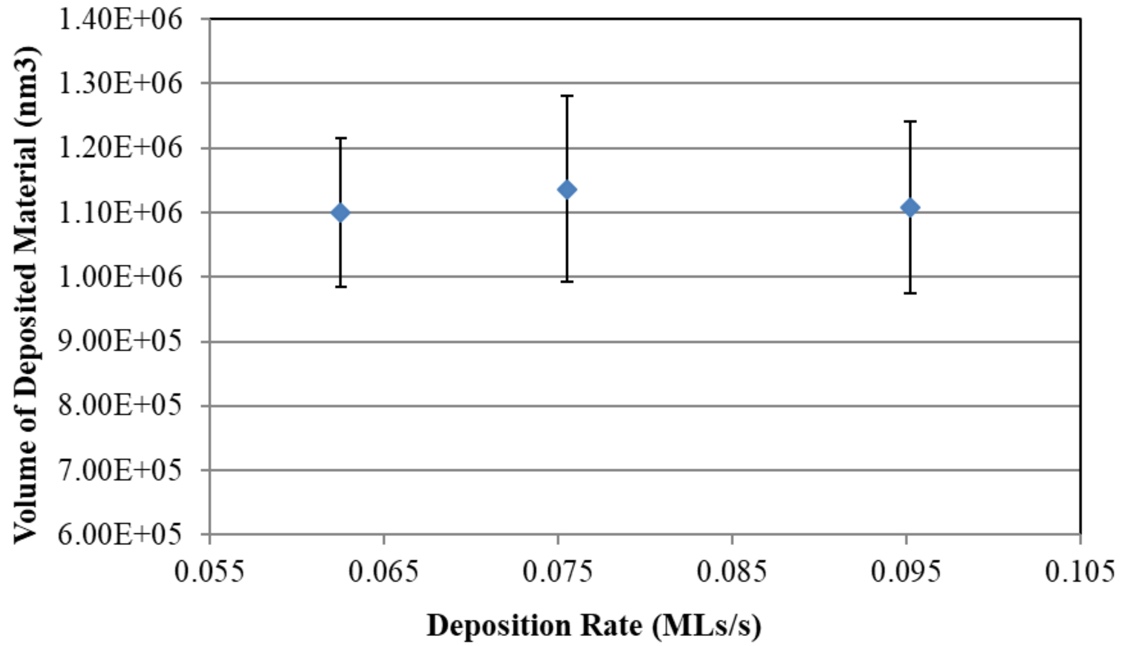

Figure 36. Volume of Deposited InN as a Function of Deposition Rate for Nitrogen-Rich InN QDs.

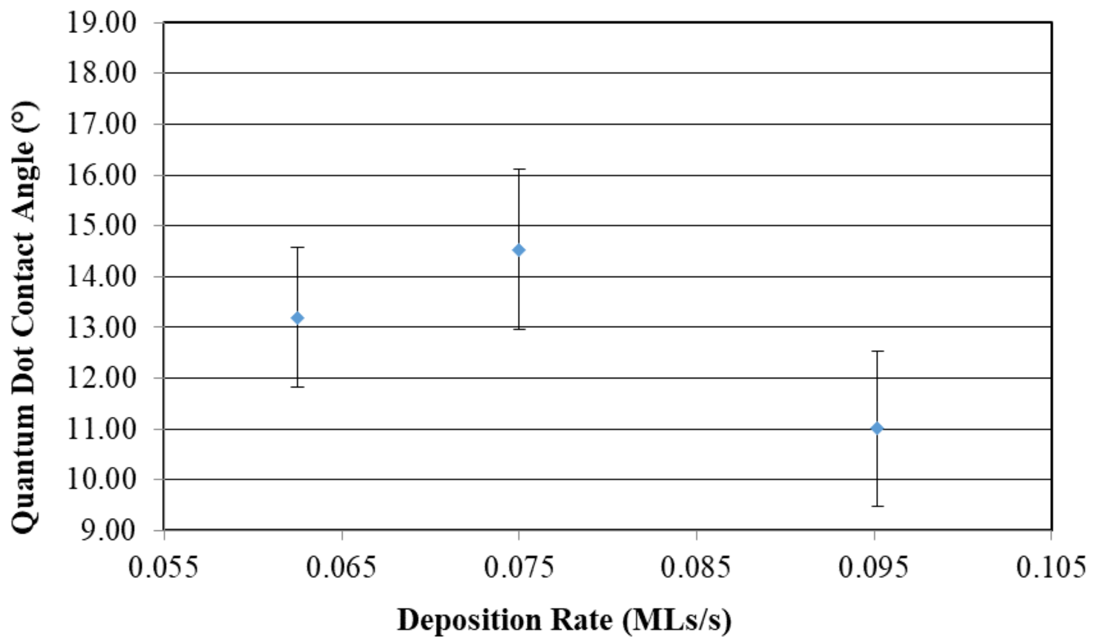

Figure 37. QD Contact Angle as a Function Deposition Rate for Nitrogen-Rich InN QDs.

4.2 Metal-Rich Growth

4.2.1 Growth Temperature Dependence

Five samples were created in order to observe the role which substrate growth temperature has on the nucleation and growth of InN QDs under Metal-Rich growth conditions. The five samples were grown at 390, 395, 400, 405, and 410 °C. Other growth conditions, deposition time (12s) and In:N deposition flux ratio (1.07) were held constant during this experiment. Each sample was grown to have the equivalent of 3 MLs of indium nitride deposited. The results from the AFM characterization can be seen in Figure 38.

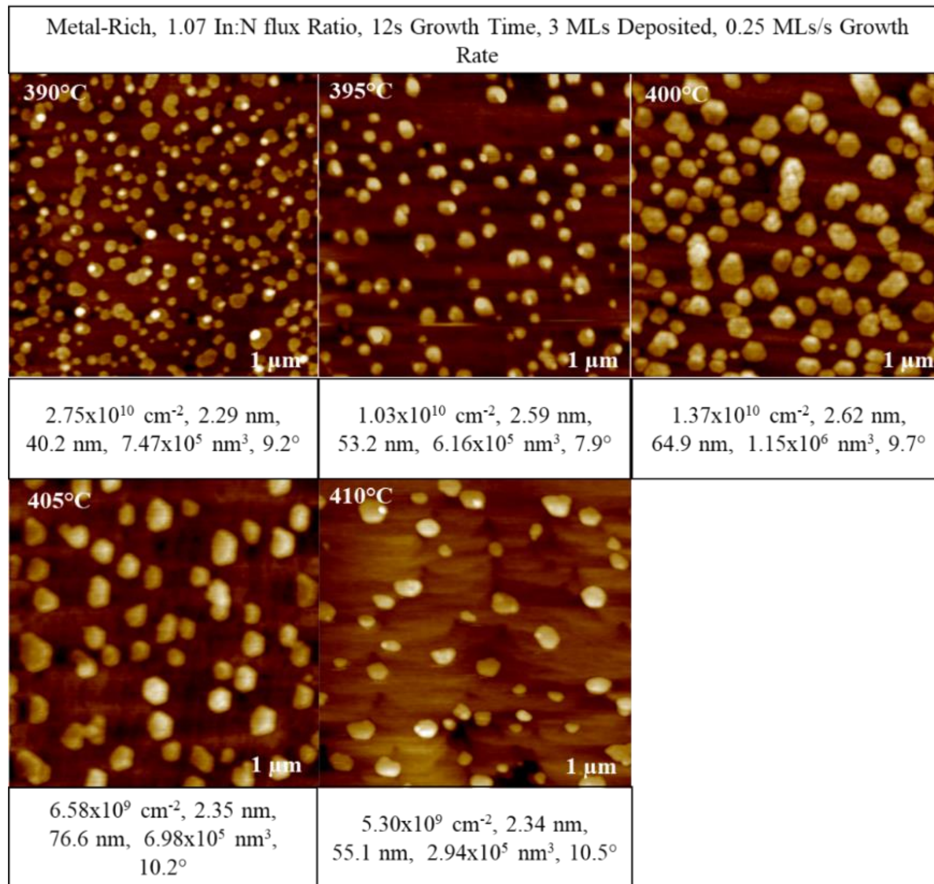

Figure 38. AFM scans of Metal-Rich, Temperature Dependent samples. (Each scan's deposition time, deposition thickness, and scan size are indicated within the scan. Descriptive statistics are given in each box for the following in this order: QD mean density, height, and diameter, total volume deposited, and mean contact angle of QD with the growth surface.)

Quantum Dot Density

Table 12 displays the quantitative results of the substrate growth temperature treatment for the Metal-Rich growth mode for InN QDs as it pertains to QD density.

Table 12. Metal-Rich InN QD Density as a Function of Growth Temperature.

Sample ID	Substrate Temperature (°C)	1/kT (J^{-1})	Mean Density (cm^{-2})	Standard Deviation (cm^{-2})	Error (cm^{-2})
NH103	390	1.093E+20	2.75E+10	3.19E+09	± 1.37E+09
NH105	395	1.085E+20	1.03E+10	1.54E+09	± 1.22E+09
NH101	400	1.076E+20	1.37E+10	2.32E+09	± 9.94E+08
NH104	405	1.069E+20	6.58E+09	7.55E+08	± 3.23E+08
NH102	410	1.061E+20	5.30E+09	8.02E+08	± 4.45E+08

Figure 39 is a plot of quantum dot density as a function of the inverse of energy as measured by the product of the Boltzmann constant, k, and the absolute substrate temperature, T. Error bars are not visible in Figure 39 and are represented within the data point.

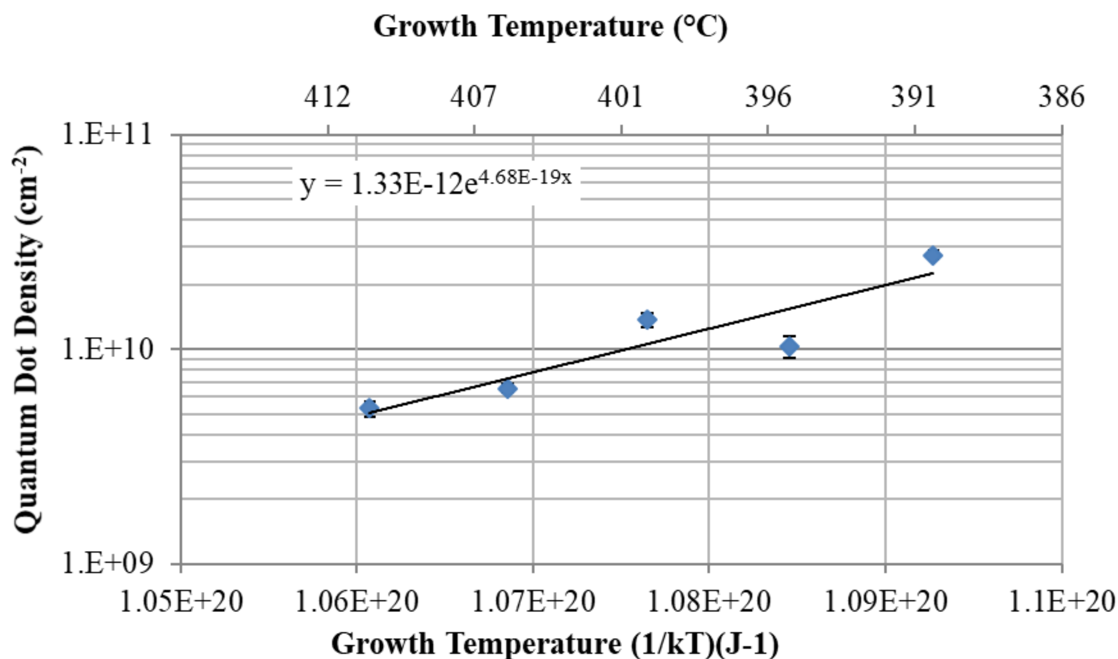

Figure 39. QD Density as a Function of 1/kT for Metal-Rich InN QDs.

The data set shown in Figure 39 has an exponential tread which has been fitted by the equation displayed. The activation energy of this system was found to be 4.68x10^{-19} J, or 2.93 eV. The observed trend found in the density as a function of time is consistent with heterogeneous nucleation and follows Equation 24.

$$N^* = n_0 \exp\left(\frac{-\Delta G^*}{k_B T}\right) \qquad \text{(Equation 24)}$$

Quantum Dot Height and Diameter

Table 13 and Table 14 display the quantitative results of the substrate growth temperature parameter for the Metal-Rich growth environment for InN QDs as it pertains to height and diameter, respectively.

Table 13. Metal-Rich InN QD Height as a Function of Growth Temperature.

Sample ID	Substrate Temperature (°C)	1/kT (J^{-1})	Mean Height (nm)	Standard Deviation (nm)	Error (nm)
NH103	390	1.093E+20	2.29	0.22	± 0.09
NH105	395	1.085E+20	2.59	0.12	± 0.10
NH101	400	1.076E+20	2.62	0.15	± 0.06
NH104	405	1.069E+20	2.35	0.19	± 0.08
NH102	410	1.061E+20	2.34	0.08	± 0.05

Table 14. Metal-Rich InN QD Diameter as a Function of Growth Temperature.

Sample ID	Substrate Temperature (°C)	1/kT (J^{-1})	Mean Diameter (nm)	Standard Deviation (nm)	Error (nm)
NH103	390	1.093E+20	40.2	5.8	± 2.49
NH105	395	1.085E+20	53.2	6.0	± 4.74
NH101	400	1.076E+20	64.9	4.9	± 2.08
NH104	405	1.069E+20	76.6	4.5	± 1.93
NH102	410	1.061E+20	55.1	5.7	± 3.17

Figure 40 and Figure 41graphically display the data found in Table 13 and Table 14.

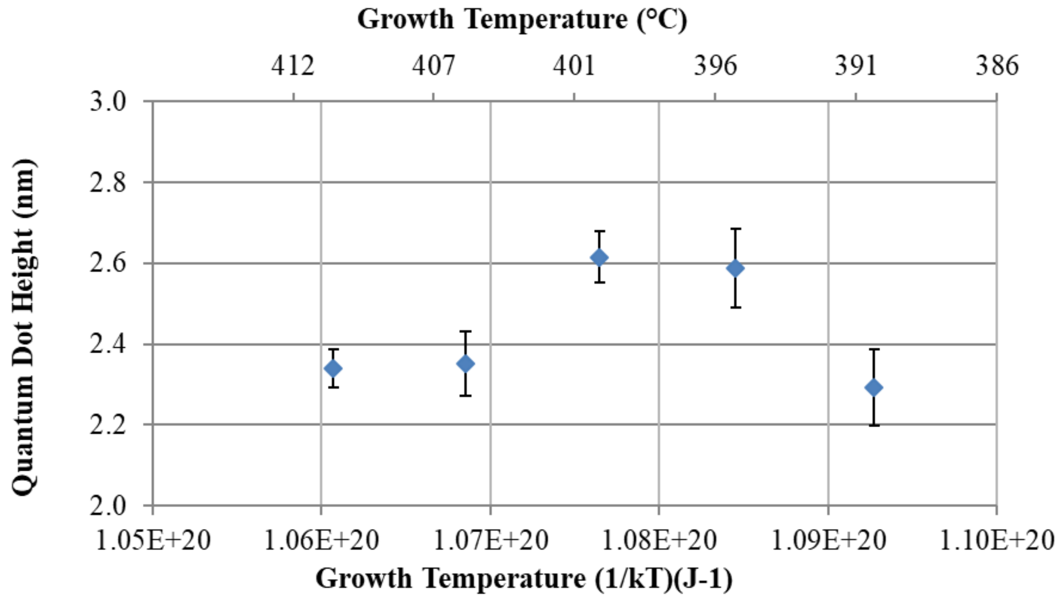

Figure 40. QD Height as a Function of 1/kT for Metal-Rich InN QDs.

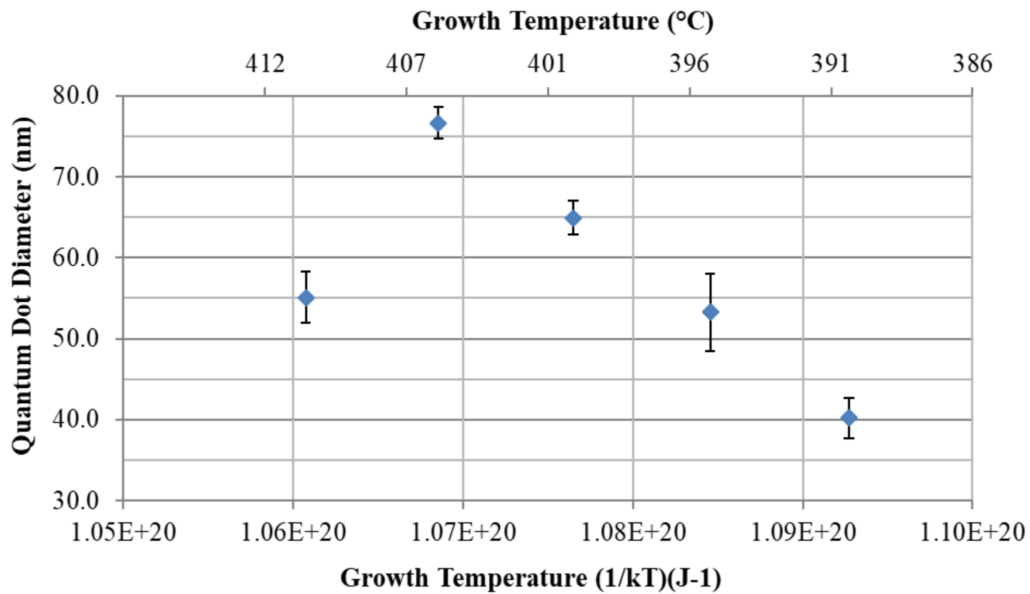

Figure 41. QD Diameter as a Function of 1/kT for Metal-Rich InN QDs.

No conclusive data fit could be displayed for either Figure 40 or Figure 41. The QD height showed little or no change. QD heights in this series ranged from 2.3 nm to 2.6 nm. Those heights corresponded to between 8 and 9 monolayers, or 2.28 and 2.57 nm, respectively. The change in diameter shows typical growth and ripening effects for SK QDs. An increasing trend was observed with increasing temperature for QD diameter until the hottest growth temperature of 410°C is reached. The reduction in diameter at 410°C was most likely caused by dissociation of InN as seen in the Nitrogen-Rich, temperature dependent series.

The difference in growth rates for QD heights and diameters with increasing temperatures suggested that the Metal-Rich QDs have a preference for lateral growth.

Volume of Deposited Material

Calculations were made to account for all deposited material observed through AFM. Volume calculations were made using the product of the average values for quantum dot density, surface area, and height. The volumes are reported as the volume of indium nitride material found in a 1 μm^2 area ($nm^3/\mu m^2$). Figure 42 graphically depicts the change in deposited material with a change in growth temperature for the Metal-Rich samples.

No discernable trend was observed in the volume of material deposited. At 3 MLs, the expected volume for a 1 μm^2 area was $8.85 x 10^5$ nm^3. Dissociation of InN at temperatures greater than 400 °C was likely the cause for the observed reduction in calculated volume.

Quantum Dot Contact Angle

Quantum dot contact angle was measured using the Bruker Nanoscope Analysis software. Contact angles were averaged for each sample in the series. Figure 43 displays the change in contact angle as a function of growth substrate temperature.

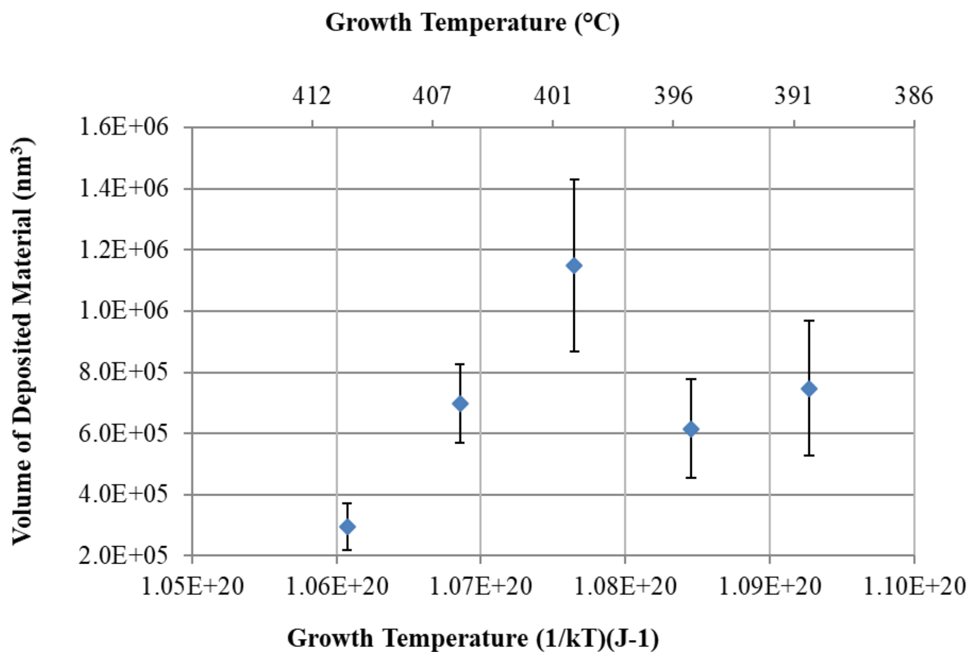

Figure 42. Deposited InN Volume as a Function of 1/kT for Metal-Rich InN QDs.

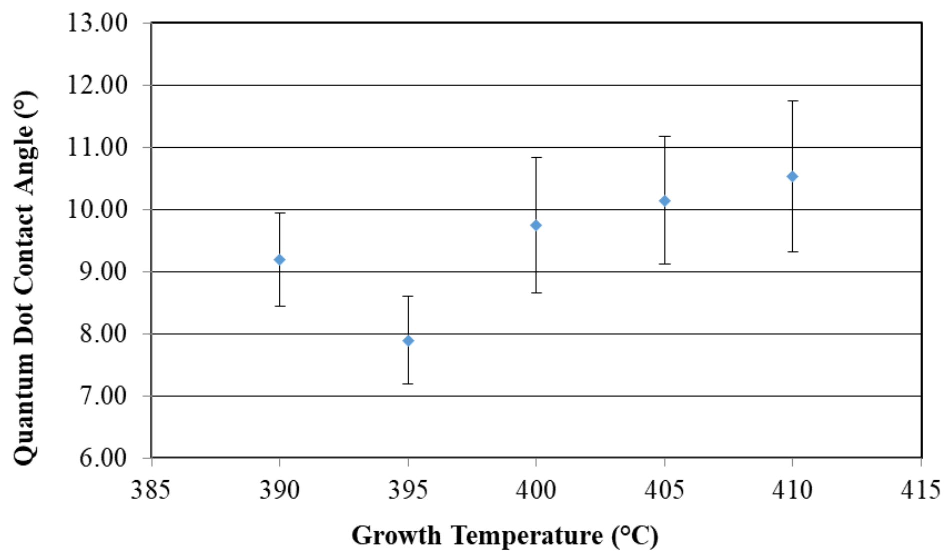

Figure 43. QD Contact Angle as a Function of Growth Temperature for Metal-Rich InN QDs.

No significant change was found in quantum dot contact angle with increasing growth temperature. Metal-Rich QDs showed a shallow average contact angle of approximately 10°.

4.2.2 Deposition Time Dependence

Three samples were created in order to observe the role in which deposition time has on the nucleation and growth of InN QDs for a Metal-Rich growth environment. The three samples were fabricated at deposition times of 12, 20, and 28 seconds. The deposition times led to film depositions of 3, 5, and 7 MLs, respectively. Other growth conditions, growth temperature (400°C), In:N flux ratio (1.07), and growth rate (0.25 MLs/s), were held constant during this experiment. The results from the AFM characterization are shown in Figure 44.

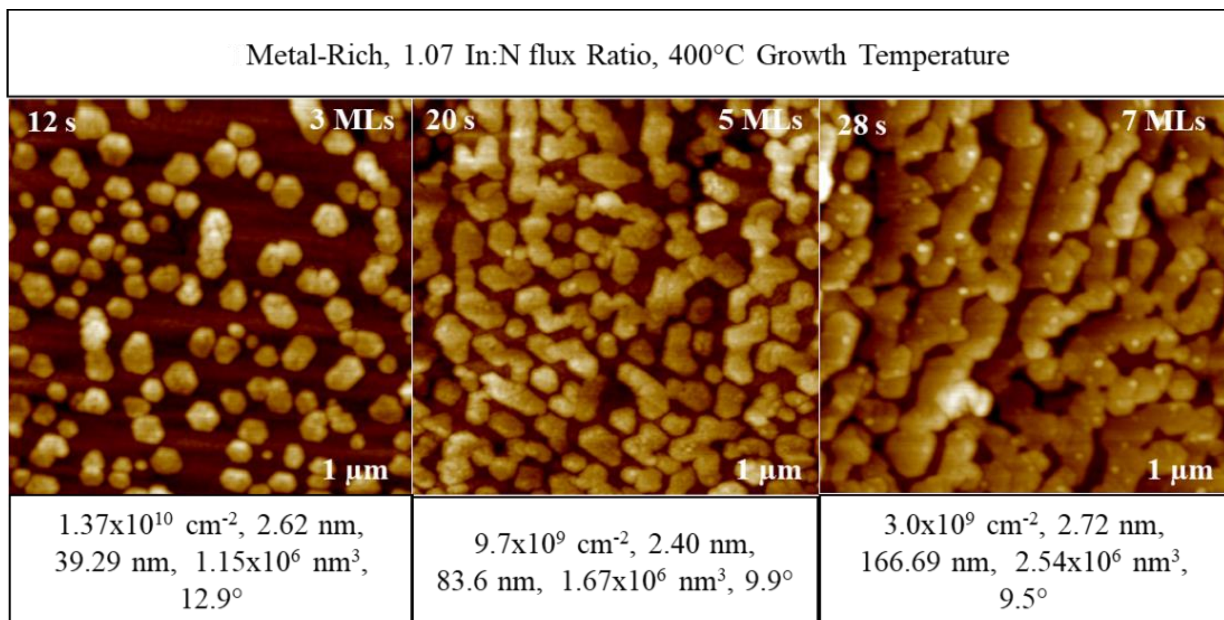

Figure 44. AFM scans of Metal-Rich, Time Dependent samples. (Each scan's deposition time, deposition thickness, and scan size are indicated within the scan. Descriptive statistics are given in each box for the following in this order: QD mean density, height, and diameter, total volume deposited, and mean contact angle of QD with the growth surface.)

Quantum Dot Density

Table 15 displays the quantitative results of the deposition time treatment for the Metal-Rich growth mode for InN QDs as it pertains to QD density. Figure 45 is a plot of QD density as a function of deposition time. Error bars represent a 95% confidence interval.

Table 15. Metal-Rich InN QD Density as a Function of Deposition Time.

Sample ID	Deposition Time (s)	Mean Density (nm)	Standard Deviation (nm)	Error (nm)
NH101	12	1.37E+10	2.32E+09	± 9.94E+08
NH108	20	9.70E+09	1.01E+09	± 2.60E+09
NH109	28	3.00E+09	6.00E+08	± 1.54E+09

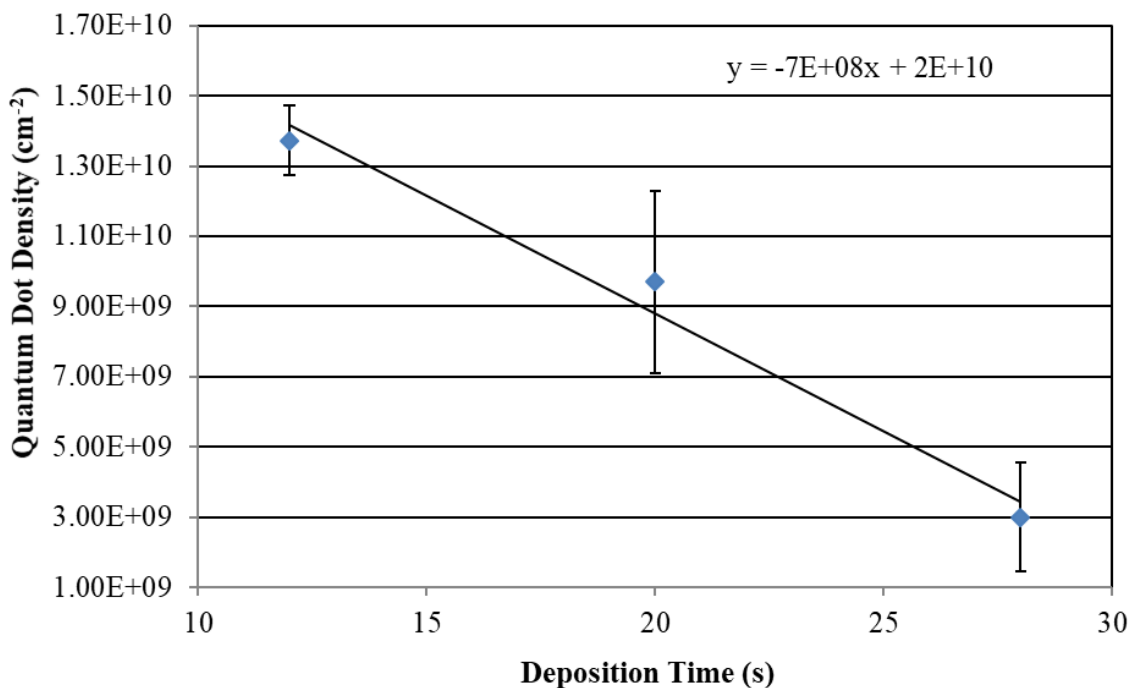

Figure 45. QD Density as a Function of Deposition Time for Metal-Rich InN QDs.

A decreasing linear trend was observed in the quantum dot density as a function of deposition time. The QD density decreases at a rate of 7x10^8 cm^{-2} s^{-1}. This trend was due to the

coalescent nature of the quantum dot growth and ripening.

Quantum Dot Height and Diameter

The height of structures was analyzed and the quantitative results can be found in Table 16. The average height of each sample has been displayed in Figure 46.

Table 16. Metal-Rich InN QD Height as a Function of Deposition Time.

Sample ID	Deposition Time (s)	Mean Height (nm)	Standard Deviation (nm)	Error (nm)
NH101	12	2.62	0.15	± 0.06
NH108	20	2.40	0.26	± 0.11
NH109	28	2.72	0.75	± 0.60

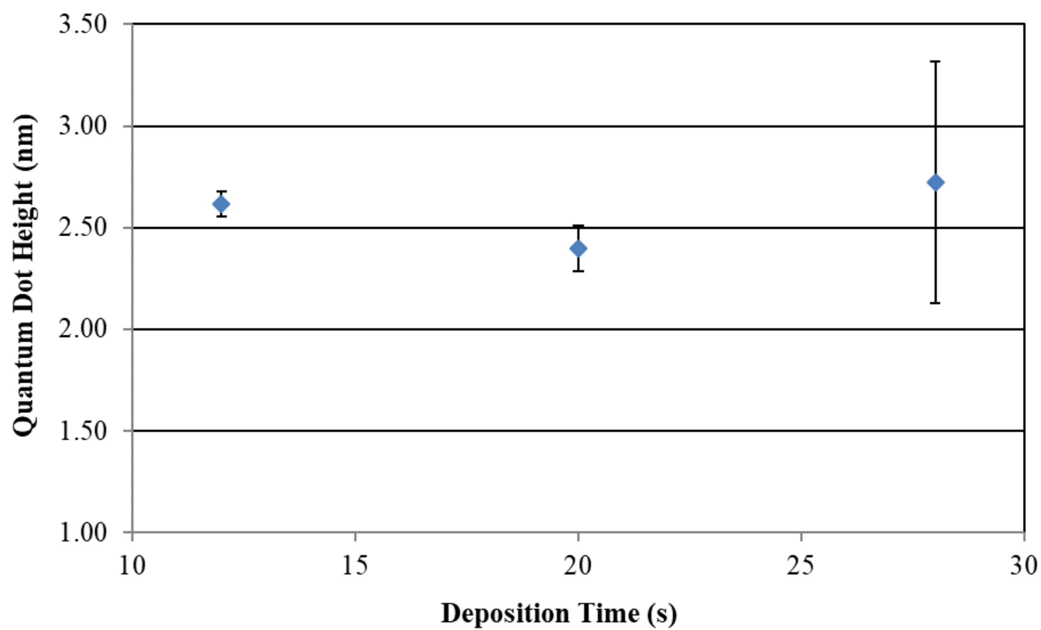

Figure 46. QD Height as a Function of Deposition Time for Metal-Rich InN QDs.

No change was observed in the quantum dot height due to extended growth time. AFM measurement error increased with the increase in coalescence of indium nitride structures.

Due to the coalescent nature of the Metal-Rich, time dependent series, quantum dot diameter was very difficult to determine. An average diameter was calculated for the samples grown for 20 and 28 seconds. The average diameter was calculated using the average surface area of a single structure. The diameter for the sample with a growth time of 12 s was measured with the Bruker Nanoscope Analysis software. The quantitative results can be found in Table 17.

Table 17. Metal-Rich InN QD Diameter as a Function of Deposition Time.

Sample ID	Deposition Time (s)	Mean Diameter (nm)	Standard Deviation (nm)	Error (nm)
NH101	12	64.94	4.86	± 2.08
NH108	20	83.63	8.40	± 38.22
NH109	28	166.69	23.84	± 45.81

The average diameter for each sample has been plotted in Figure 47. Larger error was calculated for two of the three samples due to the uncertainty in the diameter calculation.

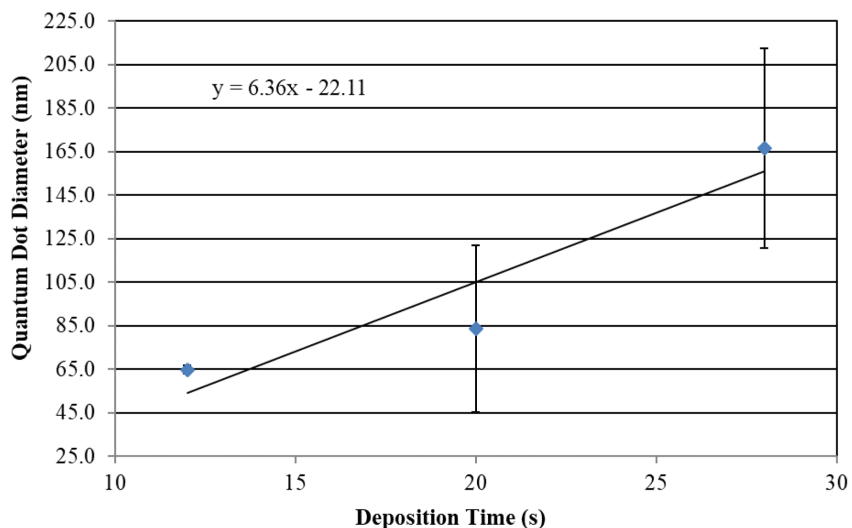

Figure 47. QD Diameter as a Function of Deposition Time for Metal-Rich InN QDs.

An increasing trend in diameter was observed for longer deposition times. Again, the diameter of Metal-Rich InN QDs increased whereas the height of the QD remained unchanged, suggesting that the Metal-Rich QDs prefer lateral growth.

Volume of Deposited Material

Calculations were made to account for all deposited material observed through AFM. Volume calculations were made using the product of the average values for quantum dot density, surface area, and height. The volumes are reported as the volume of indium nitride material found in a 1 μm^2 area ($nm^3/\mu m^2$). Figure 48 graphically depicts the change in deposited material with a change in deposition time for Metal-Rich samples.

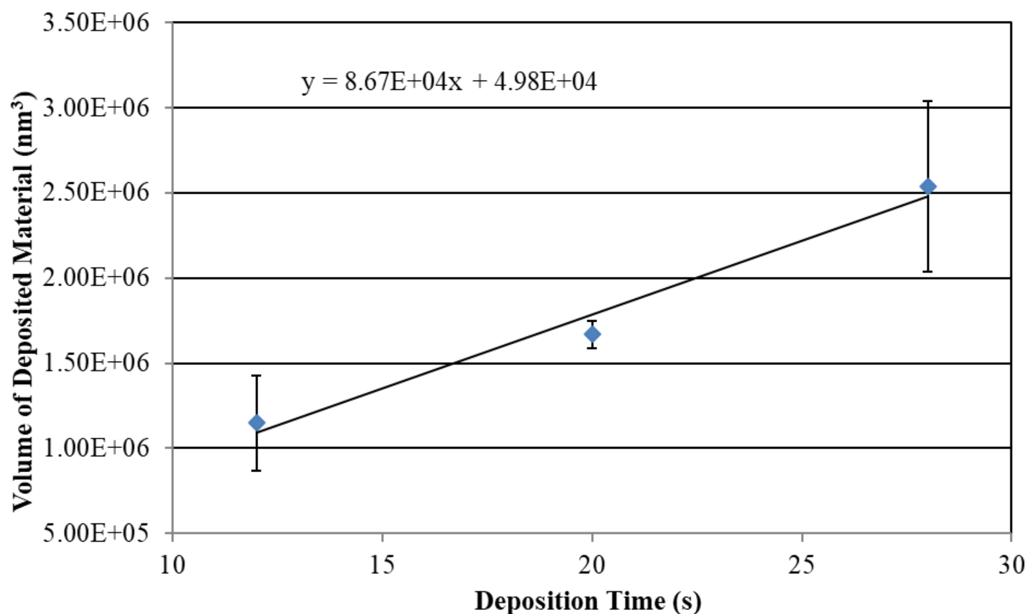

Figure 48. Deposited InN Volume as a Function of Deposition Time for Metal-Rich InN QDs.

A linear trend was observed for the volume of deposited material with increased deposition time. From the fitted equation, the volume increased at a rate of 8.67×10^4 nm^3/s. Given the c-plane lattice spacing of InN is 2.85 Å, the modeled rate of change in volume corresponded to a

growth rate of 0.30 MLs/s. This was higher than the expected growth rate used of 0.25 MLs/s. However, the measured volume would be higher due to the presence of excess indium on the growth surface due to the Metal-Rich growth condition.

Quantum Dot Contact Angle

Quantum dot contact angle was measured using the Bruker Nanoscope Analysis software. Contact angles were measured and averaged for each sample in the series. Figure 49 displays the change in contact angle as a function of deposition time for the Metal-Rich series.

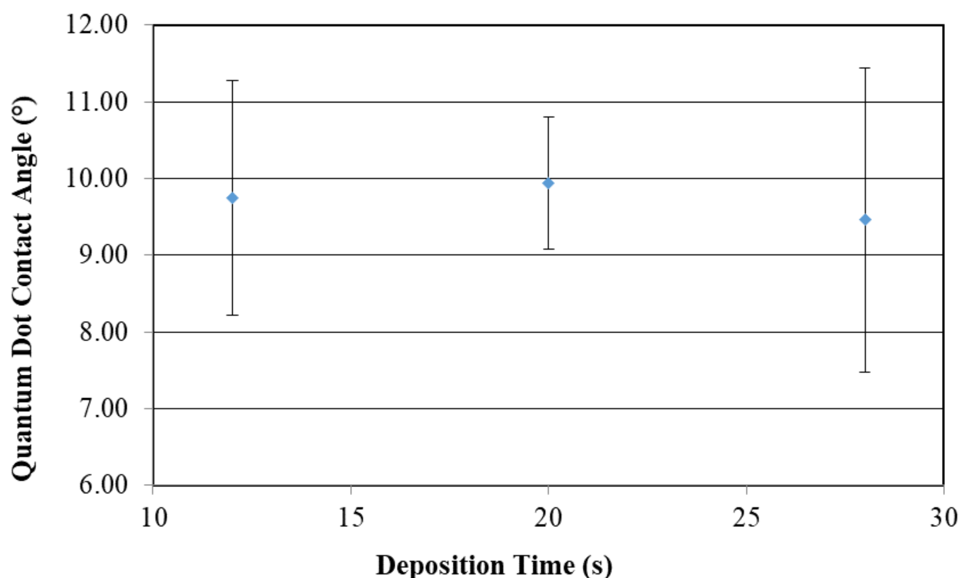

Figure 49. QD Contact Angle as a Function Deposition Time for Metal-Rich InN QDs.

There was no change in the QD contact angle for the Metal-Rich, time-dependent series. Like the temperature-dependent series, the time dependent series had an average QD contact angle of approximately 10°.

4.2.3 Deposition Rate Dependence

Three rate dependent samples were grown at growth rates of 0.24, 0.32, 0.39 MLs/s. Total deposition amounts for these three growth rates was 2.88, 3.84, and 4.68 MLs, respectively. The growth rates were varied by changing the nitrogen flow rate to the plasma source. The three nitrogen flow rates used were 0.5, 0.75, and 1.0 sccm. The power supplied to the plasma source was held constant at 350W. The growth temperature and deposition time were held constant at 400 °C and 12 seconds, respectively. The results from the AFM characterization are shown in Figure 50.

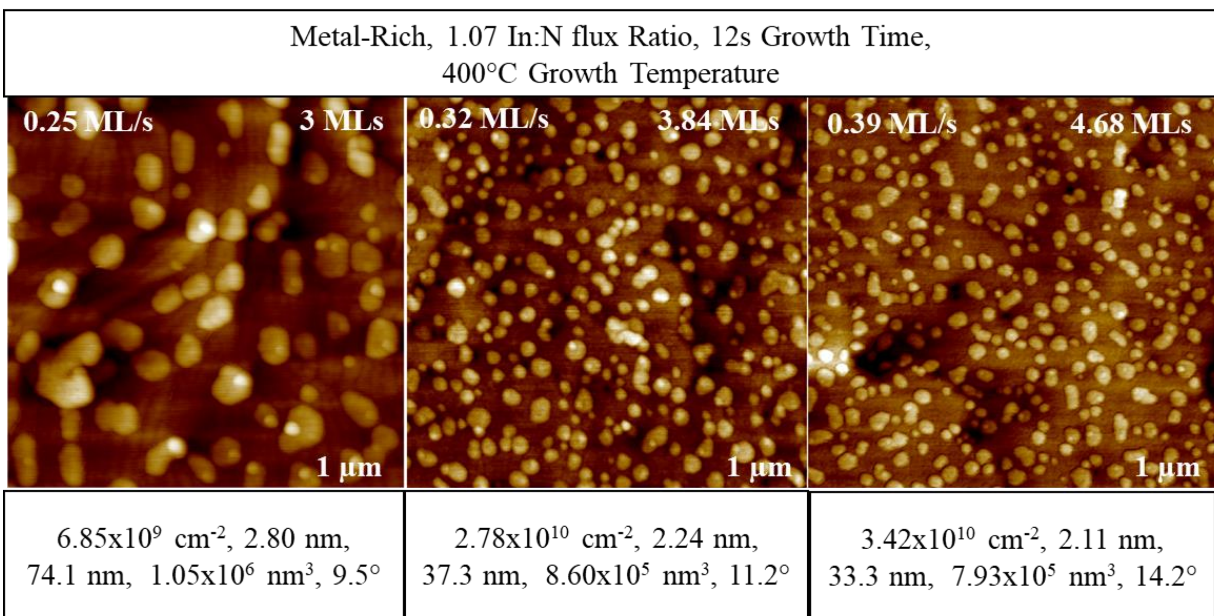

Figure 50. AFM scans of Metal-Rich, Rate Dependent samples. (Each scan's deposition time, deposition thickness, and scan size are indicated within the scan. Descriptive statistics are given in each box for the following in this order: QD mean density, height, and diameter, total volume deposited, and mean contact angle of QD with the growth surface.)

Quantum Dot Density

Table 18 displays the quantitative results of the substrate growth temperature treatment

for the Nitrogen-Rich growth mode for InN QDs as it pertains to QD density.

Table 18. Metal-Rich InN QD Density as a Function of Deposition Rate.

Sample ID	Growth Rate (MLs/s)	Mean Density (cm^{-2})	Standard Deviation (cm^{-2})	Error (cm^{-2})
NJ37	0.25	6.85E+09	5.39E+08	± 2.31E+08
NJ38	0.32	2.78E+10	2.92E+09	± 1.25E+09
NJ39	0.39	3.42E+10	1.91E+09	± 1.52E+09

Figure 51, shown below, is a plot of quantum dot density as a function of the deposition rate. Where error bars are not visible in Figure 51, they are represented within the data point.

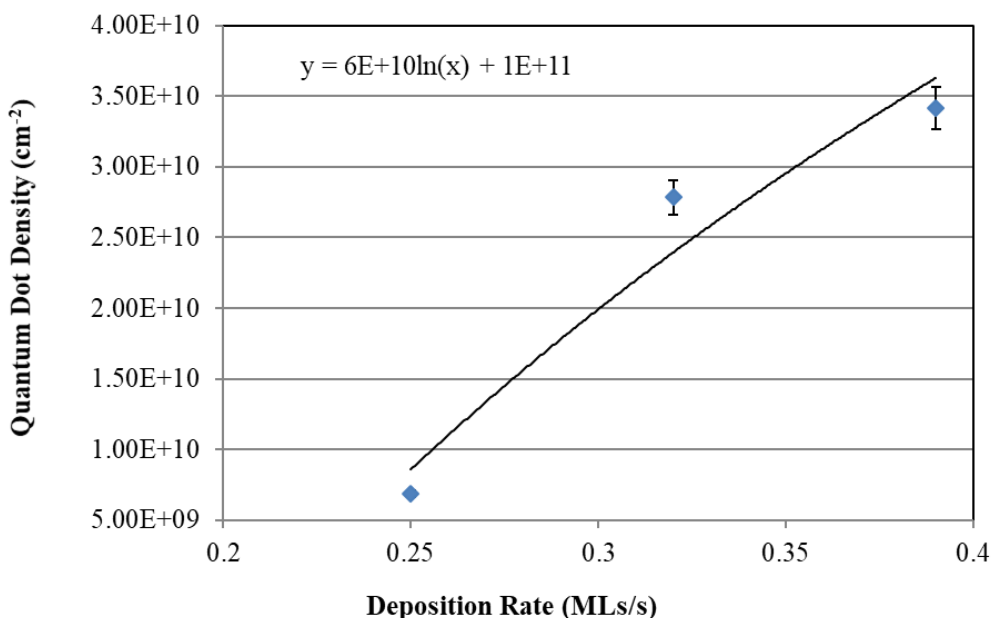

Figure 51. QD Density as a Function of Deposition Rate for Metal-Rich InN QDs.

A logarithmic trend was observed for the change in quantum dot density for the Metal-Rich, rate dependent series. The data series was modeled with the equation found within Figure 51. A logarithmic trend in quantum dot density was not observed in the temperature dependent or

time dependent data sets. Discussion of this logarithmic trend was discussed in the Nitrogen-Rich, growth rate dependent results (Section 4.1.3).

Quantum Dot Height and Diameter

The quantitative results of the AFM analysis on structure size can be found in Table 19 and Table 20. These results have been graphically displayed in Figure 52 and Figure 53.

A logarithmic trend was observed for the change in quantum dot height for the Metal-Rich, rate dependent series. The equation used to model the change in quantum dot height with deposition rate can be found within Figure 52. The logarithmic trend in QD height was previously discussed (Section 4.1.3.1).

Table 19. Metal-Rich InN QD Height as a Function of Deposition Rate.

Sample ID	Growth Rate (MLs/s)	Mean Height (nm)	Standard Deviation (nm)	Error (nm)
NH94	0.25	2.92	0.23	± 0.10
NH85	0.32	2.24	0.17	± 0.07
NH93	0.39	2.11	0.14	± 0.11

Table 20. Metal-Rich InN QD Diameter as a Function of Deposition Rate.

Sample ID	Growth Rate (MLs/s)	Mean Diameter (nm)	Standard Deviation (nm)	Error (nm)
NH94	0.25	73.4	2.10	± 0.90
NH85	0.32	36.9	2.90	± 1.24
NH93	0.39	33.3	3.22	± 2.56

A logarithmic trend was observed for the change in quantum dot diameter for the Metal-Rich, rate dependent series. The equation used to model the change in quantum dot diameter with deposition rate can be found within Figure 53. The logarithmic trend in QD diameter was previously discussed (Section 4.1.3).

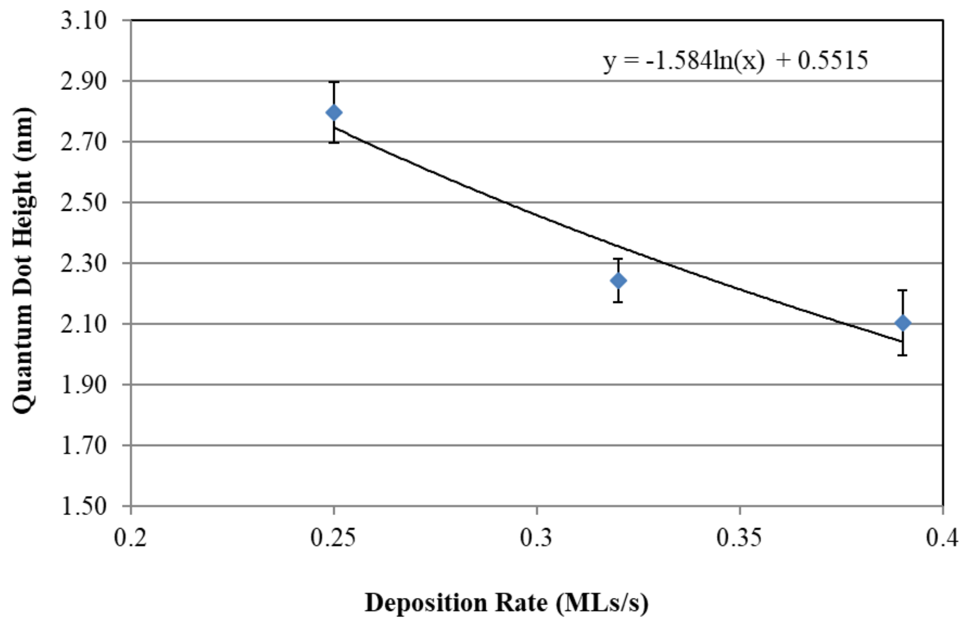

Figure 52. QD Height as a Function of Deposition Rate for Metal-Rich InN QDs.

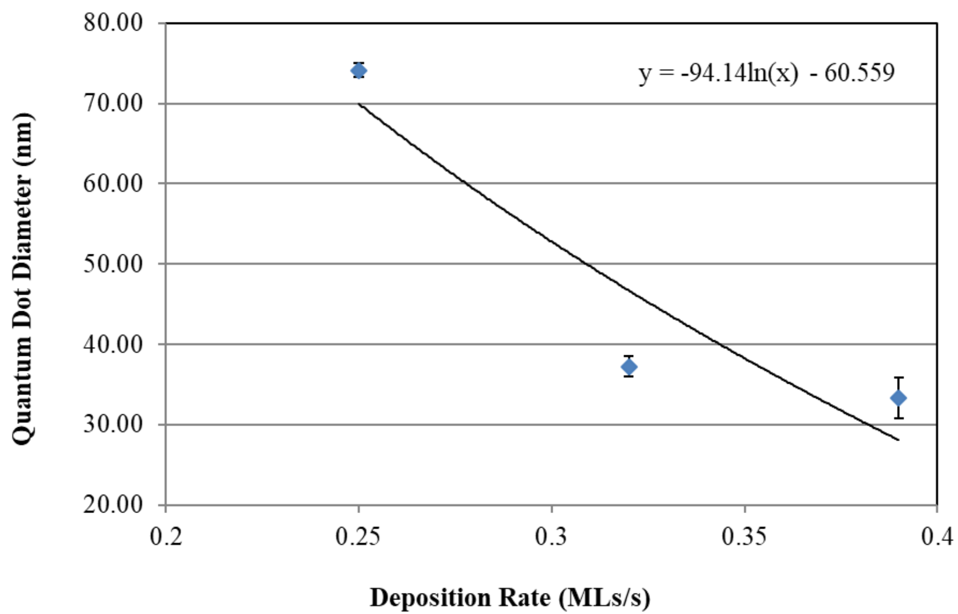

Figure 53. QD Diameter as a Function of Deposition Rate for Metal-Rich InN QDs.

Volume of Deposited Material

Calculations were made to account for all deposited material observed through AFM. Volume calculations were made using the product of the average values for quantum dot density, surface area, and height. The volumes are reported as the volume of indium nitride material found in a 1 μm^2 area ($nm^3/\mu m^2$). Figure 54 graphically depicts the change in deposited material with a change in deposition rate for Metal-Rich samples.

A decreasing, logarithmic trend was observed for the volume of material as the deposition rate was increased. This was an unusual outcome. The expected outcome for this series would be an increase in volume with increasing deposition rate. The observed trend in Figure 54 suggests that the deposition rate actually went down.

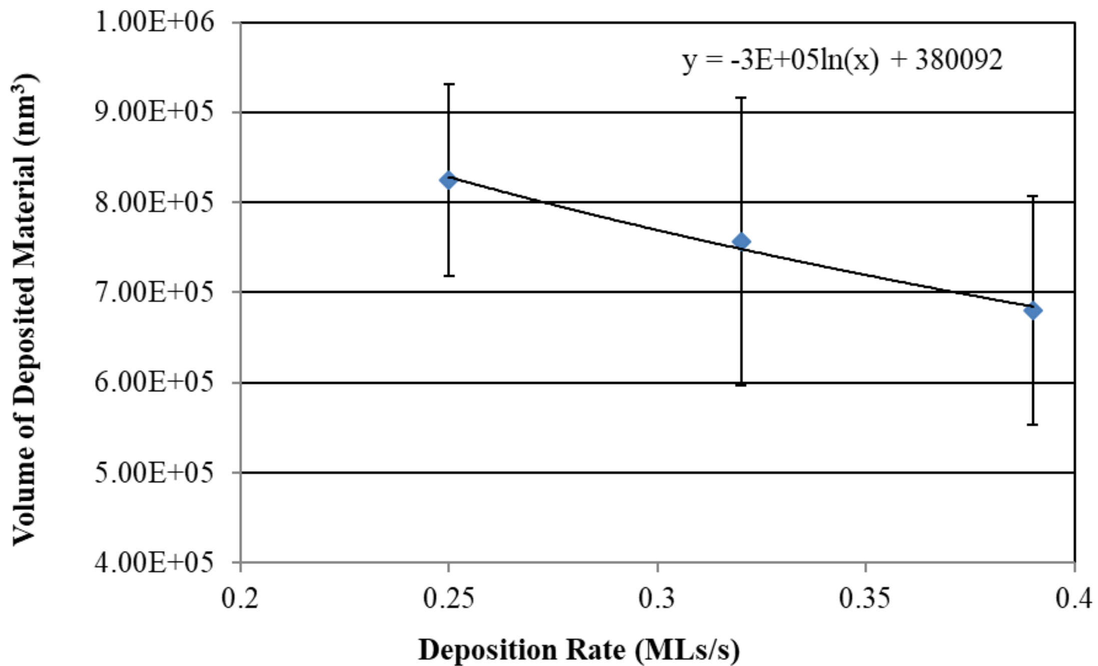

Figure 54. Deposited InN Volume as a Function of Deposition Rate for Metal-Rich InN QDs.

Quantum Dot Contact Angle

Quantum dot contact angle was measured using the Bruker Nanoscope Analysis software. Contact angles were measured and averaged for each sample in the series. Figure 55 displays the change in contact angle as a function of deposition rate for the Metal-Rich series.

An increase in contact angle with increasing deposition rate was observed. The average magnitude of the QD contact angle was approximately 11°.

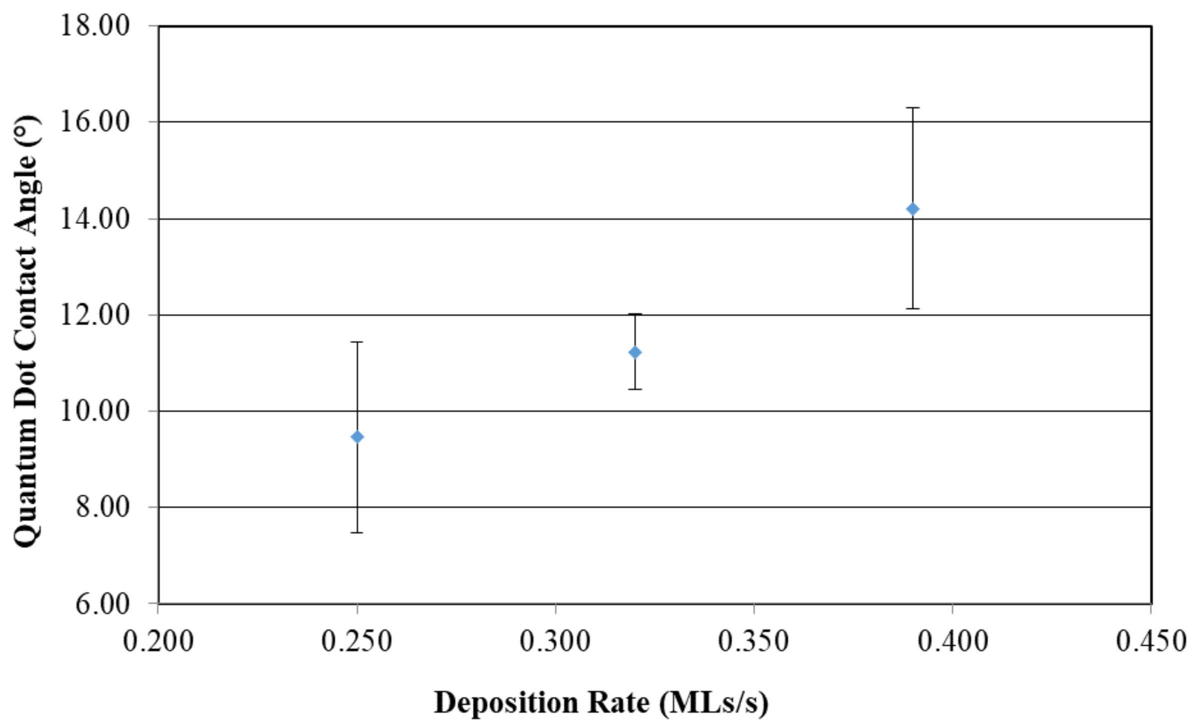

Figure 55. QD Contact Angle as a Function Deposition Rate for Metal-Rich InN QDs.

4.3 Comparison of Nitrogen-Rich and Metal-Rich Growth Environments

4.3.1 Nitrogen-Rich

The Nitrogen-Rich InN QDs followed typical SK QD growth behavior. Through RHEED observations, a 2D-3D transition was observed. This critical thickness was found to be

approximately 2.2-2.5 MLs. Control of QD properties (density, height, diameter, volume, and contact angle) by growth parameters (growth temperature, deposition time, and deposition rate) were explained with heterogeneous nucleation theory in the previous sections dedicated to manipulation of each growth parameter.

4.3.2 Metal-Rich

The Metal-Rich InN QDs followed typical SK QD growth behavior. Through RHEED observations, a 2D-3D transition was observed. This critical thickness was found to be approximately 3 MLs. The difference in critical thickness from the Nitrogen-Rich samples was due to the increased growth rate of the Metal-Rich samples. The density of time dependent QDs decreased with increasing deposition time due to the coalescence of InN QDs. The QD heights were observed to be constant and "self-limiting." Diameters increased with growth temperature and deposition time. The difference in height and diameter growth rates suggested that the Metal-Rich QDs prefer lateral growth over vertical growth. The deposition rate dependent volume decreased with increasing deposition rate. The average contact angle was reduced (10°) in comparison to the Nitrogen-Rich average contact angle (15°).

4.3.3 InN QD shape

Figures 56, 57, and 58 are typical representations of the shapes found for both Nitrogen-Rich and Metal-Rich InN QDs.

Metal-Rich QD shape differed significantly to that of the Nitrogen-Rich QD shape. The Metal-Rich QDs exhibited a "flat top" shape, whereas the Nitrogen-Rich QDs had smooth, curved surfaces.

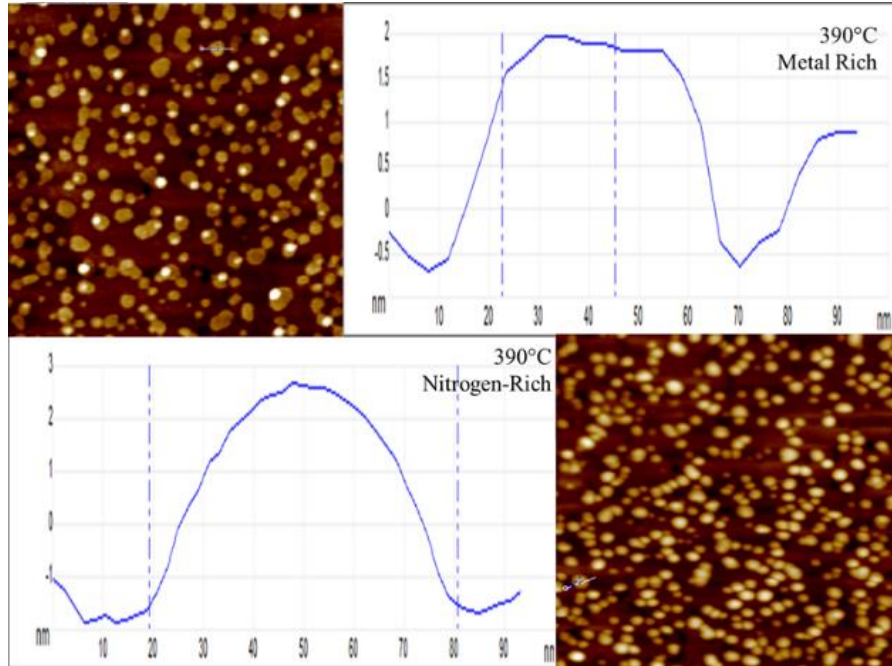

Figure 56. InN Shape Comparison for Metal-Rich and Nitrogen-Rich Growth Conditions at 390 °C.

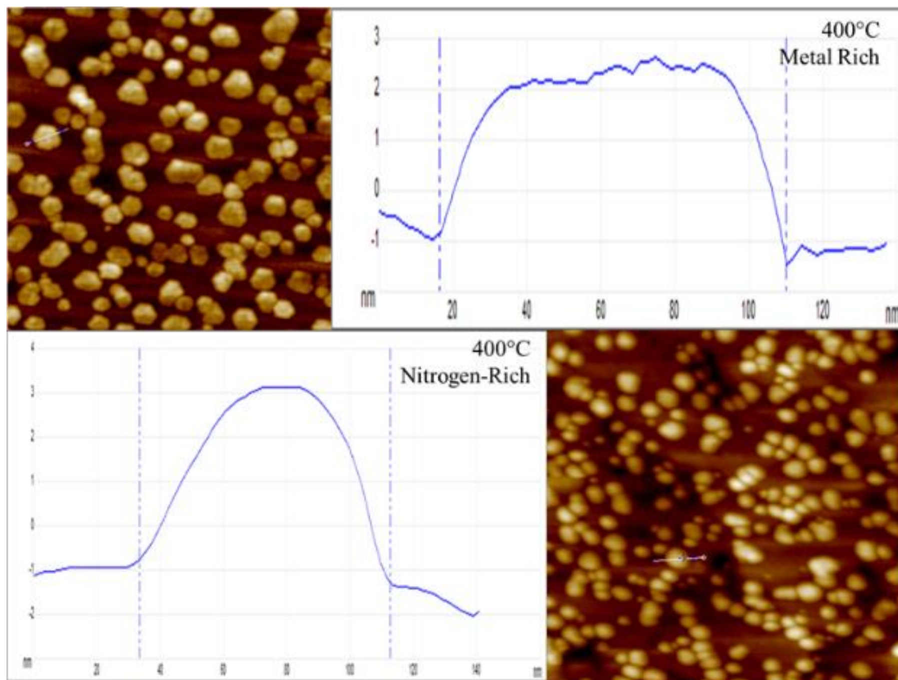

Figure 57. InN Shape Comparison for Metal-Rich and Nitrogen-Rich Growth Conditions at 400 °C.

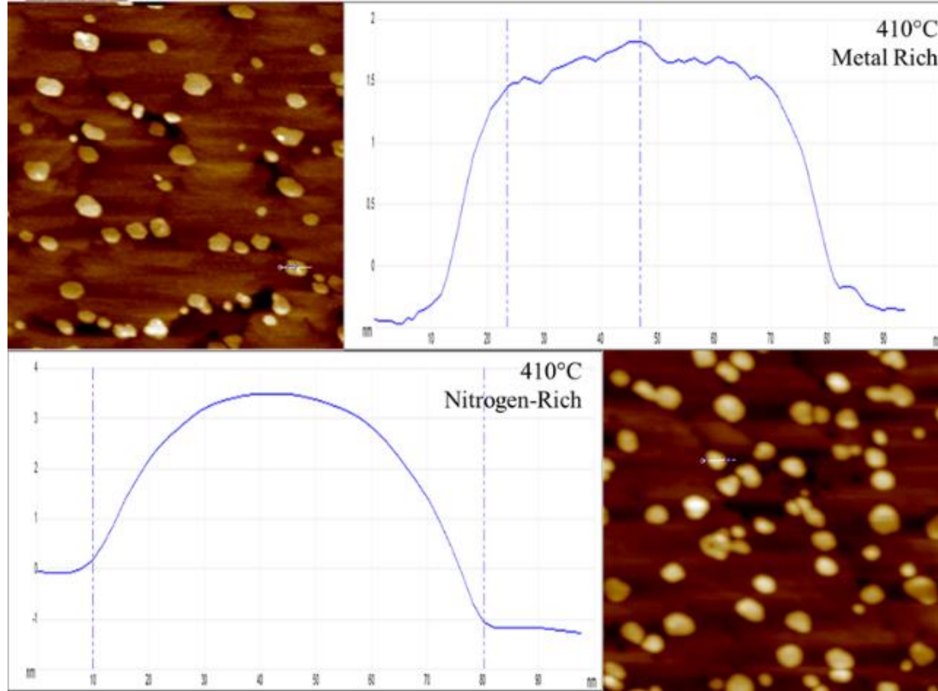

Figure 58. InN Shape Comparison for Metal-Rich and Nitrogen-Rich Growth Conditions at 410 °C.

4.4 The Presence of Excess Indium

Observations of the analyzed AFM scans indicated that there was a significant difference in the QDs produced by the two different growth environments. It was hypothesized that the differences discussed in Section 4.3 were due to the excess indium on the surfaces of the Metal-Rich samples. In order to confirm the presence of excess indium on the surface, an experiment was conducted. Two samples, one Metal-Rich and one Nitrogen-rich, were selected that shared similar growth temperature and deposition thickness. New AFM scans were performed on each sample. The time between the original AFM scans and this experiment was 5 years. After the new scans were performed, the Metal-Rich sample was treated for 20 minutes in HCl to remove any possible oxide. The AFM images for this experiment are shown in Figure 59.

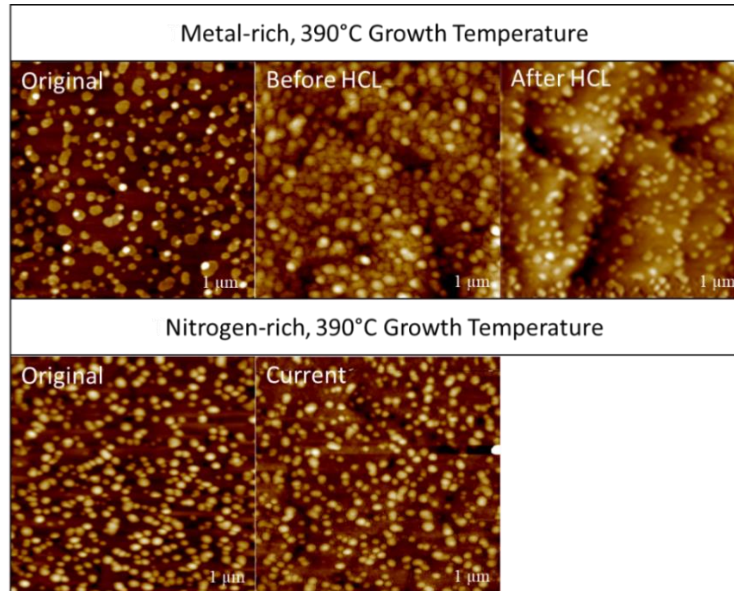

Figure 59. AFM Scans of Samples used for Analyzing the Possibility of Excess Indium on the Growth Surface.

The new scan for the Nitrogen-Rich growth was analyzed and compared to the original AFM scan. The results can be found in Figure 60. There was no significant change in QD diameter or height found in the Nitrogen-rich sample.

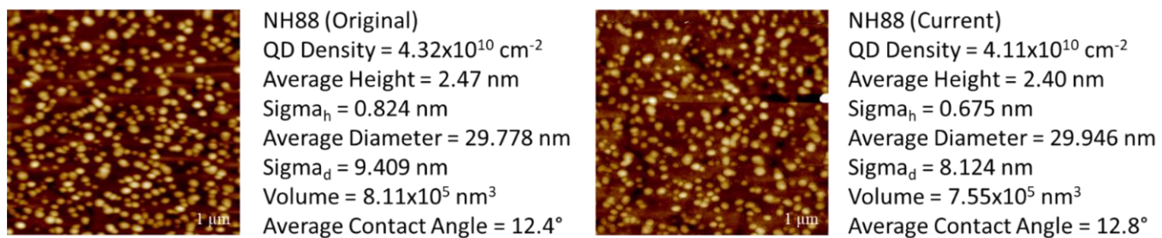

Figure 60. Nitrogen-Rich uncapped QD AFM scan analysis showing no significant change after 5 years.

Following the HCl treatment, the Metal-Rich sample was rescanned through AFM. After careful analysis, histograms for height and diameter were created for each time interval scan: original, before HCl, and after HCl. The resulting size distributions can be found in Figure 61.

The average QD height and diameter for each AFM scan is shown at the top left corner of the size distribution.

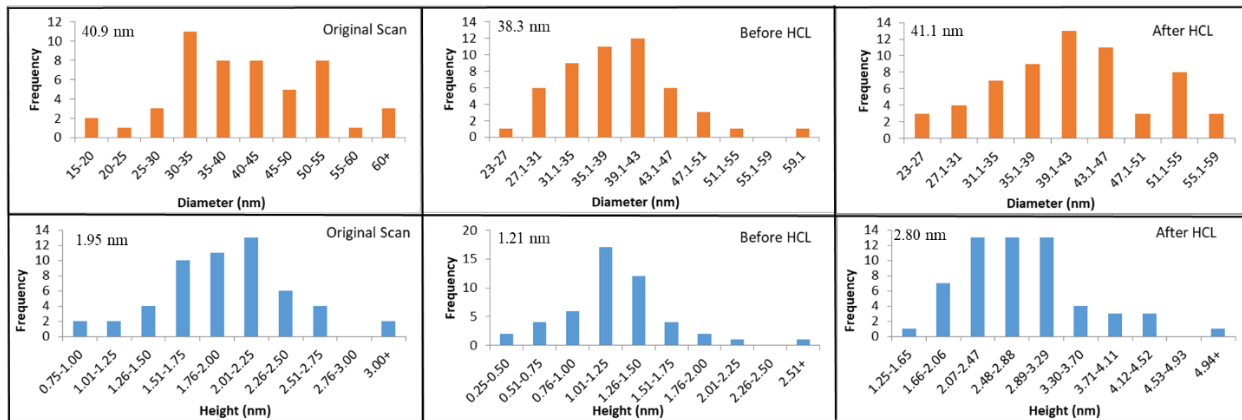

Figure 61. QD Diameter and Height distributions for Metal-Rich QD Showing Effects of Oxidation. (Average dimension added to the top left corner of each distribution.)

There was a significant change in the heights of the Metal-Rich QD sample. This is best explained by the presence of an indium adlayer in the original scan. Figure 62 illustrates the mechanism causing a change in measured height for each scan.

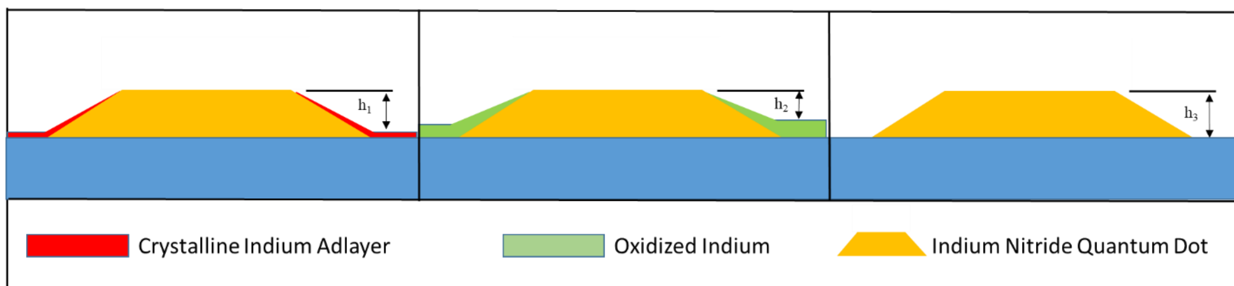

Figure 62. Conceptual Illustration of the Change in Structure Height Due to the Presence of an Indium Adlayer, an Oxidized Indium Layer, or Bare Growth Surface.

In the original scan, QDs are measured with height, h_1. The presence of an indium adlayer is unknown due to wetting the surface. After some time in ambient, “open air” conditions, the

indium adlayer oxidizes. The indium oxide layer is inherently thicker than the indium adlayer, so the measured height, h_2, of the QD goes down, h_2 is less than h_1. Finally, the surface is treated with HCl. The indium oxide layer was removed exposing the unaltered height, h_3, of the QD where h_3 is greater than h_1.

Given the observations from this experiment, it is safe to assume that all Metal-Rich samples have the presence of an indium adlayer in the original AFM scans. In addition, there was no indium accumulation in the Nitrogen-rich samples.

4.5 Summary of Metal-Rich Deviations

Due to the presence of an excess indium adlayer, all of the Metal-Rich behaviors were understood. Metal-Rich QDs have a preferred lateral growth direction. This was evident in the coalescence of QDs grown for longer times and the discrepancies in growth rates for QD height and diameter. The presence of an indium adlayer reduced the contact angle of the QD with the surface. The deposition rate of Metal-Rich QDs went down with increased “growth rate” due to the increase in indium accumulation on the surface. The thicker indium adlayer reduced the probability of an active nitrogen atom reaching the growth surface.

4.6 Light Emitting Structures

Three initial structures were fabricated to study the optical response of InN QDs: Metal-Rich, Nitrogen-Rich, and a GaN Reference. Due to the observations made during the growth investigation, every attempt was made to optimize the density and size of the QDs while keeping the substrate temperature the same for both the Metal-Rich and the Nitrogen-Rich samples. In addition, the initial GaN capping layer was fabricated at a temperature low enough to avoid InN

dissociation. After the InN QDs were sufficiently covered, the growth temperature was increased to improve the quality of the GaN layer. Figures 63, 64, and 65 display the growth structures for Metal-Rich, Nitrogen-Rich, and GaN reference samples, respectively.

For PL measurements, the samples were excited by a double-double, continuous-wave, YAG LASER at 266 nm. Samples were mounted in a closed-cycle cryostat (Janis CCS-150) (Janis, Woburn, MA) with a variable temperature range of 10 to 300 K. Detection of the PL emission was done by a liquid nitrogen cooled CCD detector array which was attached to a 50 cm focal-length spectrometer. The PL measurements can be found in Figure 66.

The optical response of the Metal-Rich sample at ~1.7 eV (730 nm) was encouraging. Normal GaN emission peaks were observed as well. At 2.2 eV, all samples exhibited a peak at the GaN impurity band. Bulk GaN emission was found at 3.4 eV. The bulk GaN peak became secondary in the Metal-Rich sample due to the presence of the confined active layer at 1.7 eV. Without cross-sectional transmission electron microscopy (TEM) to confirm the existence of stoichiometric InN QDs, it was determined that the emitted light was most likely due to $In_{0.60}Ga_{0.40}N$ QDs.

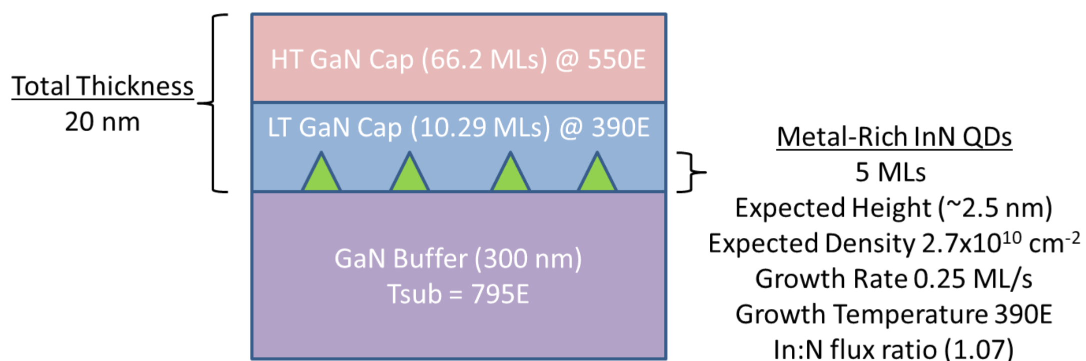

Figure 63. Graphical Illustration of the Metal-Rich InN QD Structure.

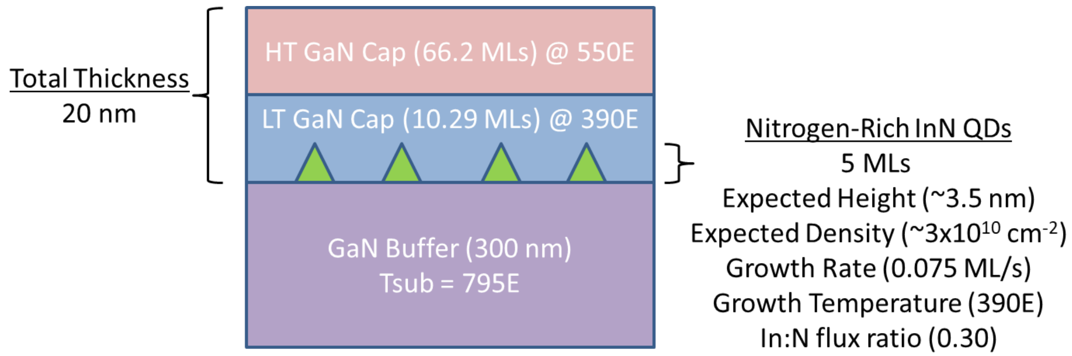

Figure 64. Graphical Illustration of the Nitrogen-Rich InN QD Structure.

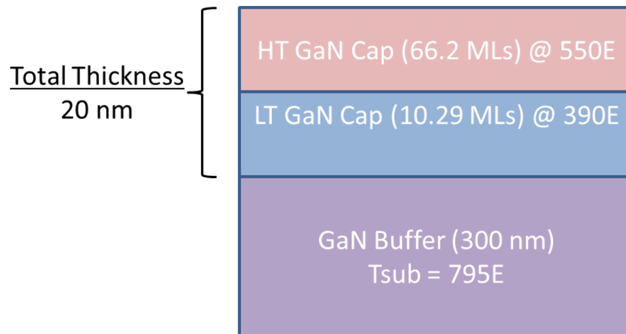

Figure 65. Graphical Illustration of the GaN Reference Structure.

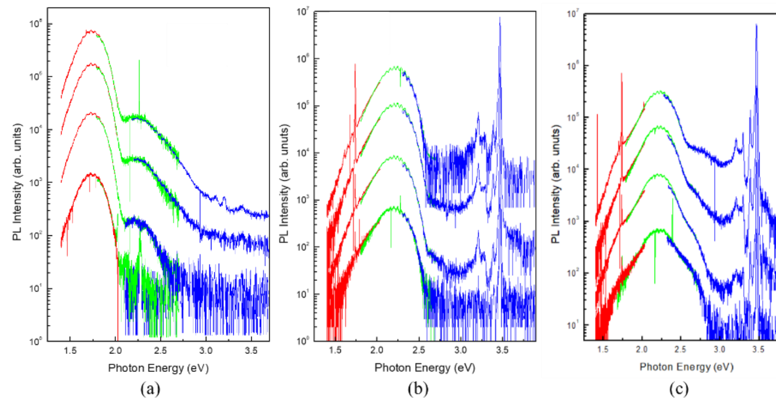

Figure 66. Results of the PL Spectroscopy at 10K for Confined InN/GaN QDs Using Metal-Rich and Nitrogen-Rich Growth Conditions: a) Metal-Rich, b) Nitrogen-Rich, and c) LT/HT GaN Reference.

Chapter 5: Conclusions & Future Work

4.7 Conclusions

This dissertation focused on three specific goals: 1) MBE growth of InN QDs, 2) comparing InN QDs grown under Metal-Rich and Nitrogen-Rich growth environments, and 3) developing an understanding of the factors which influence QD density, diameter, and height, deposited InN volume, the contact angle between the InN QD and the GaN growth surface, and the QD shape. Once these goals were satisfied, the optical response of InN QDs was observed. In order to achieve these goals, InN QDs samples were grown under Metal-Rich and Nitrogen-Rich growth environments using three growth parameters: growth temperature, deposition time, and deposition rate. After growth, all samples were measured using Atomic Force Microscopy and statistically analyzed.

The existence of oxidized excess indium was experimentally confirmed to exist on the Metal-Rich samples through AFM analysis. Before and after HCl treatment AFM scans were taken. Nitrogen-Rich samples were shown to not be affected by this condition.

Through comparison of the Metal-Rich and Nitrogen-Rich growth environment at each growth parameter, differences in the two growth environments were observed. The Nitrogen-Rich samples were found to behave like traditional self-assembled SK QDs following heterogeneous nucleation theory. Predicted outcomes for QD density, height, and diameter for each treatment were confirmed. The Metal-Rich samples followed heterogeous nucleation theory in terms of the change in QD density for each treatment. However, changes in the Metal-Rich QD dimensions showed a tendency for a change in the structure's diameter over a change in the structure's height. Metal-Rich QDs were observed to have a shallower contact angle and a "flat

top” shape as comparted to the Nitrogen-Rich QD’s contact angle and “curved” surface. In addition, Metal-Rich QD deposition rate decreased with increasing growth rate. These behaviors were attributed to the proposed presence of excess indium on the Metal-Rich QD growth surfaces.

A preliminary investigation into the optical response of Metal-Rich and Nitrogen-Rich InN QDs was performed. Conditions were chosen to optimize the success of the experiment. At a growth temperature of 390 °C, samples for each growth condition, Metal-Rich and Nitrogen-Rich, were fabricated with growth parameters that would produce QDs with similar height and density. A single period active layer was capped with a two-step growth process. In this two-step growth process, low temperature (390 °C) and high temperature (550 °C) GaN capped the InN QDs. PL spectroscopy showed emission of 1.7 eV (730 nm) for the Metal-Rich sample. No light emission was observed from the Nitrogen-Rich sample. Without cross-sectional transmission electron microscopy (TEM) to confirm the existence of stoichiometric InN QDs, it was determined that the emitted light was most likely due to $In_{0.60}Ga_{0.40}N$ QDs.

4.8 Future Work

Some underlying questions are yet to be answered by this work. TEM analysis of the Metal-Rich optical sample should be performed to prove the existence of capped InN QDs. Further investigation into the height manipulation of Metal-Rich samples should be performed. In order to realize the true motivation of this study, tunable wavelength emission, precise QD height control is needed. In addition, further study into the optimal GaN capping procedure should be done. With precise QD height manipulation and optimal GaN capping, Metal-Rich InN QDs show excellent promise in achieving tailored wavelength emission/adsorption.

References

[1] Anonymous. "U.S. Energy Information Administration - EIA - Independent Statistics and Analysis." How Much Electricity Is Used for Lighting in the United States? - FAQ - U.S. Energy Information Administration (EIA). Accessed August 09, 2019. https://www.eia.gov/tools/faqs/faq.php?id=99&t=3.

[2] N. Zheludev, "The Life and times of the LED - a 100-year History." Nature News. April 01, 2007. Accessed August 09, 2019. https://www.nature.com/articles/nphoton.2007.34.

[3] Anonymous. (USA Lighting), “Compare: LED Lights vs CFL vs Incandescent Lighting Chart.” Accessed July 15, 2014. https://www.usailighting.com/stuff/contentmgr/files/1/92ffeb328de0f4878257999e7d46d6e4/misc/lighting_comparison_chart.pdf.

[4] M.M.L Trevisanello, "Thermally Activated Degradation of Phosphor-Converted White LEDs." Thermally Activated Degradation of Phosphor-Converted White LEDs - LED Professional - LED Lighting Technology, Application Magazine. March 23, 2016. Accessed August 09, 2019. https://www.led-professional.com/technology/thermal-management/thermally-activated-degradation-of-phosphor-converted-white-leds-1.

[5] H. Morkoç, Nitride Semiconductors and Devices. Berlin: Springer, 1999. pp. 8-50.

[6] Anonymous. NSM Archive - Physical Properties of Semiconductors. Accessed August 09, 2019. http://www.ioffe.ru/SVA/NSM/Semicond/.

[7] A. Bett, F. Dimroth, G. Stollwerck, and O.v. Sulima. "III-V Compounds for Solar Cell Applications." Applied Physics A: Materials Science & Processing 69, no. 2 (1999): 119-29. doi:10.1007/s003390050983.

[6] Anonymous. (Philips Color Kinetics), “Useful Life,” Brief, Technical, 2010. Accessed: July 17, 2014. Available: http://www.colorkinetics.com/support/whitepapers/ledlifetime.pdf.

[7] Anonymous. (Lowel: A. L. R. Center), “Color Temperature & Color Rendering Index DeMystified.” Accessed: July 17, 2014. Available: http://lowel.com/edu/color_temperature_and_rendering_demystified_4.html.

[8] J. Wu, W. Walukiewicz, K. M. Yu, J. W. Ager, E. E. Haller, H. Lu, William J. Schaff, Y. Saito, and Y. Nanishi. "Unusual Properties of the Fundamental Band Gap of InN." Applied Physics Letters 80, no. 21 (2002): 3967-969. doi:10.1063/1.1482786.

[9] P. Preuss, An Unexpected Discovery Could Yield a Full Spectrum Solar Cell. Accessed July 17, 2014. https://www2.lbl.gov/Science-Articles/Archive/MSD-full-spectrum-solar-cell.html.

[10] Y.C. Pan, W.H. Lee, C. K. Shu, H. C. Lin, C. I. Chiang, H. Chang, D. S. Lin, M. C. Lee, and W. K. Chen. "Influence of Sapphire Nitridation on Properties of Indium Nitride

Prepared by Metalorganic Vapor Phase Epitaxy." Japanese Journal of Applied Physics 38, no. Part 1, No. 2A (1999): 645-48. doi:10.1143/jjap.38.645.

[11] C. Meissner, S. Ploch, M. Leyer, M. Pristovsek, and M. Kneissl. "Indium Nitride Quantum Dot Growth Modes in Metalorganic Vapour Phase Epitaxy." Journal of Crystal Growth 310, no. 23 (2008): 4959-962. doi:10.1016/j.jcrysgro.2008.07.066.

[12] Y. E. Romanyuk, R. G. Dengel, L. V. Stebounova, and S. R. Leone. "Molecular Beam Epitaxy of InN Dots on Nitrided Sapphire." Journal of Crystal Growth 304, no. 2 (2007): 346-51. doi:10.1016/j.jcrysgro.2007.01.048.

[13] K. M. Yu, Z. Liliental-Weber, W. Walukiewicz, W. Shan, J. W. Ager, S. X. Li, R. E. Jones, E. E. Haller, H. Lu, and W. J. Schaff. "On the Crystalline Structure, Stoichiometry and Band Gap of InN Thin Films." Applied Physics Letters 86, no. 7 (2005): 071910. doi:10.1063/1.1861513.

[14] C. S. Gallinat, G. Koblmüller, J. S. Brown, and J. S. Speck. "A Growth Diagram for Plasma-assisted Molecular Beam Epitaxy of In-face InN." Journal of Applied Physics 102, no. 6 (2007): 064907. doi:10.1063/1.2781319.

[15] K. Xu, and A. Yoshikawa. "Effects of Film Polarities on InN Growth by Molecular-beam Epitaxy." Applied Physics Letters 83, no. 2 (2003): 251-53. doi:10.1063/1.1592309.

[16] T. C. P. Chen, C. Thomidis, J. Abell, W. Li, and T.D. Moustakas. "Growth of InN Films by RF Plasma-assisted MBE and Cluster Beam Epitaxy." Journal of Crystal Growth 288, no. 2 (2006): 254-60. doi:10.1016/j.jcrysgro.2005.12.074.

[17] V. Mamutin, T. Shubina, V. Vekshin, V. Ratnikov, A. Toropov, S. Ivanov, M. Karlsteen, U. Södervall, and M. Willander. "Hexagonal InN/sapphire Heterostructures: Interplay of Interface and Layer Properties." Applied Surface Science 166, no. 1-4 (2000): 87-91. doi:10.1016/s0169-4332(00)00382-2.

[18] A. Yoshikawa, and S-B Che. "PROPOSAL OF NOVEL STRUCTURE LIGHT EMITTING DEVICES CONSISTING OF InN/GaN MQWs WITH ULTRATHIN InN WELLS IN GaN MATRIX." Selected Topics in Electronics and Systems Frontiers in Electronics, 2009, 235-45. doi:10.1142/9789814273022_0021.

[19] C. Nörenberg, R. Oliver, M. Martin, L. Allers, M. Castell, and G. Briggs. "Stranski-Krastanov Growth of InN Nanostructures on GaN Studied by RHEED, STM and AFM." Physica Status Solidi (a) 194, no. 2 (2002): 536-40. doi:10.1002/1521-396x(200212)194:23.0.co;2-b.

[20] R. Oliver, C. Nörenberg, M. Martin, M. Castell, L. Allers, and G. Briggs. "The Effect of V:III Ratio on the Growth of InN Nanostructures by Molecular Beam Epitaxy." Surface Science 532-535 (2003): 806-10. doi:10.1016/s0039-6028(03)00125-0.

[21] I. Gherasoiu, M. O'Steen, T. Bird, D. Gotthold, A. Chandolu, D. Y. Song, S. X. Xu, M. Holtz, S. A. Nikishin, and W. J. Schaff. "Characterization of High Quality InN Grown

on Production-style Plasma Assisted Molecular Beam Epitaxy System." Journal of Vacuum Science & Technology A: Vacuum, Surfaces, and Films 26, no. 3 (2008): 399-405. doi:10.1116/1.2899412.

[22] G. D. Chern, E. D. Readinger, H. Shen, M. Wraback, C. S. Gallinat, G. Koblmuller, and J. S. Speck. "Excitation Wavelength Dependence Of Terahertz Emission From Indium Nitride Thin Films." AIP Conference Proceedings, 2007. doi:10.1063/1.2729991.

[23] Y. F. Ng, Y. G. Cao, M. H. Xie, X. L. Wang, and S. Y. Tong. "Growth Mode and Strain Evolution during InN Growth on GaN(0001) by Molecular-beam Epitaxy." Applied Physics Letters 81, no. 21 (2002): 3960-962. doi:10.1063/1.1523638.

[24] A. Yoshikawa, N. Hashimoto, N. Kikukawa, S. B. Che, and Y. Ishitani. "Growth of InN Quantum Dots on N-polarity GaN by Molecular-beam Epitaxy." Applied Physics Letters 86, no. 15 (2005): 153115. doi:10.1063/1.1900948.

[25] E. Calleja, J. Ristić, S. Fernández-Garrido, L. Cerutti, M. A. Sánchez-García, J. Grandal, A. Trampert, U. Jahn, G. Sánchez, A. Griol, and B. Sánchez. "Growth, Morphology, and Structural Properties of Group-III-nitride Nanocolumns and Nanodisks." Physica Status Solidi (b) 244, no. 8 (2007): 2816-837. doi:10.1002/pssb.200675628.

[26] Y. G. Cao, M. H. Xie, Y. Liu, Y. F. Ng, H. S. Wu, and S. Y. Tong. "InN Island Shape and Its Dependence on Growth Condition of Molecular-beam Epitaxy." Applied Physics Letters 83, no. 25 (2003): 5157-159. doi:10.1063/1.1635077.

[27] Y-Z Yao, T. Sekiguchi, N. Ohashi, Y. Adachi, and T. Ohgaki. "Photoluminescence and X-ray Diffraction Measurements of InN Epifilms Grown with Varying In/N Ratio by Plasma-assisted Molecular-beam Epitaxy." Applied Physics Letters 92, no. 21 (2008): 211910. doi:10.1063/1.2937833.

[28] E. Dimakis, E. Iliopoulos, K. Tsagaraki, and A. Georgakilas. "Physical Model of InN Growth on Ga-face GaN (0001) by Molecular-beam Epitaxy." Applied Physics Letters 86, no. 13 (2005): 133104. doi:10.1063/1.1891292.

[29] C-L Hsiao, L-W Tu, M. Chen, Z-W Jiang, N-W Fan, Y-J Tu, and K-R Wang. "Polycrystalline to Single-Crystalline InN Grown on Si(111) Substrates by Plasma-Assisted Molecular-Beam Epitaxy." Japanese Journal of Applied Physics 44, no. No. 34 (2005). doi:10.1143/jjap.44.l1076.

[30] T. Araki, Y. Saito, T. Yamaguchi, M. Kurouchi, Y. Nanishi, and H. Naoi. "Radio Frequency-molecular Beam Epitaxial Growth of InN Epitaxial Films on (0001) Sapphire and Their Properties." Journal of Vacuum Science & Technology B: Microelectronics and Nanometer Structures 22, no. 4 (2004): 2139. doi:10.1116/1.1771682.

[31] H. Ahn, Y.-P. Ku, Y.-C. Wang, C.-H. Chuang, S. Gwo, and C.-L. Pan. "Erratum: “Terahertz Spectroscopic Study of Vertically-aligned InN Nanorods” [Appl. Phys. Lett.

91, 163105 (2007)]." Applied Physics Letters 94, no. 18 (2009): 189901. doi:10.1063/1.3137182.

[32] L. Zhou, T. Xu, D. J. Smith, and T. D. Moustakas. "Microstructure of Relaxed InN Quantum Dots Grown on GaN Buffer Layers by Molecular-beam Epitaxy." Applied Physics Letters 88, no. 23 (2006): 231906. doi:10.1063/1.2205166.

[33] T. Stoica, R. Meijers, R. Calarco, T. Richter, and H. Lüth. "MBE Growth Optimization of InN Nanowires." Journal of Crystal Growth 290, no. 1 (2006): 241-47. doi:10.1016/j.jcrysgro.2005.12.106.

[34] T. Tansley, and C. Foley. "Electron Mobility in Indium Nitride." Electronics Letters 20, no. 25-26 (1984): 1066. doi:10.1049/el:19840729.

[35] H. Sunakawa, A. A. Yamaguchi, A. Kimura, and A. Usui. "Growth of InN by Chloride-Transport Vapor Phase Epitaxy." Japanese Journal of Applied Physics 35, no. Part 2, No. 11A (1996). doi:10.1143/jjap.35.l1395.

[36] I. Shalish, G. Seryogin, W. Yi, J. M. Bao, M. A. Zimmler, E. Likovich, D. C. Bell, F. Capasso, and V. Narayanamurti. "Epitaxial Catalyst-Free Growth of InN Nanorods on C-Plane Sapphire." Nanoscale Research Letters 4, no. 6 (2009): 532-37. doi:10.1007/s11671-009-9276-z.

[37] A. L. Syrkin, V. Ivantsov, A. Usikov, V. A. Dmitriev, G. Chambard, P. Ruterana, A. V. Davydov, S. G. Sundaresan, E. Lutsenko, A. V. Mudryi, E. D. Readinger, G. D. Chern-Metcalfe, and M. Wraback. "InN Layers Grown by the HVPE." Physica Status Solidi (c) 5, no. 6 (2008): 1792-794. doi:10.1002/pssc.200778646.

[38] K. Mitamura, T. Honke, J. Ohta, A. Kobayashi, H. Fujioka, and M. Oshima. "Characteristics of InN Grown Directly on Al2O3 (0001) Substrates by Pulsed Laser Deposition." Journal of Crystal Growth 311, no. 5 (2009): 1316-320. doi:10.1016/j.jcrysgro.2008.12.015.

[39] T. Fujii, K. Shimomoto, R. Ohba, Y. Toyoshima, K. Horiba, J. Ohta, H. Fujioka, M. Oshima, S. Ueda, H. Yoshikawa, and K. Kobayashi. "Fabrication and Characterization of AlN/InN Heterostructures." Applied Physics Express 2, no. 1 (2009): 011002. doi:10.1143/apex.2.011002.

[40] R. Ohba, K. Mitamura, K. Shimomoto, T. Fujii, S. Kawano, J. Ohta, H. Fujioka, and M. Oshima. "Growth of Cubic InN Films with High Phase Purity by Pulsed Laser Deposition." Journal of Crystal Growth 311, no. 11 (2009): 3130-132. doi:10.1016/j.jcrysgro.2009.03.010.

[41] W-H Chang, W-C Ke, S-H Yu, L Lee, C-Y Chen, W-C Tsai, H. Lin, W-C Chou, M-C Lee, and W-K Chen. "Effects of Growth Temperature on InN∕GaN Nanodots Grown by Metal Organic Chemical Vapor Deposition." Journal of Applied Physics 103, no. 10 (2008): 104306. doi:10.1063/1.2927249.

[42] N. Chao, Z. Rong, X. Zi-Li, X. Xiang-Qiang, L. Bin, F. De-Yi, L. Qi-Jia, H. Ping, G. Shu-Lin, S. Yi, and Z. You-Dou. "Synthesis of [100] Wurtzite InN Nanowires and [011] Zinc-Blende InN Nanorods." Chinese Physics Letters 25, no. 5 (2008): 1780-783. doi:10.1088/0256-307x/25/5/070.

[43] M. C. Johnson, C. J. Lee, E. D. Bourret-Courchesne, S. L. Konsek, S. Aloni, W. Q. Han, and A. Zettl. "Growth and Morphology of 0.80eV Photoemitting Indium Nitride Nanowires." Applied Physics Letters 85, no. 23 (2004): 5670-672. doi:10.1063/1.1831563.

[44] Z. Bi, "Low-temperature MOCVD Growth of InN Buffer Layers with Indium Pre-deposition Technology." Journal of Crystal Growth 300, no. 1 (2007): 123-26. doi:10.1016/j.jcrysgro.2006.11.003.

[45] S. P. Minor, “Plasma-Assisted Molecular Beam Epitaxial Growth of Indium Nitride for Future Device Fabrication.” University of Arkansas. (2012).

[46] J. Neugebauer, T. K. Zywietz, M. Scheffler, J. E. Northrup, H. Chen, and R. M. Feenstra. "Adatom Kinetics On and Below the Surface: The Existence of a New Diffusion Channel." Physical Review Letters 90, no. 5 (2003). doi:10.1103/physrevlett.90.056101.

[47] J. G. Lozano, A. M. Sánchez, R. García, D. Gonzalez, O. Briot, and S. Ruffenach. "Misfit Relaxation of InN Quantum Dots: Effect of the GaN Capping Layer." Applied Physics Letters 88, no. 15 (2006): 151913. doi:10.1063/1.2195642.

[48] O. Manasreh, Semiconductor Heterojunctions and Nanostructures. New York: Mc Graw Hill, 2005. pp. 379-382.

[49] M. Ohring, The Materials Science of Thin Films. San Diego, Calif: Academic Press, 2006. pp. 376-395.

[50] Arkajitmandal. "Interplanar Spacing of Hexagonal Lattice Calculator." Calistry. February 08, 2017. Accessed August 09, 2019. https://calistry.org/calculate/spacingHexagonalLattice.

[51] Liu, Jia-Ming. Photonic Devices. Cambridge University Press, 2005. pp. 876-925

[52] Suryanarayana, C., and M. Grant. Norton. X-Ray Diffraction: A Practical Approach. Plenum Press, 1998. pp. 125-152.

[53] Wang, S. "How Our Predictions Work (continued)." Princeton University. 2019. Accessed August 09, 2019. http://election.princeton.edu/2014/09/18/how-our-predictions-work-continued/.

Appendix A: Description of Research for Popular Publication

"The Old Guy"

By Paul Minor

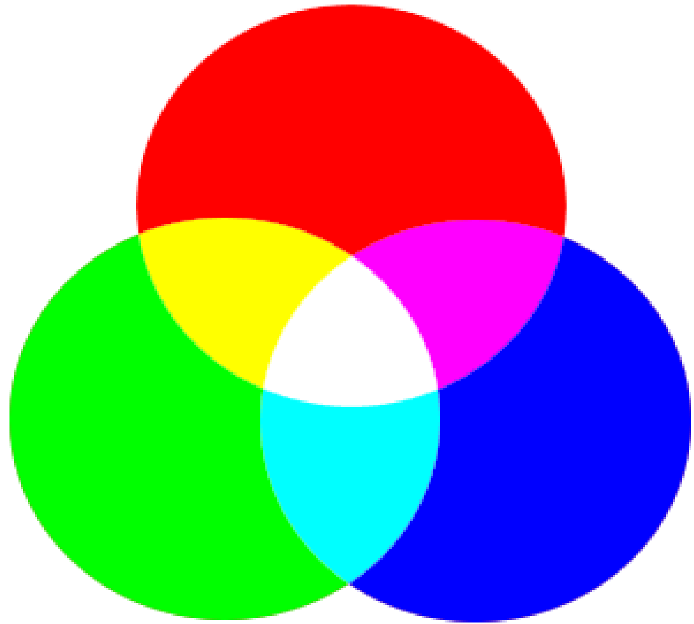

Being the oldest student in your office can create quite a buzz. Just ask the 42-year-old graduate student, Paul Minor. "Yeah, I see a lot of YouTube videos being stopped when I walk around the office," says Mr. Minor in response to questions about being mistaken as a visiting faculty member in the graduate student offices. Mr. Minor, a student in Dr. Greg Salamo's research group, is finally completing his PhD research. "It's been a long, and drawn out process. I'm looking forward to AARP benefits when I finish."

Mr. Minor's research centers around the growth of indium nitride quantum dots. Quantum dots are very small, crystal structures that are so small, they actually "trap" electrons. By changing the size of these very small crystals, Mr. Minor can create light of all visible colors. When he started this research, he was motivated to create a system which utilized crystal sizes to produce light of three specific colors: Red (650 nm), Green (510 nm), and Blue (475 nm). The overall mission was to create a trichromatic (3 color) light emitting diode (LED).

Though the LED was never fabricated, Mr. Minor's work has laid the foundation for future investigations. He has developed an understanding of how growth temperature, deposition time

and deposition temperature affect the development of InN QDs. In addition, he has developed this understanding of QD development for two separate growth methods. Finally, Mr. Minor exhibited red (730 nm) light from his little crystals.

It looks like the future is “bright” for LED research at the University of Arkansas. This is one time that it might be alright to let “The Old Guy” head towards the light.

Appendix B: Executive Summary of Newly Created Intellectual Property

The following list of new intellectual property items were created in the course of this research project and should be considered from both a patent and commercialization perspective.

1. Demonstrated the Processes of Metal-Rich and Nitrogen-Rich QD growth for InN on GaN substrates using RF-MBE. These processes were investigated using temperature, time, and rate dependencies.
2. Established conditions by which the size and density of InN QDs can be fabricated on GaN substrates though RF-MBE.
3. Demonstrated an optical response at 700 nm for capped InN QDs using a LT/HT GaN capping procedure.

Appendix C: Potential Patent and Commercialization Aspects of listed Intellectual Property Items

C.1 Patentability of Intellectual Property

No devices were fabricated as the result of this research. A device patent cannot be pursued; however, a process patent could be considered. The processes that were used to fabricate the InN QDs, while not understood by the research community, have been studied or used by other groups. These processes therefore, are not "novel." The structure that was created and produced an optical emission of 700 nm was the first case that was observed from extensive literature searches. However, tunable wavelength emission by InN and low temperature (LT)/high temperature (HT) capping proceedures are not "novel." All three items listed in Appendix B should be considered incremental advances in previously applied knowledge.

C.2 Commercialization Prospects (Should Each Item be Patented)

The growth process for InN by MBE presented in this thesis does not meet patentability requirements and therefore should not be considered for commercialization.

C.3 Possible Prior Disclosure of IP

This research has not been publicly disclosed. However, work was performed in the communication of the research (dissertation writing) and QD analysis on an Arkansas State University computer.

Appendix D: Broader Impact of Research

D.1 Applicability of Research Methods to Other Problems

The research methods utilized in this work can be applied to developing an understanding of the growth physics of new material systems. Actually, new insights could be gained on currently used material systems if complex growth structures are required.

Analysis techniques (structural analysis, statistical analysis, etc.) which were used in this work are applicable to all forms of crystal growth. These techniques are also beneficial to studying surfaces in which devices will be fabricated.

The MBE growth methodology used in this research could be extended to other material systems: III-arsenide, III-phosphide, III-bismides, etc.

D.2 Impact of Research Results on U.S. and Global Society

The results of this research is still very far from making an impact on U.S. or Global Societies. However, continued work on understanding the growth mechanics of InN could lead to a host of interesting optoelectronic device applications (solar cells, LEDs, photodiodes, devices in optical communication, etc.). If InN devices become a reality, this work will be small part of the impact in which InN devices have on U.S. and Global Societies.

D.3 Impact of Research Results on the Environment

All materials created by this research are not hazardous. No immediate physical harm will come to the environment due to this research. Future impacts could be positive for the environment. Further investigation that leads to the creation of an LED structure from this basic

research would lead to a reduction in energy consumption and a reduced dependency on fossil fuel. In addition, the full use of the III-nitride system's wide range of direct band gaps could be used to create high efficiency solar cells. The use of indium is a concern. Indium, a rare earth metal, is "rare" and in short supply. It may not be feasible to make a tremendous impact on the global environment with a rare earth metal.

Appendix E: Microsoft Project for PhD MicroEP Degree Plan

	Task Mode	Task Name	Duration	Start	Finish
4		Distribute Proposal to Committee	1 day	Mon 7/21/14 8:00 AM	Mon 7/21/14 5:00 PM
5		Prepare PhD Proposal Presentation	6 days	Mon 7/21/14 8:00 AM	Sun 7/27/14 5:00 PM
6		PhD Proposal Defense	1 day	Mon 7/28/14 8	Mon 7/28/14 5
7		Research	1803 days	Wed 8/1/12 8:(	Fri 6/28/19 5:0
8		Apply for Graduation	1 day	Mon 7/29/19 8	Mon 7/29/19 5
9		Write PhD Dissertation	1302 days	Fri 8/1/14 8:00	Mon 7/29/19 5
10		Distribute Dissertation to Committee	1 day	Tue 7/30/19 8:00 AM	Tue 7/30/19 5:00 PM
11		Dissertation Defense	1 day	Tue 8/6/19 8:0	Tue 8/6/19 5:0
12		Dissertation Corrections	4 days	Tue 8/6/19 8:0	Fri 8/9/19 5:00
13		Dissertation to Graduate School	1 day	Fri 8/9/19 8:00 AM	Fri 8/9/19 5:00 PM
14		Graduation	0 days	Sat 12/21/19 8:	Sat 12/21/19 8:

Appendix F: Identification of All Software Used in Research and Dissertation Generation

Computer #1:
  Model Number: Dell Vostro 230
  Serial Number: 86LKJM1
  Location: Nano301
  Owner: University of Arkansas
Software #1:
  Name: Microsoft Office 2010
  Purchased by: Nano Institute
Software #2:
  Name: Origin Pro 8
  Purchased by: Dr. Gregory J. Salamo
Software #3:
  Name: Nanoscope Analysis Software V1.50
  Purchased by: Free
Software #4:
  Name: Crystalograph
  Purchased by: Free

Computer #2:
  Model Number: Dell Latitude 5592
  Serial Number: 5Z9D5S2
  Location: Astate – LSW 232 (laptop)
  Owner: Arkansas State University
Software #1:
  Name: Microsoft Office 2016
  Purchased by: Arkansas State University
Software #2:
  Name: Nanoscope Analysis Software V1.50
  Purchased by: Free

Appendix G: All Publications Published, Submitted and Planned

No publications were published, submitted, or planned from this work.